

LEIBNIZ UNIVERSITÄT HANNOVER  
INSTITUTE OF QUANTUM OPTICS

SPECTROSCOPY AND EXCITATION  
DYNAMICS OF  $\text{LiYF}_4:\text{Pr}^{3+}$   
NANOCRYSTALS

Von der Fakultät für Mathematik und Physik  
der Gottfried Wilhelm Leibniz Universität Hannover zur  
Erlangung des Grades

DOKTOR DER NATURWISSENSCHAFTEN  
Dr. rer. nat.

genehmigte Dissertation von

Simon Spelthann

2023

Referent:  
Prof. Dr. Detlev Ristau

Korreferenten:  
Prof. Dr. Uwe Morgner  
Prof. Dr. Markus A. Schmidt

Tag der Promotion: 14.06.2023

Simon Spelthann: *Spectroscopy and Excitation Dynamics of LiYF<sub>4</sub>:Pr<sup>3+</sup> Nanocrystals* © März 2023, Hannover

## ABSTRACT

---

Downsizing lanthanide-doped crystals to the nanoscale allows for new applications in a variety of forms as photonic composites. The dipole-forbidden  $4f$  transitions in trivalent lanthanide ions promise high excited state lifetimes and quantum yields that are required for a plethora of applications, e.g., in lasers, phosphors, and quantum memories. However, nanocrystals undergo excitation quenching which takes mostly place at the nanocrystal surface and severely reduces the lifetime and quantum yield. So far, optimizing lanthanide nanocrystals required resource-consuming experimental procedures covering multiple syntheses, complex morphological characterization and extensive spectroscopy.

In this thesis,  $\text{LiYF}_4:\text{Pr}^{3+}$  was chosen as a model system because it is frequently used as bulk laser crystal whose spectroscopic properties are well investigated. A concentration series consisting of four samples ( $\sim 10$  nm, 0.7 – 1.47 at%) and a size series consisting of five samples ( $\sim 5$  at%, 12 – 21 nm) was spectroscopically characterized. As the main result of this investigation, an unexpected yet intense emission was observed that in bulk crystals is only exploitable through excitation of a different, subjacent energy level. Considering the spectroscopic results, a numerical model based on a Monte Carlo approach was implemented that takes the relevant energy exchange and quenching mechanisms into account. As main result of the present thesis, the numerical simulations were able to predict the excited state lifetimes and quantum yields of the nanocrystals with a maximum uncertainty of 12.6% for the lifetimes. To demonstrate the potential of this numerical approach, an undoped shell was added around the core particles in the model which extends the lifetime by up to 44%. Furthermore, spatiotemporal analysis of single nanocrystals points towards a new type of energy trapping in lanthanide nanocrystals.

The numerical approach presented in this thesis constitutes an enormous potential for nanocrystal research, since it can be employed in any material system such as upconversion or avalanching nanocrystals. In the future, the considered approach allows for numerical optimization of the  $\text{LiYF}_4:\text{Pr}^{3+}$  nanocrystals for application as quantum memories, lanthanide-based ratiometric nanothermometers, or efficient fused silica fiber lasers operating in the visible spectrum.

**KEYWORDS:** Lanthanides, Nanocrystals, Spectroscopy, Monte Carlo Simulations





# CONTENTS

---

<b>I</b>	<b>INTRODUCTION</b>	<b>1</b>
1	MOTIVATION	3
1.1	The Age of the Photon . . . . .	3
1.2	Plenty of Room at the Bottom . . . . .	4
1.3	Contribution to Nanotechnology and Photonics . . . . .	5
2	NANOCRYSTAL SYNTHESIS AND CHARACTERISTICS	9
2.1	Synthesizing Rare Earth Doped Nanocrystals . . . . .	9
2.1.1	Synthesis of Monodispersed $\text{LiYF}_4:\text{Pr}^{3+}$ Nanocrystals . . . . .	11
2.2	Structural Properties of $\text{LiYF}_4:\text{Pr}^{3+}$ Nanocrystals . . . . .	13
2.2.1	X-Ray Diffraction . . . . .	13
2.2.2	Transmission Electron Microscopy and Energy Dispersive X-Ray Spectroscopy . . . . .	15
2.2.3	Flexibility and Precision of the Synthesis . . . . .	18
2.2.4	Sample Overview . . . . .	19
3	ENERGY STATES OF RARE EARTH IONS	21
3.1	The Free Lanthanide Ion . . . . .	22
3.2	Influence of the Crystal Field . . . . .	25
3.3	Trivalent Praseodymium . . . . .	25
4	INTERACTION OF ENERGY AND MATTER	27
4.1	Intraionic Interaction . . . . .	27
4.1.1	Absorption . . . . .	28
4.1.2	Emission . . . . .	29
4.1.3	Nonradiative Transitions . . . . .	29
4.2	Interionic Interaction . . . . .	30
4.2.1	Overview on Interionic Energy Transfers . . . . .	30
4.2.2	Calculation of the Transfer Rates . . . . .	31
4.3	Particularities on the Nanoscale . . . . .	34
4.3.1	Local Field Effects on Nanocrystals . . . . .	35
4.3.2	Förster Transfer based Multi-Phonon Quenching . . . . .	36
<b>II</b>	<b>SPECTROSCOPY</b>	<b>39</b>
5	EXPERIMENTAL SETUPS	41
5.1	Absorption . . . . .	41
5.2	Excited State Lifetimes . . . . .	42
5.3	Emission . . . . .	43
5.4	Quantum Yield . . . . .	43
6	THE ORGANIC LIGAND: OLEIC ACID	45
7	ABSORPTION SPECTROSCOPY	49
7.1	Absorption Cross Sections . . . . .	49
7.2	Fitting the Absorption Cross Section . . . . .	50

7.2.1	Fitting Procedure . . . . .	50
7.2.2	Discussion of the Fitting Results . . . . .	52
7.3	Discussion . . . . .	53
8	EMISSION SPECTROSCOPY . . . . .	57
8.1	Spontaneous Emission Spectra . . . . .	57
8.2	Excited State Lifetime and Quantum Yield . . . . .	61
8.2.1	Analysis of the Excited State Lifetime . . . . .	61
8.2.2	Analysis of the Quantum Yield . . . . .	63
8.2.3	Discussion on the Decay Dynamics . . . . .	64
8.2.4	Estimation of Characteristic Lengths . . . . .	65
III	NUMERICS . . . . .	67
9	MODELLING THE EMISSION DECAY . . . . .	69
9.1	The Numerical Approach . . . . .	69
9.2	From Rates to Probabilities . . . . .	71
9.2.1	Rates . . . . .	71
9.2.2	Spectral Overlap . . . . .	74
9.2.3	Relationship Between Energy Migration/Hopping and the Cross-Relaxations . . . . .	74
9.2.4	Process Probabilities . . . . .	75
9.3	Software and Computation . . . . .	76
9.3.1	Implementation . . . . .	76
9.3.2	Computational Resources . . . . .	77
10	DETERMINATION OF THE CHARACTERISTIC LENGTHS . . . . .	79
10.1	Statistics . . . . .	79
10.2	Parameter Search . . . . .	80
10.3	Plausibility . . . . .	84
11	PREDICTING THE EXCITATION DYNAMICS . . . . .	87
11.1	Prediction of the Size Series . . . . .	87
11.2	Process statistics . . . . .	88
12	A SIMPLE NUMERIC OPTIMIZATION APPROACH . . . . .	91
12.1	Simulation of Core-Shell nanocrystals . . . . .	91
12.2	Process Statistics . . . . .	92
12.3	Resource-related Potential . . . . .	93
IV	CONCLUSION . . . . .	95
13	FUTURE PROSPECT . . . . .	97
13.1	Spatial Decay Dynamics . . . . .	97
13.2	Intelligent Optimization . . . . .	98
13.3	Prospect on Potential Application of Optimized Nanocrystals in Photonics . . . . .	100
14	SUMMARY . . . . .	103
V	APPENDIX . . . . .	105
15	ADDITIONAL RESULTS FROM THE STRUCTURAL CHARACTERIZATION . . . . .	107

15.1	Transmission Electron Microscopy Pictures . . . . .	107
15.2	Element Mapping and Linescans . . . . .	110
16	LIFETIME FITTING RESULTS	113
17	PROCESS STATISTICS RESULTS	117
17.1	Core-Only Nanocrystals . . . . .	117
17.2	Core-Shell Nanocrystals with 6 nm shell thickness . . .	122
18	ADDITIONAL SIMULATION PARAMETERS	127
	BIBLIOGRAPHY	129
	LIST OF PUBLICATIONS	145
	ACKNOWLEDGEMENTS	149



Part I

INTRODUCTION



## MOTIVATION

---

The 20<sup>th</sup> century was the century of the electron because electronics had a significant impact on society and allowed for numerous technological innovations such as computers and telecommunication. The continuous advance in electronics is described by Moore's Law that predicted that the number of transistors per unit area on integrated circuit chips doubles approximately every two years. However, this advance currently approaches its physical size limit which is why researchers search for new ways to prevent Moore's Law from ending [1].

### 1.1 THE AGE OF THE PHOTON

„The 21<sup>th</sup> century is the age of the photon.“ [2] – Photonics already spawned a wide range of technological innovations such as medical imaging, quantum computing, or fiber-optic communication. Fused silica fiber technology allowed to implement a world-wide communication network but is also key to other applications such as fiber lasers. By doping fused silica fibers with lanthanide ions such as Ytterbium, Erbium, or Thulium flexible yet rugged lasers can be set up in a compact form. Lanthanide ions in general provide exceptional spectroscopic properties such as high excited state lifetimes which make them excellent candidates for lasers, luminescent phosphors, or quantum memories [3–5].

However, photonics face physical limits that need innovative approaches to enable further progress – just as in electronics. For example, in the case of fiber lasers, one limit is the extension of operation wavelengths to the visible spectrum. Stimulated continuous wave emission of visible photons in fused silica fibers is challenging, so far, because the high phonon energies of around  $1100\text{ cm}^{-1}$  in fused silica enable efficient multiphonon quenching that depopulates the excited state of the ions [6]. Among the lanthanide ions,  $\text{Pr}^{3+}$  shows intense emissions from the vacuum ultraviolet up to near infrared spectral region, which found application in laser physics [7–11], phosphors [12–15], or single photon generation [16–18]. Percival and co-workers investigated visible emission and lasing from a  $\text{Pr}^{3+}$ -doped fused silica fiber and found slope efficiencies of only a few percent [19]. They concluded that the fast non-radiative processes due to the high phonon energies of fused silica make such fiber unsuitable for laser applications [19]. As alternatives, visible photons can be generated from other material platforms such as lanthanide-doped fluoride glasses or

dye-doped polymers [20–23]. Since both approaches are not compatible with conventional fiber technology, researchers combined dyes with liquid core fibers based on fused silica [24, 25]. However, the dyes bleach within few hours of operation, thus, rendering this approach unsuitable for rugged and flexible fiber lasers [20, 26]. Developing fiber lasers in the visible spectrum based on fused silica poses an exciting challenge because their excellent beam quality and potential to high power levels would find countless applications in science and technology, for example in precision spectroscopy [27], material processing [28], or display technology [29].

## 1.2 PLENTY OF ROOM AT THE BOTTOM

„There is plenty of room at the bottom.“ [30] – This citation has become synonymous with the variety of possibilities arising from science at the nanoscale. The field of nanotechnology led to advanced metrology instruments such as high-resolution electron microscopes or atomic force microscopes. Another prominent discipline of nanotechnology are so-called bottom-up approaches for the synthesis of smallest nanomaterials such as lanthanide-doped nanocrystals [31]. The most prominent representative of lanthanide nanocrystals is Sodium Yttrium tetrafluoride ( $\text{NaYF}_4$ ) doped with trivalent Erbium and Ytterbium ions. These nanocrystals can upconvert infrared photons to the visible, albeit with low quantum yield, and found a broad range of application in fields such as cancer therapy, biosensing, and solar energy conversion [32–36].

In electronics, turning to nanotechnology helped to keep pace with Moore’s Law [1]. As one recent example for a successful symbiosis of photonics with nanotechnology, liquid-core fibers filled with colloidal 2D semiconductor nanoplatelets emerged as a fused-silica fiber technology compatible alternative that provides pulsed stimulated emission in the visible spectrum [37, 38].

Nanotechnology and photonics do not only enter a symbiosis but also cross-fertilize each other as in the case of lanthanide upconversion nanocrystals that inspired ratiometric temperature sensing [39]. In so-called nanothermometry, the emission intensity ratio of thermally coupled energy levels in lanthanide nanocrystals is exploited to measure temperature. As a consequence, lanthanide nanocrystals constitute a flexible and versatile photonic temperature sensor that, in combination with optical fiber technology is inert to strong electrical fields [40], can be applied as fiber tip sensor [41–43], or, in combination with stimulated emission depletion (STED), can enable temperature measurement below the optical diffraction limit as numerically shown in [44].

Many lanthanide nanocrystals, however, suffer from low efficiencies, because quenching mechanisms at the nanocrystal surface se-



verely reduce both, the excited state lifetime and quantum yield, thus limiting the field of application for the nanocrystals. Consequently, researchers make enormous efforts to optimize the excited state lifetime and quantum yield of lanthanide nanocrystals [45, 46]. Such experimental optimization is resource-consuming and comprises the synthesis of multiple samples as well as their morphological and spectroscopic characterization. In contrast to the status quo, numerical approaches carry the potential to drastically reduce these efforts which would accelerate and facilitate the development of nanocrystals optimized toward applications.

### 1.3 CONTRIBUTION TO NANOTECHNOLOGY AND PHOTONICS

This thesis aims at leaving behind the resource-consuming experimental optimization approaches and paving the way to numerically optimize the design of lanthanide nanocrystals. Due to limited capabilities to accurately describe the excitation dynamics of nanocrystals at small sizes, numerical approaches have so far only complemented experimental investigations. Most prominently, this has been the case for above-mentioned upconversion nanocrystals ( $\text{NaYF}_4:\text{Er}^{3+}, \text{Yb}^{3+}$ ), modeled in terms of a set of differential rate equations.

This approach is widely used to model lasers [3, 20, 47], and comparable approaches recently have been used to model photon avalanche emission [48]. In these rate-equation-based models, the number of energy levels taken into account determines the number of coupled equations. Every single energy level of the involved lanthanide ions is assigned an individual differential equation that includes all relevant population and de-population processes. Although simulations based on this approach comprise a certain optimization potential, they reach their limit at some ten nanometers particle size.

The first model was developed for micron-sized crystals [49–51], a scale where the optical properties are determined by the dynamics in the volume of the particles as in bulk crystals. Rate-equation models average the properties and ionic distances of all the ions and determine the transition rates in terms of a single macroscopic variable. Consequently, the model considers only one process rate for the average distances, i.e. for example one rate for energy transfer in the whole nanocrystal [52].

However, to accurately model nanoscopic particles, spatial dynamics have to be considered because surface effects become increasingly important at this scale [53–55]. Subsequently, researchers continued to develop rate-equation-based approaches towards enabling spatial resolution of the excitation dynamics. In 2015, Villanueva-Delgado and co-workers presented an approach that takes the inter-ionic distances into account and averages the rates of every ion within a nanocrystal, instead of calculating the rate of an average distance [55–57]. Pini and

co-workers recently extended this model by dividing the nanocrystals into a core and an outer layer that interacts with the surrounding medium and achieved a certain spatial resolution in 40 nm sized nanocrystals [58].

To summarize, rate equations can describe macroscopic and, to some extent, microscopic systems particularly well as long as surface effects can be neglected [3, 47, 48, 50, 51, 55–59]. Therefore, all these rate equation-based models provided an increasingly accurate understanding of the underlying dynamics within lanthanide-doped particles. However, these simulations reach their limits at nanoscopic scales, which restricts them to a complementary role in nanocrystal research. Consequently, existing numerical approaches cannot exploit the potential for understanding and predicting spatial excitation dynamics in lanthanide nanocrystals.

In this thesis, a numerical model based on a Monte Carlo approach is presented that allows to understand, and, more importantly, to predict the spatiotemporal excitation dynamics of lanthanide nanocrystals. To achieve this,  $\text{LiYF}_4:\text{Pr}^{3+}$  nanocrystals were synthesized and morphologically characterized at the Fraunhofer Center for Applied Nanotechnology. A total of nine samples was provided that consisted of a concentration and a size series which are introduced in Part I of this thesis.

An extensive spectroscopic characterization of these samples is presented in Part II as a result of this thesis. The spectroscopic behaviour of the nanocrystals was compared to bulk crystals and revealed strong multiphonon quenching that results in reduced quantum yields, see the artwork in Figure 1.

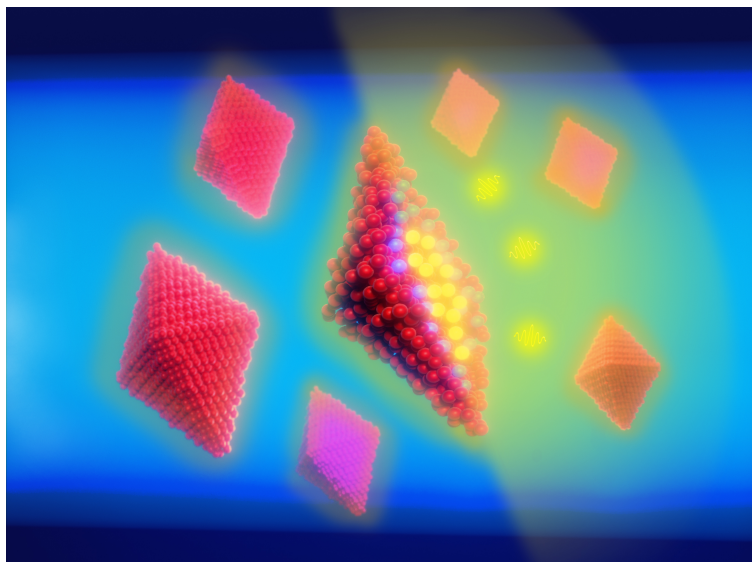


Figure 1: Artistic representation of  $\text{LiYF}_4:\text{Pr}^{3+}$  nanocrystals in an organic solvent and their spectroscopic behavior that was chosen as cover picture in *Nanoscale Advances* referring to [54].

This effect efficiently depopulates the excited state of interest, the  $^3P$  manifold. At the same time, the multiphonon quenching efficiently populates the adjacent  $^1D_2$  level which in turn yields strong emission at 595 nm. The excited state lifetime of the  $^1D_2$  level is limited by cross-relaxations and comparable to bulk crystals for small nanocrystals with low doping concentrations. From this spectroscopic characterization the excited state lifetimes and quantum yields served as control parameters for the Monte Carlo simulations.

The numerical approach and the respective investigations are presented in Part III of this thesis. The model treats every lanthanide ion in a nanocrystal individually including all relevant processes such as energy transfers, cross-relaxations, and multiphonon quenching to the surrounding medium. This provides the necessary spatial resolution of the excitation dynamics. With this model, the excited state lifetime and quantum yield of the size series could be predicted with a maximum uncertainty of 12.6%. A prominent strategy from the literature to suppress quenching was applied and the model was extended by adding a neutral shell around the nanocrystals [60]. The neutral shell almost completely suppressed the multiphonon quenching resulting in improved excited state lifetimes and quantum yields. Additional simulations of individual nanocrystals revealed oscillations of the excitation energy in some nanocrystals for a short period that point toward a new type of energy trapping in lanthanide nanocrystals.

The ability to predict the excited state lifetime and quantum yield renders the presented Monte Carlo approach a powerful tool for nanocrystal research that is not restricted to the chosen model system,  $\text{LiYF}_4:\text{Pr}^{3+}$ , but applicable to any kind of lanthanide nanocrystals. In the future, this approach will contribute to a deeper understanding of the dynamics in nanocrystals and, in particular, allow to study spatiotemporal effects. In addition, it will enable the numerical, i.e., artificially intelligent optimization of nanocrystals for excellent spectroscopic properties and thus open up new fields of application in photonics. For example, a combination of such optimized nanocrystals with established fiber technology might allow for visible continuous wave fiber lasers or telecom-network compatible quantum memories. „There is plenty of room at the bottom“ [30].



## NANOCRYSTAL SYNTHESIS AND CHARACTERISTICS

---

### Contents

---

2.1	Synthesizing Rare Earth Doped Nanocrystals . . .	9
2.1.1	Synthesis of Monodispersed $\text{LiYF}_4:\text{Pr}^{3+}$ Nanocrystals . . . . .	11
2.2	Structural Properties of $\text{LiYF}_4:\text{Pr}^{3+}$ Nanocrystals .	13
2.2.1	X-Ray Diffraction . . . . .	13
2.2.2	Transmission Electron Microscopy and Energy Dispersive X-Ray Spectroscopy . . . .	15
2.2.3	Flexibility and Precision of the Synthesis .	18
2.2.4	Sample Overview . . . . .	19

---

Existing approaches to synthesize  $\text{LiYF}_4:\text{Pr}^{3+}$  nano- and microcrystals yield broad size distributions (polydispersity) with sizes above 30 nm [61, 62]. At these scales, multiphonon quenching already constitutes a critical loss channel. A common strategy to decrease these losses is to add an undoped shell around the nanocrystals. However, this results in bigger nanocrystals and, consequently, increasing scattering losses. Smaller nanocrystal sizes around 10 nm are desirable to allow for thick shells that reduce multiphonon quenching while still preventing increased scattering. Such core-shell nanocrystals need to be optimized by carefully adjusting doping concentration, core size, and shell thickness. A numeric approach to achieve that is presented in Part III of this thesis. However, the existing synthesis approaches do not provide the needed flexibility and versatility which specifies the necessity of a synthesis route that allows for the synthesis of monodisperse nanocrystals with 10 nm size.

Such a synthesis was developed by Rajesh Komban and Christoph Gimmler at the Fraunhofer Center for Applied Nanotechnology (CAN) in Hamburg. They synthesized nine different nanocrystal samples, characterized their structural properties, and provided them for the investigations presented in this thesis. In this chapter, the synthesis approach and the structural characterization are briefly introduced.

### 2.1 SYNTHESIZING RARE EARTH DOPED NANOCRYSTALS

In this section, the general synthesis approach of nanocrystals is described to obtain small and monodisperse nanocrystals. Ideal monodispersity is reached if the size distribution can be described by a delta

function. In reality, nanocrystal sizes are often Gaussian distributed and exhibit a certain distribution width which is a measure for the monodispersity. The exact boundary between poly- and monodispersity is somewhat arbitrary, but if the full width at half maximum of the size distribution is narrower than about 20-30% of the average nanocrystal size, the distribution is considered monodisperse. Therefore, for 10 and 20 nm sized nanocrystals the size distributions should thus not exceed 3 and 6 nm respectively, to be called monodisperse.

In principle, synthesizing monodispersed nanocrystals consists of three phases as can be seen from the LaMer plot in Figure 2. First, the so called monomers are released. These are dissolved ions or molecules which aggregate and thus build the basis for the crystallization of solid state particles in solvents. During the synthesis process monomers are released by thermal decomposition when the reactants are heated above 200°. The monomer concentration increases due to the thermal decomposition of the reactants and reaches a critical level  $c_{min}$ . There are two different approaches for the first phase. Heating the reactants above their decomposition temperature is called heating method and injecting the reactants above this temperature is called injection method.

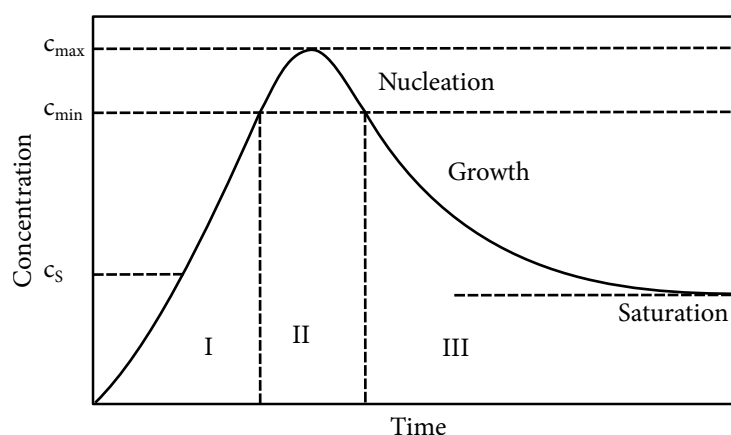


Figure 2: The LaMer plot summarized the three phases during the synthesis of nanocrystals, reproduced from [63].

Then, the second phase, the nucleation starts, which is why the concentration is called critical nucleation concentration. Above this concentration the nucleation rate strongly increases and monomers are used up to form seeds. The nucleation rate thus decreases with decreasing monomer concentration until nucleation stops below the critical concentration  $c_{min}$ . At this point, the solution consists of seed crystals, monomers and possibly reactants which continue to release further monomers.

In the last phase, the seed crystals grow via agglomeration of monomers. After decomposition of all reactants, the monomer concentration decreases further and reaches an equilibrium concentration.

This equilibrium is characterized by monomers accumulating to the particles and dissociating again.

In the this growth phase, two methods need to be distinguished: diffusion controlled growth and kinetically controlled growth. The growth rates of a particle in both cases can be predicted theoretically using Wagners growth law for spherical particles [64]. For very small particles which form at the beginning of either growth process, the growth velocity is negative so that formed seed crystals dissolve. Once a critical radius  $r_{\text{crit}}$  is reached the particles begin to grow.

In the case of kinetically controlled growth the growth velocity is always positive which means that big particles grow faster than smaller ones. This leads to an ongoing broadening of the size distribution and needs to be prevented if monodispersed nanocrystals are needed. In contrast, in the case of diffusion controlled growth, the slope of the growth rate exhibits a point of inflection. Up to this point the particles grow and the size distribution broadens. Once this point is reached small particles grow faster than bigger ones. The size of particles with a small size in the beginning of the synthesis thus approach the bigger sizes during the synthesis progress which results in a narrowing of the size distribution. Stirring of the solution during synthesis avoids kinetically controlled growth and thus allows for monodisperse size distributions.

During the growth phase, monomers are consumed which reduces the ratio of monomer concentration and equilibrium concentration, the so-called supersaturation  $S$  in the reaction volume. This results in a shift of the critical radius  $r_{\text{crit}}$  to greater values because it is inversely proportional to  $\ln S$  [65]. Therefore, particles with  $r < r_{\text{crit}}$  dissolve while particles with  $r > r_{\text{crit}}$  grow by consuming the monomer released through the dissolution of the smaller particles. The critical radius  $r_{\text{crit}}$  hence remains in the maximum of the size distribution so that small particles shrink and big particles grow. This leads to a tail of the size distribution which reaches down to particle sizes of  $r = 0$ . As a result, the absolute number of particles is reduced, the size distribution broadens and takes a characteristic shape. This process is called Ostwald-Ripening and needs to be prevented by adding monomer during the synthesis to avoid broadening size distribution of the nanocrystals during the growth phase.

### 2.1.1 *Synthesis of Monodispersed $\text{LiYF}_4:\text{Pr}^{3+}$ Nanocrystals*

Lithium-based Yttrium tetrafluorides have mostly been synthesized with size distributions around 40 nm or bigger [12, 45, 66, 67]. Therefore, the general description on the synthesis given above needs some customization to yield monodispersed  $\text{LiYF}_4:\text{Pr}^{3+}$  nanocrystals. The synthesis described below has been developed at Fraunhofer CAN and is briefly described in the following [54].



In the synthesis, an appropriate amount of  $\text{YCl}_3$  and  $\text{PrCl}_3$  (each 99.9%) in methanol was mixed with oleic acid and octadecene (both 20 ml and technical grade) in a three-necked round bottom flask. The flask was connected to a reflux condenser, a temperature sensor, and a septum resulting in a modified Schlenk-line setup. The mixture was stirred and heated to  $170^\circ\text{C}$  for 30 min under  $\text{N}_2$  atmosphere and then cooled down to  $50^\circ\text{C}$ . Next, the mixture was degassed at  $100^\circ\text{C}$  in a vacuum ( $< 1$  mbar). Afterward,  $\text{LiOH}$  (3 mmol, 99.995%, Sigma Aldrich) was added under  $\text{N}_2$  flow and then stirred under vacuum for another 30 min. Subsequently, 12 mmol  $\text{NH}_4\text{F}$  (99.99%, Sigma Aldrich) was added and the mixture was heated up to  $300^\circ\text{C}$  for 90 min. After cooling below  $30^\circ\text{C}$  the mixture was precipitated with 1:1 addition of ethanol and centrifuged for collection. The residue was redispersed in toluene (10 ml, 99.8%, Sigma Aldrich). If necessary, the washing step was repeated and finally, the precipitated nanocrystals were redispersed in toluene (5 ml). The ratio and amount of  $\text{YCl}_3$  and  $\text{PrCl}_3$  were tuned to obtain the different praseodymium doping concentrations while the  $\text{LiOH}$  content was tuned to obtain different sizes.

The nitrogen atmosphere serves to prevent oxidation since it has been suggested that other fatty acids present in the oleic acid might oxidize or form more complex structures in presence of oxygen at temperatures employed during synthesis. This results in a yellowish/brownish coloration of the reaction mixture during heat-up and, thus, results in distortions of the spectroscopic properties as will be discussed in [Chapter 6](#). While using oleic acid in nanocrystal syntheses is quite common [68], the appropriate amount of oleic acid, the right formation temperature and the timing for adding oleate precursors is especially crucial to obtain high-quality  $\text{LiYF}_4:\text{Pr}^{3+}$  nanocrystals and prevent dissociation into trifluoride. Using the appropriate amount of oleic acid in the reaction mixture effectively controls the size distribution and provides a stable dispersion without any visible sedimentation even after several months of storing.

This synthesis route has been employed at Fraunhofer CAN to synthesize nine samples in total that were used in this thesis. Four of them constitute a series with different doping concentrations at a size of about 10 nm which is called *concentration series*, subsequently. These samples were synthesized in one batch. For the other five samples, the doping concentration is constant at 5 at% but the size varies. These samples were synthesized in two different batches which might result in slightly different properties as discussed in [Chapter 7](#). These samples will be further referred to as *size series*.



2.2 STRUCTURAL PROPERTIES OF  $\text{LiYF}_4:\text{Pr}^{3+}$  NANOCRYSTALS

Bulk crystals of  $\text{LiYF}_4:\text{Pr}^{3+}$  are commercially available for application, e.g., as laser crystals. Therefore, the structural and spectroscopic properties were already subject to various publications [7–11, 69–74]. While the spectroscopic properties are presented in Part II of this thesis, the structural properties are presented in this chapter.

In  $\text{LiYF}_4:\text{Pr}^{3+}$ , trivalent rare earth ions typically substitute the Yttrium ions which are also trivalent. While the ionic radius of Yttrium is  $R_{\text{Y}} = 1.04 \text{ \AA}$  Praseodymium is slightly bigger with  $R_{\text{Pr}} = 1.14 \text{ \AA}$ . Therefore, incorporated Praseodymium ions induce local stress in the crystal lattice resulting in lattice defects that are produced in the surroundings for stress compensation. Such defects may lead to clustering of the dopant ions which in turn causes a variety of distorted lattice sites. This effect influences the spectroscopic properties of small nanocrystals with high doping concentrations used in the present thesis as further investigated in [Chapter 7](#).

[Table 1](#) gives an overview on important structural and optical properties of bulk  $\text{LiYF}_4$ .

$\text{LiYF}_4$  single crystals exhibit a large anisotropy due to the high aspect ratio of the lattice constants. This results in polarization dependence of absorption and emission cross sections. However, this effect cannot be optically resolved in nanocrystal spectroscopy when the nanocrystals are randomly oriented in an organic solvent. However, this the contribution of the different nanocrystal axes needs to be accounted for when fitting the absorption spectra (c.f. [Chapter 7](#)).

Once synthesized, the nanocrystals need to be analyzed thoroughly to verify their properties such as crystal structure, size, and doping concentration. For this analysis, a set of three methods is typically used: X-Ray Diffraction (XRD), Transmission Electron Microscopy (TEM), and Energy Dispersive X-Ray (EDX) Spectroscopy. In this chapter, the structural characterization results of the nanocrystals are presented. This characterization was performed at Fraunhofer CAN. The results are summarized in [Section 2.2.4](#) and used for the simulations carried out in Part III.

### 2.2.1 X-Ray Diffraction

When a crystal is irradiated with monochromatic X-rays they will be diffracted at the crystal lattice and the crystal structure can be calculated from the observed diffraction pattern. This method can be applied for nanocrystalline powders. For the nanocrystals used in the present thesis, XRD has been used to verify the crystalline structure, dimensions of the unit cell, and the density of the nanocrystals.

For the measurement, 50  $\mu\text{l}$  of the obtained dispersions were dried on a Si wafer and analyzed in an X-ray diffractometer (PANalytical X'PERT Pro) equipped with a Cu  $K\alpha$  X-ray source (154 pm).

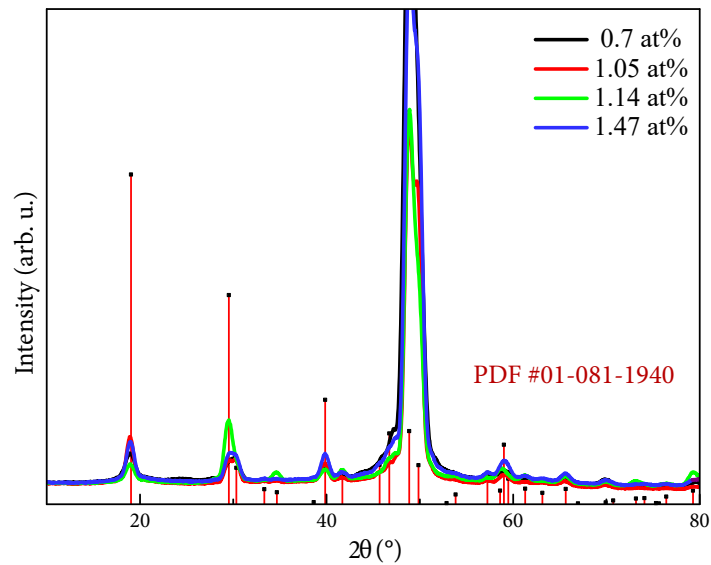


Figure 3: XRD results for the concentration series. The measured diffractograms match well to the Powder Diffraction File #01-081-1940 which is assigned to  $\text{LiYF}_4$ . These measurements were performed and provided by the Fraunhofer Center for Applied Nanotechnology.

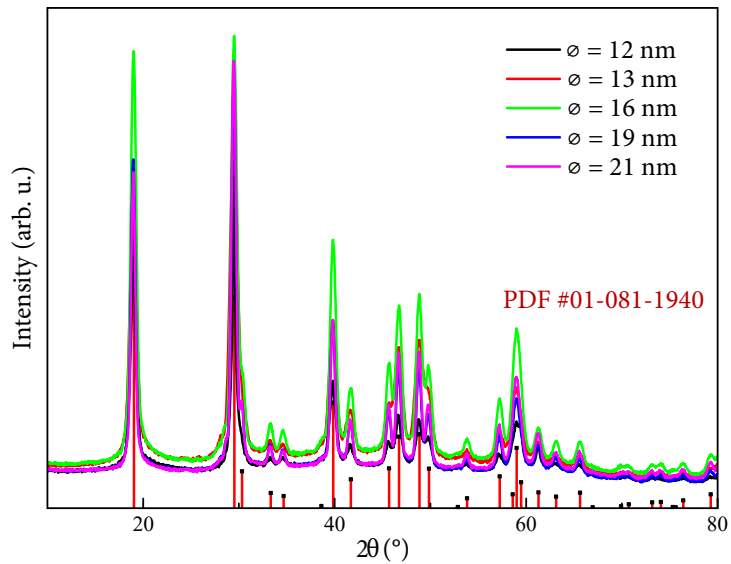


Figure 4: XRD results for the size series. The measured diffractograms match well to the Powder Diffraction File # 01-081-1940 which is assigned to  $\text{LiYF}_4$ . These measurements were performed and provided by the Fraunhofer Center for Applied Nanotechnology.

PROPERTY	BULK CRYSTAL	NANOCRYSTAL
Formula units per unit cell Z	4	4
Lattice constants	$a = 5.160 \text{ \AA}$ $c = 10.850 \text{ \AA}$	$a = 5.171 \text{ \AA}$ $c = 10.748 \text{ \AA}$
Refractive indices at 639.5 nm	$n_o = 1.453$ $n_e = 1.475$	
Effective phonon energy $\hbar\omega_{eff}$	$460 \text{ cm}^{-1}$	
Density $\rho$	$3.99 \text{ g/cm}^3$	$3.96 \text{ g/cm}^3$
Melting temperature	$850 \text{ }^\circ\text{C}$	

Table 1: Important structural and optical properties of bulk [75–78] and nanocrystalline  $\text{LiYF}_4$ .

As expected, the diffractogram revealed a tetragonal crystal structure of all synthesized nanocrystals since the diffraction pattern agrees well with bulk  $\text{LiYF}_4$  (PDF #01-081-1940), see Figure 3 and Figure 4. Furthermore, the unit cell parameters are  $a = 5.171 \text{ \AA}$  and  $c = 10.748 \text{ \AA}$ , and the nanocrystals have a density of  $3.96 \text{ gcm}^{-3}$  confirming the bulk values summarized in Table 1.

### 2.2.2 Transmission Electron Microscopy and Energy Dispersive X-Ray Spectroscopy

Transmission electron microscopes (TEM) use electron beams to image objects with resolutions in the sub-nanometer region. From TEM images, the size distribution of nanocrystals can be determined by measuring the dimensions of at least 300 individual nanocrystals [79]. In this thesis, this measurement was performed using the software ImageJ [80]. In the TEM images, the nanocrystals appear as rhombic structures which is the 2-dimensional projection of their squared bipyramidal shape [12]. Due to this shape, both, the long and short edge lengths were measured for each nanocrystal. The data was plotted in a histogram together with a gaussian fit which yielded the central value and full width at half maximum.

In energy-dispersive X-ray spectroscopy, the atoms of a sample are excited with an electron beam resulting in the emission of characteristic X-rays that can be analyzed spectroscopically. From the spectrum, the element composition of the sample can be determined. For the samples used in the present thesis, this method has been applied to verify the Praseodymium doping concentration.

For the electron microscopy,  $10 \mu\text{l}$  of the dispersions were dried on a copper grid and images were taken in a TEM (JEOL JEM-1011) operated at 100 kV. An EDX spectrometer (JEOL JEM 2200 FS, FEG

cathode, 200 kV, Oxford X-Max 100TLE, SDD 100 mm<sup>3</sup>) attached to the TEM was used to take X-ray spectra of at least three different areas for the elemental content analysis of the nanocrystals.

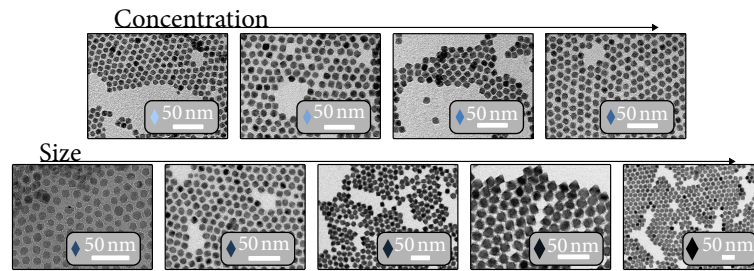


Figure 5: TEM images of all samples used in this thesis. More detailed images can be found in [Section 15.1](#). Measurements were performed and provided by the Fraunhofer Center for Applied Nanotechnology.

Well-defined individual nanocrystals having a size of around  $\approx 10 \dots 20$  nm are clearly evident in the respective TEM images, see [Figure 5](#) for an overview. The complete set of detailed TEM images for all samples used in this thesis can be found in Appendix A. Depending on the viewing angle and the nanocrystal alignment on the TEM grid, the bipyramidal shape can easily be mistaken for diamond or hexagonal morphologies as described in publications on LiYF<sub>4</sub> nanocrystals doped with other lanthanide ions [12]. Such mistake can be avoided by recording high resolution TEM images as provided in Appendix A where the tetragonal bipyramidal shape is visible.

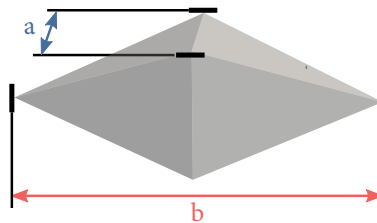


Figure 6: 3D sketch of the bipyramidal nanocrystals.

To extract the size distribution, the particles depicted on the TEM image were measured with a scientific image analysis program (ImageJ). To characterize the bipyramidal shape of the nanocrystals, two measures  $a$  and  $b$  were taken, see [Figure 6](#). The diameter size distribution becomes statistically representative if more than 300 nanocrystals are considered [79]. The size distributions of all samples were analyzed and a gaussian function was fitted to the data to determine the average sizes and size distributions, see [Figure 7](#) and [Figure 8](#). A direct relation between the doping concentration and the nanocrystal size could not be observed.

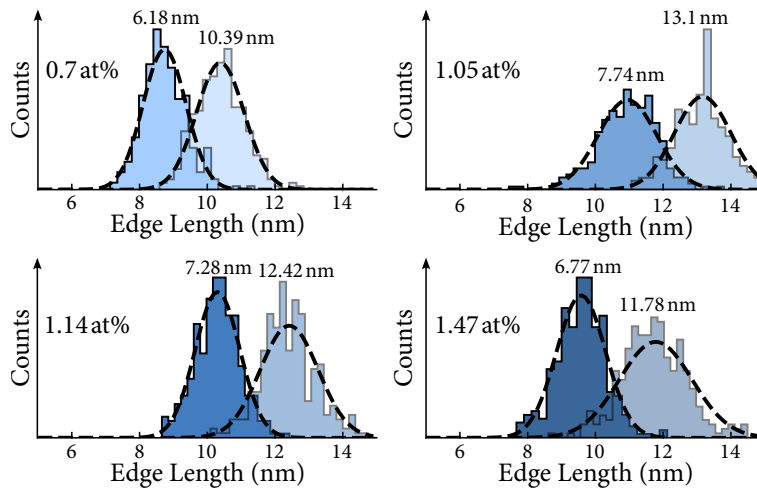


Figure 7: Normalized size distribution of the samples of the concentration series. A gaussian function was fitted to the histograms to determine the average size.

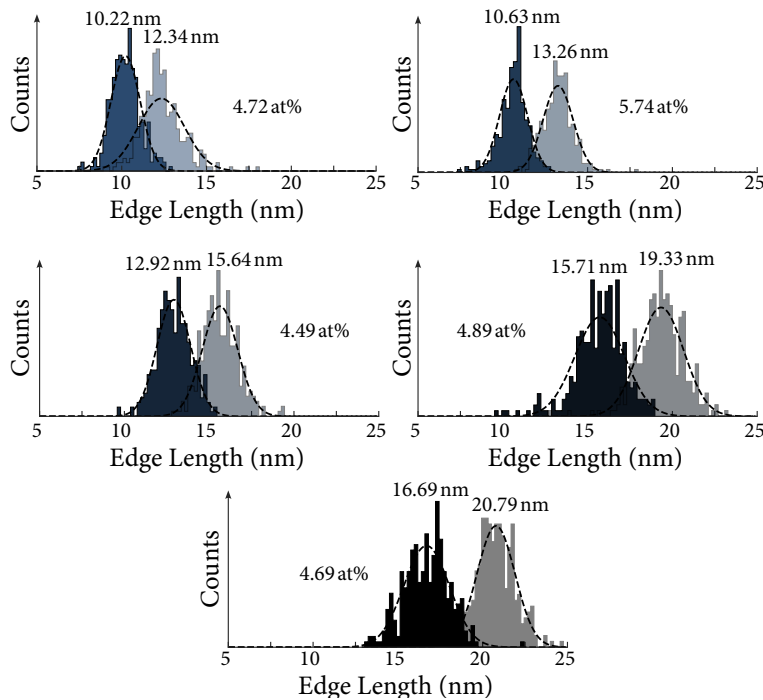


Figure 8: Normalized size distribution of the samples of the size series. A gaussian function was fitted to the histograms to determine the average size.

Mapping analysis and line scans (see Appendix A) indicate that the  $\text{Pr}^{3+}$  ions are homogeneously distributed in the nanocrystals. The doping concentration was determined from the EDX spectra and the respective values are summarized in [Table 2](#).

### 2.2.3 Flexibility and Precision of the Synthesis

In Part III, a numerical approach is presented that can decode the excitation dynamics in e.g.  $\text{LiYF}_4:\text{Pr}^{3+}$  nanocrystals and enables prediction of these dynamics. Consequently, the numerical approach will be employed in the future to optimize nanocrystals and develop new nanocrystal designs with increased complexity, e.g., structures with multiple shells, new geometries, or even doping gradients. Such designs pose high demands on the flexibility and precision of the synthesis route for such nanocrystals. This chapter highlights how flexibility and precision make up the existing synthesis route.

For the doping of the concentration series, four low level concentrations, 0.65, 1, 1.3, and 1.5 at%, were chosen as target values. These values include the optimum doping concentration of 0.65 at% known from bulk crystals. The doping concentration in bulk crystals is mainly limited by concentration quenching [8]. Due to the strong impact of surface ions in nanocrystals, concentration quenching is expected to be lower and hence the anticipated optimum doping concentration is slightly larger compared to the bulk case. The actual  $\text{Pr}^{3+}$  ion concentration in the nanocrystals was measured via EDX as described above. The corresponding mean values are 0.7, 1.05, 1.14, and 1.47 at%, respectively, and deviate by a maximum of 12% from the targeted doping concentrations. For the size series, a doping concentration of 5 at% was targeted. The mean values revealed by EDX for these samples deviated by a maximum of 15% from the targeted concentrations. These results are summarized in Figure 9.

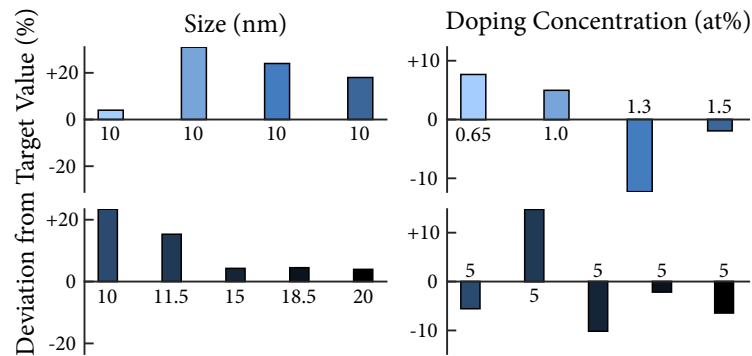


Figure 9: Percent deviation of the doping concentrations and sizes that were targeted in the synthesis of the samples used in this thesis. The actually obtained values are summarized in Table 2.

For size distribution of the concentration and size series, average sizes of 10 nm and 10, 11.5, 15, 18.5, and 20 nm were targeted, respectively. It can be seen from Figure 9 that the targeted average sizes were reached, though, with a maximum deviation of 25% for the concentration series and 22% for the size series. Furthermore, strong monodispersity is verified by the standard deviation of the size dis-









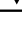
C (AT%)	A (NM)	B (NM)	$N_{\text{IONS}}$	$\rho$ ( $\text{nm}^{-3}$ )	MARKER
<b>0.7</b>	6.2	10.4	0.6	13	
<b>1.05</b>	7.7	13.1	1.1	38	
<b>1.14</b>	7.3	12.4	1.2	35	
<b>1.47</b>	6.8	11.8	1.4	37	
4.72	10.2	<b>12.3</b>	6.7	281	
5.74	10.6	<b>13.3</b>	8.5	398	
4.49	12.9	<b>15.6</b>	8.6	582	
4.89	15.7	<b>19.3</b>	11.4	1154	
4.69	16.7	<b>20.8</b>	10.8	1251	

Table 2: Overview of the samples and the data extracted from the structural material analysis. Here,  $c$  is the concentration,  $\rho$  is the ion density, and measures  $a$  and  $b$  are referenced in [Figure 6](#). Every sample was assigned an individual marker (color and size) that represents that sample in the plots throughout this thesis.

tributions that is below 10% of the average nanocrystal size for all samples (c.f. [Figure 7](#) and [Figure 8](#)).

Alltogether, monodisperse nanocrystals sized in a range of 10 – 20 nm and doped with low and middle concentrations can be synthesized with equally high precision constituting the high flexibility of the synthesis route. The present route constitutes a strong basis that can be improved to meet the demands of such future designs.

#### 2.2.4 Sample Overview

The concentration series consists of 4 samples with a comparable size distribution at around 10 nm. The doping concentration of these samples increases from 0.7 to 1.47 at%. Furthermore, the size series consists of 5 samples with comparable doping concentrations of approximately 5 at%. The size of these samples increases from around 12 to 21 nm. From the size distribution and the doping concentration, the average number of  $\text{Pr}^{3+}$  ions were calculated for bipyramids with given dimensions. The nanocrystals in the concentration series contain less than 40 ions, those of the size series between 250 and 1300 ions.

The resulting material parameters are summarized in [Table 2](#) and were used as input parameters to the simulations.





---

**Contents**


---

3.1	The Free Lanthanide Ion . . . . .	22
3.2	Influence of the Crystal Field . . . . .	25
3.3	Trivalent Praseodymium . . . . .	25

---

This chapter provides the basic theoretical background for the spectroscopic investigations in this thesis. First, a general introduction to trivalent rare earth ions, and  $\text{Pr}^{3+}$  ions in particular, will be given with focus on their energy level structure and the influence of the crystal field. The energetic relations of trivalent praseodymium in the crystal field is of particular importance for understanding the spectroscopic investigations in Part II. A broad overview on these topics can be found in the textbooks of *Henderson and Imbusch* as well as *Liu and Jacquier* [81, 82].

Rare earth ions provide distinct energy level systems which comprise excellent properties for lasing [3, 81], phosphors [13–15, 83], or even quantum memories [5, 84]. They are defined as one set of 17 chemical elements in the periodic table comprising the lanthanides, which are the 15 elements from Lanthanum through Lutetium with atomic numbers  $Z = 57 - 71$  as well as the chemically similar elements Scandium ( $Z = 21$ ) and Yttrium ( $Z = 41$ ). The following discussion will address the lanthanides in general and Praseodymium in particular.

The electron configuration of lanthanides is  $[\text{Xe}](4f)^n(5d)^x(6s)^2$  with  $x = 1$  for Lanthanum, Gadolinium, and Lutetium. For these elements  $n = 0$ ,  $n = 7$ , and  $n = 14$ , respectively. For Cerium through Ytterbium,  $x = 0$  and  $n = 2$  through  $n = 13$ .

When incorporated in an ionic crystal the lanthanides are usually present as trivalent ions. Trivalent lanthanides have the electron configuration  $[\text{Xe}](4f)^{n+x-1}$ .

Optical transitions of trivalent lanthanide ions occur in the inner 4f and 5d orbitals which are only partially occupied. In contrast, the 5s and 5p orbitals are completely filled. They shield the 4f electrons from influences of the crystal field resulting in low variations of the 4f levels in different environments. Due to the shielding through the outer orbitals the transition linewidths are narrow and the lifetimes are high compared to those in other laser active ions like transition metals [81].

### 3.1 THE FREE LANTHANIDE ION

The energy level scheme of a lanthanide ions gives information about possible transitions and ion-ion interactions. Consequently, it is of basic importance for spectroscopy experiments presented in Part II as well as for identification of e.g. cross-relaxations that are relevant to the numerical approach presented in Part III of this thesis.

To calculate the energy level scheme of lanthanide ions, the systems Hamiltonian has to be determined first. Then, the Schrödinger equation has to be solved. The Hamiltonian  $\mathcal{H}$  for an N-electron system considering both, the Coulomb interaction between the electrons and the spin-orbit interaction is

$$\mathcal{H} = \sum_i^N \left( -\frac{\hbar^2}{2m_e} \Delta_{r_i} - \frac{Ze^2}{4\pi\epsilon_0 r_i} + \xi(r_i) \vec{s}_i \cdot \vec{l}_i \right) + \sum_{i>j} \frac{e^2}{4\pi\epsilon_0 r_{ij}} \quad (1)$$

with the reduced Planck constant  $\hbar$ , mass of an electron  $m_e$ , charge of an electron  $e$ , and the vacuum permittivity  $\epsilon_0$ . The variables in this equation are the distance to the nucleus  $r_i$  as well as the distance between the electrons  $r_{ij} = |\vec{r}_i - \vec{r}_j|$ . The function  $\xi(r_i)$  has the form

$$\xi(r_i) = \frac{1}{4\pi\epsilon_0} \frac{Ze^2}{2m_e^2 c^2 r^3}. \quad (2)$$

Furthermore,  $\vec{s}_i$  and  $\vec{l}_i$  are the spin and angular momentum of every electron, respectively.

$\mathcal{H}$  consists of four terms: The first one describes the kinetic energy while the second one stands for the energy of the electrons in the central field of the nucleus. The third and fourth describe the spin-orbit interaction and the Coulomb interaction, respectively.

Solving this equation would yield the energetic states of the ion. However, the last term prevents separation to single particle differential equations. An analytical solution thus cannot be found for systems with more than one electron. The so-called central field approximation is used to circumvent these difficulties by reducing the system to a radial, effective central field without electron-electron interactions. A further reduction is obtained by neglecting the comparatively small contribution of the spin-orbit interaction. To correct the resulting Hamiltonian  $\mathcal{H}_0$  perturbation terms of first order can be used: The non-radial Coulomb interaction between the electrons,  $\mathcal{H}_{ee}$  is added as well as the spin-orbit coupling of the electrons,  $\mathcal{H}_{so}$ . Further corrections can be neglected, since their influence is small compared to the crystal field interaction which will be discussed later.

In the central field approximation, [Equation 1](#) can be reduced:

$$\mathcal{H}_0 = \sum_i^N \left( -\frac{\hbar^2}{2m_e} \Delta_{r_i} + V(r_i) \right) \quad (3)$$

The first term again describes the kinetic energy and  $V(r_i)$  stands for the central field potential of the  $i$ -th electron at a distance  $r_i$  from the nucleus.

The central field potential can be determined using the iterative Hartree-Fock-method, details can be found in [81]. Using this method, the wavefunction of a single electron can be obtained by assuming a self-consistent potential. With the new resulting total potential this procedure will be repeated until the wavefunctions do not vary furthermore. As the Hamiltonian in Equation 3 is separable, the time-independent Schrödinger equation is

$$\mathcal{H}_0\psi_0 = E_0\psi_0 \quad (4)$$

with the energy eigenvalues  $E_0$ . The solution  $\psi_0$  of this equation is the product of the eigenstates of the single electron wave functions  $|n_i l_i m_l m_s\rangle$ :

$$\psi_0 = \prod_{i=1}^N |n_i l_i m_l m_s\rangle \quad (5)$$

with the principal quantum number  $n_i$  and the orbital angular momentum  $l_i$  of the  $i$ -th electron. As the magnetic quantum numbers  $m_l$  and the spin quantum number  $m_s$  are degenerated in this model, the energy eigenvalues depend only on  $n_i$  and  $l_i$ . This set of quantum numbers is called the electron configuration.

Pauli's exclusion principle states that an electron in an ion cannot occupy the same quantum state that is already occupied by another electron. The total wave function  $\psi_0$  thus has to be completely antisymmetric. To ensure this,  $\psi_0$  is written as Slater determinant of the single electron wave function.

The nonradial part of the Coulomb interaction  $\mathcal{H}_{ee}$  between the individual electrons and the spin-orbit interaction are now considered as additional perturbation terms. Thus the free ion Hamiltonian  $\mathcal{H}_{FI}$  results as

$$\mathcal{H}_{FI} = \mathcal{H}_0 + \mathcal{H}_{ee} + \mathcal{H}_{so} \quad (6)$$

with the electron-electron perturbation term

$$\mathcal{H}_{ee} = \sum_{i<j=1}^N \frac{e^2}{4\pi\epsilon_0} |\vec{r}_i - \vec{r}_j|^{-1} - \sum_{i=1}^N \left( \frac{Ze^2}{(4\pi\epsilon_0)r_i} - V(r_i) \right). \quad (7)$$

Here  $e$  is the elementary charge,  $Z$  the atomic number,  $\epsilon_0$  the permittivity of free space, and  $|\vec{r}_i - \vec{r}_j|$  the distance between the respective

electrons. The summation is over the outer electrons. The electron-electron interaction causes a splitting of the  $4f^n$ -state as is depicted in Figure 10. This splitting takes place in distinct LS-levels and is also called Russel-Saunders-coupling. Here, the total orbital angular momentum is  $L = |\vec{L}|$  with  $\vec{L} = \sum_i \vec{l}_i$ , and the total electron spin is  $S = |\vec{S}|$  with  $\vec{S} = \sum_i \vec{s}_i$ .

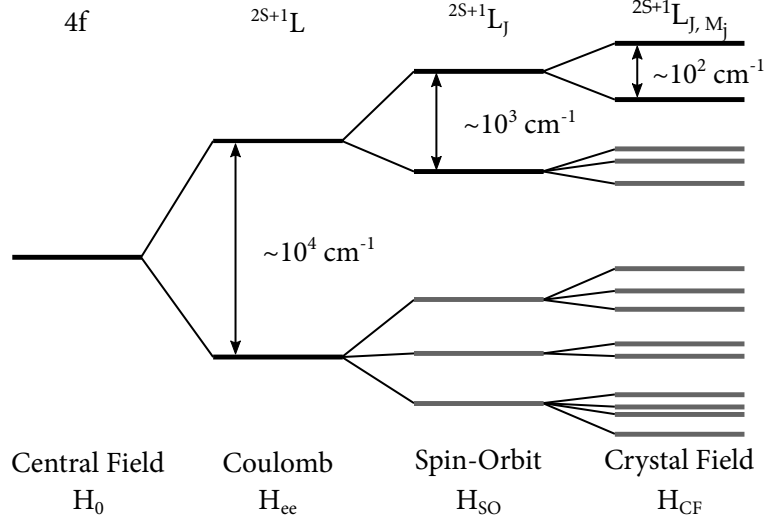


Figure 10: Principle overview of the effect of the different perturbation terms on the energy level splitting.

The third term in Equation 6 denotes the spin-orbit perturbation term

$$\mathcal{H}_{so} = \sum_{i=1}^N \frac{1}{2m^2c_0^2} \cdot \frac{1}{r_i} \cdot \frac{dV(r_i)}{dr_i} \cdot (\vec{l}_i \cdot \vec{s}_i), \quad (8)$$

with the vacuum speed of light  $c_0$ . The summation is over the outer electrons.

The perturbation terms are treated with descending order of their strength. Depending on the coupling strength of the electrons a further splitting takes place. In case of a weak spin-orbit interaction compared to the electron-electron interaction, the LS-coupling is valid as described above. The total orbital angular momentum  $\vec{L}$  and the total spin  $\vec{S}$  then couple to the total angular momentum  $\vec{J} = \vec{L} + \vec{S}$ . Every LS-multiplet is  $J$ -fold degenerate and splitted into manifolds due to the influence of spin-orbit interaction. In case of a dominating spin-orbit interaction, the angular momenta of the electrons  $\vec{j} = \vec{l}_i + \vec{s}_i$  are coupled to form the total angular momentum  $\vec{J} = \sum_i \vec{j}$ . Such  $j-j$ -coupling applies only for heavy elements as plumbum. As lanthanide elements are located on a middle position in the periodic table, the influence of both perturbation terms is comparable. For this so called intermediate coupling the eigenstates are linear combinations of several LS-states of same quantum number  $\vec{J}$ . The intermediate coupling

scheme can be developed from the LS-coupling scheme. Therefore the nomenclature for the LS-coupling  $^{2S+1}L_J$  is also suitable for the intermediate coupling. The eigenstates are designated according to Hund's rule. Furthermore, every multiplett is  $2S + 1$ -fold degenerate in  $M_j$  as is depicted in [Figure 10](#) [81].

### 3.2 INFLUENCE OF THE CRYSTAL FIELD

A lanthanide ion incorporated in a dielectric crystal will experience the electrostatic influence of the crystal field. The Hamiltonian is rewritten as:

$$\mathcal{H} = \mathcal{H}_{\text{FI}} + \mathcal{H}_{\text{CF}} \quad (9)$$

$$= \mathcal{H}_0 + \mathcal{H}_{ee} + \mathcal{H}_{so} + \mathcal{H}_{\text{CF}} \quad (10)$$

with  $\mathcal{H}_{\text{FI}}$  as defined in [Equation 6](#) and  $\mathcal{H}_{\text{CF}}$  representing the energy of interaction between the lanthanide ions and the surrounding crystal field. Eigenstates and eigenvalues of the Hamiltonian  $\mathcal{H}$  can be determined by distinguishing three regimes which depend upon the relative sizes of the terms in [Equation 10](#).

For trivalent lanthanide ions the weak crystal field regime  $\mathcal{H}_{\text{CF}} \ll \mathcal{H}_{ee}, \mathcal{H}_{so}$  is appropriate since the optically active 4f electrons are shielded by their outer filled  $5s^2 5p^6$  orbitals. The influence of the weak crystal field can be introduced as an additional perturbation  $\mathcal{H}_{\text{CF}}$  in [Equation 6](#) which can be written as:

$$\mathcal{H}_{\text{CF}} = \sum_i \sum_l \mathcal{H}_{\text{CF}}(\vec{r}_i, \vec{R}_l) \quad (11)$$

Summation is over the electrons  $i$  and the number of adjacent ions  $l$  with the mean coordinate  $\vec{R}_l$ .

The crystal field influences the energy level structure in two different ways. Due to a spreading outwards of the 4f-electron charge distribution within the crystal, the energy level structure of the ion is red-shifted compared to the free-ion which is called the nephelauxetic effect [81, 85]. Besides, the crystal field is breaking the  $M_j$ -degeneracy of the  $^{2S+1}L_J$ -manifolds. This so called Stark effect is weak since for lanthanide ions the optically active 4f electrons are partially screened from the crystal field by their outer filled subshells. The splitting of the manifolds is usually in the order of a few  $100 \text{ cm}^{-1}$ .

### 3.3 TRIVALENT PRASEODYMIUM

Praseodymium is the third member of the lanthanides with the symbol Pr and atomic number  $Z = 59$ . The electron configuration of

atomic praseodymium is  $[\text{Xe}](4f)^3(6s)^2$ . Praseodymium most readily forms the 3+ oxidation state although the 2+ [86], 4+ [87], and 5+[88] oxidation states may exist in some solid compounds. In dielectric crystals such as  $\text{LiYF}_4$ , however, praseodymium is preferably incorporated in its trivalent oxidation state as  $\text{Pr}^{3+}$ . In this state, the electron configuration of praseodymium is  $[\text{Xe}](4f)^2$  resulting in two 4f electrons which can occupy 13 energy levels inside this 4f orbital. The highest 4f energy level  $^1S_0$  is located directly below the 4f5d

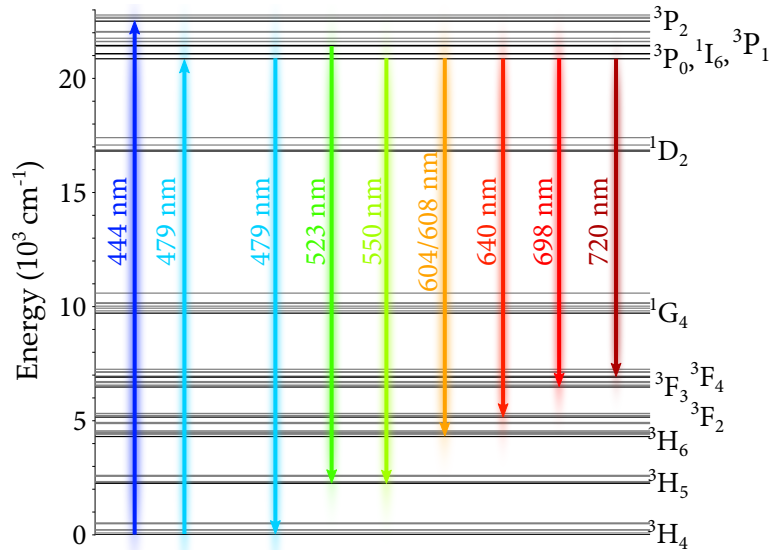


Figure 11: Energy level scheme of the  $4f^2$ -states in  $\text{Pr}^{3+}$  including Stark splitting and prominent absorption and emission transitions [73]. The energetically highest level  $^1S_0$  lies at around  $48\,000\text{ cm}^{-1}$  and is not shown as it is not of particular interest for transitions in the visible spectral range.

states at about  $48\,000\text{ cm}^{-1}$  [89]. To excite this energy level photons of wavelengths in the deep ultraviolet spectrum would be necessary. Regarding the visible spectrum addressed in this thesis, the energy levels above  $25\,000\text{ cm}^{-1}$  are not of further concern. Figure 11 shows the 12 energy levels of the  $4f^2$  states including Stark splitting which are of interest for emission in the visible. Especially by exciting the  $^3P_J$  manifold, several radiative transitions in the spectral range from the blue to the near infrared occur as implied in Figure 11. Several scientific publications on solid state lasers emitting in the visible spectrum report on the use of these transitions [7–11].

---

**Contents**


---

4.1	Intraionic Interaction . . . . .	27
4.1.1	Absorption . . . . .	28
4.1.2	Emission . . . . .	29
4.1.3	Nonradiative Transitions . . . . .	29
4.2	Interionic Interaction . . . . .	30
4.2.1	Overview on Interionic Energy Transfers . . . . .	30
4.2.2	Calculation of the Transfer Rates . . . . .	31
4.3	Particularities on the Nanoscale . . . . .	34
4.3.1	Local Field Effects on Nanocrystals . . . . .	35
4.3.2	Förster Transfer based Multi-Phonon Quenching . . . . .	36

---

This chapter provides a comprehensive description of the interaction of energy and matter. Whenever a lanthanide ion interacts with another boson or fermion, energy is either received or released from the particular ion. One can distinguish such interactions of energy and matter by *intraionic* and *interionic* processes. The first one is about interaction with bosons like photons or phonons, while in the latter the ion interacts with fermions like other ions. The explanations on the *intraionic* processes presented in this chapter, i.e., Absorption and Emission, are of particular relevance to the spectroscopic results presented in Part II because they form the fundamental understanding of spectroscopic observations. The *interionic* processes, on the other hand, are based on the model of *Förster* [90] and *Dexter* [91]. The particular interaction mechanisms play a central role in the numerical investigations in Part III. *Förster* energy transfer drives energy hopping inside lanthanide nanocrystals but also multiphonon quenching to the surrounding medium of the nanocrystals. *Dexter* energy transfer, on the other hand, drives energy migration inside the lanthanide nanocrystals. A broad overview on these topics can be found in the textbooks of *Svelto* and *Lakowicz* [3, 92].

#### 4.1 INTRAIONIC INTERACTION

Typical intraionic energy transfers involve photons in radiative transitions or phonons in non-radiative transitions. The basic radiative transitions are absorption, spontaneous emission and stimulated emission.

#### 4.1.1 Absorption

In principle, absorption can occur if an incident photons energy equals the energy difference between two energy levels and the lower energy level is occupied. The photon may then be annihilated while the ion is instantaneously excited to the upper energy level. The initial state of the ion may be either the ground or an excited state. The processes are then called ground state absorption (GSA) or excited state absorption (ESA), respectively. Absorption is mostly measured macroscopically and in case of nanomaterials, the absorption of dispersions in cuvettes of these materials are measured (c.f. [Chapter 5](#)). The intensity  $I$  of light transmitting a sample in  $z$ -direction can be described by Lambert-Beer's law for sufficiently small intensities (to exclude nonlinear absorption processes). The decrease of the incident light of intensity  $I_0$  then obeys the exponential relation

$$I(z) = I_0 \cdot e^{-\alpha \cdot z}. \quad (12)$$

$\alpha$  is called the absorption coefficient and can be used to calculate the absorption cross section  $\sigma_{abs}$

$$\sigma_{abs}(\lambda) = \frac{\alpha(\lambda)}{N}, \quad (13)$$

if the dopant concentration  $N$  within the transmitted volume is known. In order to increase the absorption cross section, the dopant concentration may be increased. However, this can lead to interionic effects such as concentration quenching which limits the maximum reasonable dopant concentration. An optimized doping concentration trades off between maximized absorption cross sections and minimized concentration quenching. In  $\text{LiYF}_4:\text{Pr}^{3+}$  bulk crystals, this optimum is assumed to be between 0.5 at% and 0.65 at%. In nanocrystal dispersions, maximizing the number of ions is a challenging task since the nanocrystal volume is only a fraction of the total dispersion volume. This thesis aims to provide a numerical tool that enables to optimize the number of ions in nanocrystals.

Once an ion emits a photon (see next section), that photon can be reabsorbed by the same class of ions. Reabsorption can thus result in a red shift of the emitted photons. However, it only becomes significant for a large overlap of absorption and emission spectra. In  $\text{LiYF}_4:\text{Pr}^{3+}$ , there are several overlaps of absorption and emission that can result in reabsorption. Photons emitted in the orange spectrum from the  $^3\text{P}_0$  level can for example be reabsorbed and excite Praseodymium ions to the  $^1\text{D}_2$  level. In the present thesis, however, this overlap gains more relevance for interaction between the ions, see [Section 4.2](#) and [Chapter 9](#).



### 4.1.2 Emission

An excited ion can spontaneously transition into any lower energy level releasing its energy as one photon. The transition rate  $A$  from an excited state  $|\psi_i\rangle$  to a lower state  $|\psi_j\rangle$  can be expressed through Fermi's golden rule

$$A_{i \rightarrow j} = \frac{2\pi}{\hbar} |V_{12}(\omega_0)|^2 \rho(\omega_0). \quad (14)$$

Herein,  $V_{12}(\omega_0)$  is the matrix element of the perturbation operator belonging to this particular transition. In other words,  $V_{12}(\omega_0)$  is the energy of interaction between an emitter and its electric self-field and  $\rho(\omega_0)$  is the density of states. The radiative decay of state  $|\psi_i\rangle$  can be obtained by summation over all transition rates to lower lying states

$$A_i = \sum_k A_{ik}. \quad (15)$$

The radiative lifetime of this state is

$$\tau_i = \frac{1}{A_i}. \quad (16)$$

The radiative lifetime denotes the energy storage capacity of the active medium. In  $\text{LiYF}_4:\text{Pr}^{3+}$  nanocrystals, the excitation is severely quenched as pointed out in Part II and III which results in a reduction of the excited state lifetime and quantum yield of the nanocrystals. The emission spectrum and the lifetimes can be used to calculate emission cross sections using the Fuchtbauer-Ladenburg (c.f. [Chapter 8](#)). A comparison of the emission cross sections of bulk and nanocrystals contributes to qualitatively understand the spectroscopic behaviour of the nanocrystals in Part II.

Stimulated emission can take place if an ion is in excited state  $|\psi_i\rangle$  and a photon of same amount of energy interact. The excited state then transits  $|\psi_i\rangle \rightarrow |\psi_j\rangle$  and a photon is emitted in the same direction as the incident photon featuring the same properties such as energy, polarization and phase. To obtain a net gain by stimulated emission population inversion has to be ensured. To being able to neglect such effects in the simulations presented in Part III, the initial excitation had to be kept below 50% of the total number of ions.

### 4.1.3 Nonradiative Transitions

Transitions of excited states  $|\psi_i\rangle$  to lower ones can also occur by excitation of one or more phonons in the crystal lattice. Within such multiphonon relaxation excitation energy directly transforms into heat.

Multiphonon relaxation into energetically close lower states depopulates the excited state fast and efficiently, resulting in a reduced radiative lifetime. The transition probability  $W_{nr}$  for such nonradiative process of  $n$ -th order depends on the crystal temperature and is described by [93].

$$W_{nr} = W_0 \cdot e^{-\alpha\Delta E} [1 - e^{-\frac{\hbar\omega_{eff}}{kT}}]^{-n}. \quad (17)$$

$W_0$  is an empirical parameter depending on the crystal lattice and  $\alpha$  describes the electron-phonon coupling, which is considered to be weak for 4f-electrons.  $\Delta E$  is the energy gap between the involved states and  $\hbar\omega_{eff}$  is the effective phonon energy of the lattice. The number of phonons which are involved to bridge the energy gap is given by  $n = \frac{\Delta E}{\hbar\omega_{eff}}$ .  $T$  and  $k$  are the temperature and the Boltzmann constant, respectively. Considering Praseodymium ions in an  $\text{LiYF}_4$  lattice, the temperature dependency is neglectable due to the lattices low phonon energies of  $460 \text{ cm}^{-1}$  [94].

On a nanoscale, materials may experience further multiphonon relaxation based on dipole-dipole interaction between the lanthanide ion and material which surrounds a nanocrystal. This mechanism occurs within distances of several nanometers and is thus able to quench energy out of the nanocrystal. A detailed explanation is given in [Section 4.3](#).

## 4.2 INTERIONIC INTERACTION

Excitation energy can be transferred from one ion to another without absorption or emission of photons. The energy is delivered from a donor  $D$  and received by the acceptor  $A$ . Within this processes, partly or even complete energy loss may occur. One can distinguish three different processes: energy migration, cross relaxation, and upconversion.

### 4.2.1 Overview on Interionic Energy Transfers

*Energy migration* is a resonant process. As it is depicted in [Figure 12\(a\)](#), the excitation energy from an ion is transferred to another ion without energy loss.

*Cross relaxation* starts with only the donor ion in the excited state. Within the interaction, a part of the energy is transferred to the acceptor ion so that both ions are in an excited state which is not the same. This situation is exemplarily shown in [Figure 12\(b\)](#). In lasers, this process is unwanted as it may depopulate the upper laser level.

*Upconversion* occurs if both donor and acceptor are in an excited state. The energy transfer excites the acceptor to a energetically higher state than the initial state as shown in [Figure 12\(c\)](#). The donor transits

in the respective energetically lower state which is often the ground state. One prominent example in the nanomaterial scientific community are Erbium/Ytterbium co-doped nanocrystals. The Yb ions within these particles absorb energy in the infrared. The excitation energy from at least two Yb ions is then transferred to the Er ion which then emits in the visible. Due to this nonlinear anti-Stokes pumping scheme, these nanocrystals exhibit low quantum yields and are therefore not suitable for efficient lasing.

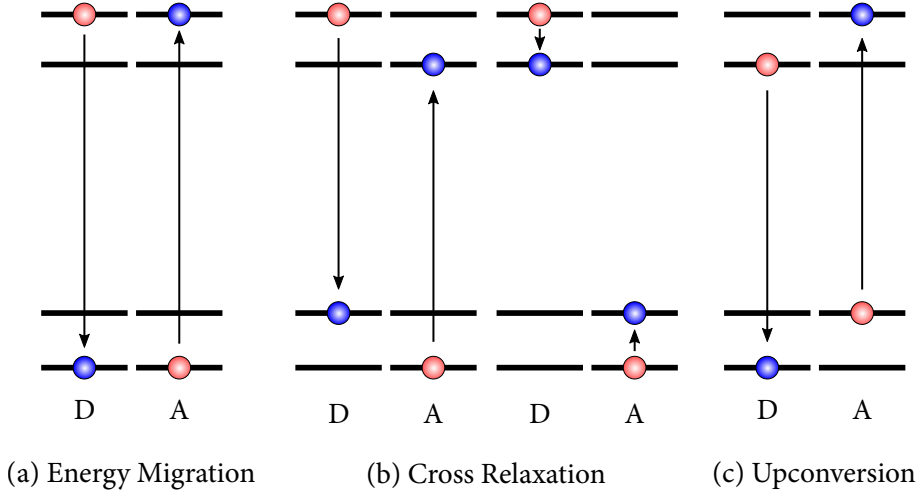


Figure 12: Adjacent lanthanide ions can experience these interionic energy transfer processes.

#### 4.2.2 Calculation of the Transfer Rates

The processes explained above base on two different interaction mechanisms which will be discussed in detail here. The energy transfer process from a donor to an acceptor can be written as



The Hamiltonian for this system reads

$$\mathcal{H} = \mathcal{H}_D + \mathcal{H}_A + V \quad (19)$$

with the perturbation part  $V$ .

Only two electron systems are involved in a transition, one from  $D$  and the second one from  $A$ . The wavefunctions for the initial state  $\psi_i$  with  $D^* + A$  and the final state  $\psi_f$  with  $D + A^*$  can be written as

$$\psi_i = \frac{1}{\sqrt{2}} (\psi_{D^*}(1)\psi_A(2) - \psi_{D^*}(2)\psi_A(1)) \quad (20)$$

$$\psi_f = \frac{1}{\sqrt{2}} (\psi_D(1)\psi_{A^*}(2) - \psi_D(2)\psi_{A^*}(1)) \quad (21)$$

with the numbers 1 and 2 referring to the electron systems involved. Note, that this representation only applies to a donor-acceptor system with one electron each. However, [Equation 20](#) and [Equation 21](#) are sufficient to explain the principle mechanism.

The coupling between the initial and final state is described by the interaction matrix element:

$$U = \langle \psi_i | |V| | \psi_f \rangle \quad (22)$$

which also can be written as

$$U = \langle \psi_{D^*}(1)\psi_A(2) | |V| | \psi_D(1)\psi_{A^*}(2) \rangle \quad (23)$$

$$- \langle \psi_{D^*}(1)\psi_A(2) | |V| | \psi_D(2)\psi_{A^*}(1) \rangle. \quad (24)$$

The first term is called Coulombic term and describes the return of the initially excited ion on D to the ground state while an electron system on A is simultaneously promoted to the excited state. The second term is called exchange term and describes an exchange of two electrons on D and A. The matrix element can thus be written as a sum of these two terms:

$$U = U_C - U_{ex} \quad (25)$$

In the following, both terms are treated separately as they lead to different outcomes.

#### 4.2.2.1 Dipole-Dipole Energy Transfer

The Coulombic term can be expanded into a multipole-multipole series

$$U = U^{dd} + U^{dq} + U^{qd} + U^{qq} + \dots \quad (26)$$

which can be approximated by the predominant dipole-dipole term  $U^{dd}$  for point dipoles. The higher order terms  $U^{dq}$ ,  $U^{qd}$ , and  $U^{qq}$  for dipole-quadrupole, quadrupole-dipole and quadrupole-quadrupole interaction are thus neglected and will not be discussed further.

The dipole-dipole interaction between the transition dipole moments  $\mu_D$  and  $\mu_A$  of the transition in [Equation 18](#) can be expressed as

$$U_{dd} = \alpha \frac{\vec{\mu}_D \cdot \vec{\mu}_A}{r^3} (\cos \Theta_{DA} - 3 \cos \Theta_D \cos \Theta_A) \quad (27)$$

with the donor-acceptor separation  $r$  and the orientation factor  $\kappa = \cos \Theta_{DA} - 3 \cos \Theta_D \cos \Theta_A$ . Herein,  $\Theta_{DA}$  is the angle between the emission dipole of the donor and the absorption dipole of the acceptor, and  $\Theta_D$  and  $\Theta_A$  the angles between the respective dipole and the connection vector between donor and acceptor.

From Equation 27 and Fermi's golden rule in Equation 14 the rate for such dipole-dipole transition can be derived:

$$k_{dd} = \frac{1}{\tau_D} \left( \frac{d_0}{d} \right) \quad (28)$$

Here  $\tau_D$  is the excited state lifetime of the donor and

$$d_0 = \frac{9000 \ln(10) \kappa^2}{128 \pi^5 N_A n^4} \int E_D(\lambda) \epsilon_A(\lambda) \lambda^4 d\lambda \quad (29)$$

with Avogadro's constant  $N_A$ , the refractive index  $n$ , and the overlap spectrum

$$J = \int E_D(\lambda) \epsilon_A(\lambda) \lambda^4 d\lambda. \quad (30)$$

In the overlap spectrum,  $E_D$  is the emission spectrum of the donor normalized to an area of 1 and  $\epsilon_A$  the molar extinction coefficient of the acceptor molecules. Förster first derived the rate for the dipole-dipole transition [90] which is why the mechanism is referred to as Förster energy transfer (FET) and the characteristic distance  $d_0$  is called the Förster distance.

Besides dipole-dipole interactions, electron exchange plays a significant role in energy transfer mechanisms and is discussed next.

#### 4.2.2.2 Exchange Energy Transfer

Electrostatic interaction between the charge clouds occurs via overlap of the electron clouds and thus requires physical contact between the donor and acceptor. If there is no direct overlap, interaction may occur via intervening ions [81]. The second term in Equation 25 for two electrons separated by a distance  $r$  in the D-A pair can be expressed as

$$U_{ex} = \langle \Phi_{D^*}(1) \Phi_A(2) | \frac{e^2}{r} | \Phi_D(2) \Phi_{A^*}(1) \rangle \quad (31)$$

with  $\Phi_A$  and  $\Phi_D$  representing contributions of the spatial wavefunction to the total wavefunctions  $\psi_A$  and  $\psi_D$ .

Using this expression and Fermi's golden rule, one can derive an expression for the transition rate as has been done first by *Dexter* which is why the mechanism is also referred to as Dexter energy transfer (DET). The expression later derived by *Inokuti* and *Hirayama* reads

$$k_{ex} = \frac{1}{\tau_D} \exp \left[ \gamma \left( 1 - \frac{r}{r_0} \right) \right] \quad (32)$$

with the characteristic radius  $r_0$  called Dexter radius and

$$\gamma = \frac{2r_0}{L} \quad (33)$$

where  $L$  is called the effective average Bohr radius. The transition rate also depends on the overlap spectrum  $J$  of the involved transitions which can be expressed as

$$\frac{e^\gamma}{\tau_D} = \frac{2\pi}{\hbar} K^2 J \quad (34)$$

where  $K$  is a constant with the dimension of energy.

In contrast to exchange interactions which occur within small distances, dipole-dipole interactions occur over a comparatively long distance of up to 10 nm [95]. This is why mechanisms based on Dexter transfers are referred to as energy diffusion while Förster transfer based mechanisms are referred to as energy hopping. Both, Förster and Dexter transfer drive interaction mechanisms. As can be seen from Equations [Equation 29](#) and [Equation 34](#), the transition rates of these particular processes differ only in their overlap spectrum. This will further be of particular interest for the numerical determination of the different characteristic length scales in [Chapter 10](#).

### 4.3 PARTICULARITIES ON THE NANOSCALE

Optical properties of nanocomposites like nanocrystal dispersions can differ significantly from bulk materials. Besides the mechanisms discussed above, lanthanide nanocrystals experience further effects which are specifically relevant at the nanoscale. These effects base on the influence of the medium which surrounds the nanocrystals. On one hand, its electrical field affects the local field within the nanocrystal and thus the radiative lifetime. On the other hand, the excitation energy can be transferred to the surrounding medium via multiphonon quenching leading to a drastic decrease of the radiative lifetime. These mechanisms will be introduced in the following.

#### 4.3.1 Local Field Effects on Nanocrystals

The local field affects the electrical dipole moment, and it can be shown that this has a direct influence on the Einstein A coefficient (see e.g. [3]) which is inversely proportional to the radiative lifetime. The Einstein coefficient can be expressed through Fermi's golden rule as in Equation 14. In this, the interaction energy  $V_{12}$  scales as [96]

$$V_{12} \propto \frac{L}{\sqrt{n_{\text{eff}}}}, \quad (35)$$

where  $L$  is called the local field correction factor and  $n_{\text{eff}}$  the effective refractive index which can be obtained employing effective medium theory (see below). The local field correction factor corresponds to the ratio of the microscopic field acting on one individual emitter to the macroscopic average field in the medium. It can be found by quantizing Maxwell's equations that the density of states of radiation  $\rho$  is proportional to the effective refractive index [97]:

$$\rho(\omega_0) \propto n_{\text{eff}}^2. \quad (36)$$

From Equations Equation 14, Equation 35, and Equation 36 follows that the radiative emission rate  $A_{\text{LFE}}$  in the medium is related to the bulk crystal emission rate  $A$  as

$$A_{\text{LFE}} = n_{\text{eff}} L^2 A. \quad (37)$$

The effective refractive index can be obtained from Maxwell and Garnett's effective medium theory via

$$\frac{n_{\text{eff}}^2 - n_{\text{med}}^2}{n_{\text{eff}}^2 + 2n_{\text{med}}^2} = f_{\text{NC}} \frac{n_{\text{NC}}^2 - n_{\text{med}}^2}{n_{\text{NC}}^2 + 2n_{\text{med}}^2} \quad (38)$$

when the nanocrystal volume fraction  $f_{\text{NC}}$  within the sample is comparatively low [96, 98]. Here,  $n_{\text{med}}$  is the refractive index of the surrounding medium, and  $n_{\text{NC}}$  is the refractive index of the nanocrystal. Both refractive indices are close to each other when organic solvents or optical grade glasses are the surrounding medium for fluoride based nanocrystals like  $\text{LiYF}_4:\text{Pr}^{3+}$ . This results in an effective refractive index that differs only slightly from refractive index of the crystal system which is advantageous in two ways: First, local field effects have only small impact on the lifetime. Second, scattering plays only a minor role.

Theoretical models predict expressions for the local field correction factor  $L$  and are able to describe the experimental results. The two most prominent models are called the virtual-cavity model and the

real-cavity model. Dolgaleva and co-workers investigated Nd:YAG nanocrystals in different organic solvents and found out that the virtual-cavity model explains their experiments the best [96] which, thus, was employed here as well.

In this model, the dielectric medium can be considered to be a cubic lattice of point dipoles. The space around a chosen emitter can be divided into two regions. The first region consists of nearby dipoles treated as discrete particles and the second region consists of more distant dipoles treated in a continuum approximation. A virtual sphere of radius  $R$  marks the boundary between both regions. The radius is chosen such that  $a \ll R \ll \lambda$ , where  $a$  is the lattice constant and  $\lambda$  the wavelength of light. Using this approach, one obtains

$$L = \frac{n_{\text{diel}}^2 + 2}{3} \quad (39)$$

for the local field correction factor [99, 100] with the refractive index of the dielectric medium  $n_{\text{diel}}$ .

From these expressions it can be predicted that local field effects in organic solvents like toluene, as used here, change the excited state lifetime of  $\text{LiYF}_4:\text{Pr}^{3+}$  nanocrystals about  $1 \mu\text{s}$  compared to bulk crystals. Dolgaleva and co-workers observed a fast decay component in their decay measurement which they elaborate may come from ions sitting on the surface of the nanocrystals [96]. Indeed, multiphonon quenching can play a significant role for the spontaneous emission decay in nanocrystals.

#### 4.3.2 Förster Transfer based Multi-Phonon Quenching

Energy loss mechanisms in nanocrystals are broadly discussed in the upconversion nanocrystal scientific community [55, 101–103]. Besides the mechanisms already discussed above, Förster transfer can also occur from an excited ion to vibrational modes in the surrounding medium [55, 103, 104]. To obtain an expression for the calculation of Förster transfer to vibrational modes, Sveshnikova and co-workers chose a similar ansatz as for the calculation of the dipole-dipole interaction [105]. Again, a set of donor  $D$  and acceptor  $A$  is used but the acceptor is chosen to be a vibrational mode within the surrounding medium. Following this, one obtains the same expression as in Equation 28 [106] with the Förster distance

$$d_0 = \frac{9000 \ln(10) \kappa^2}{128 \pi^5 N_A n^4} J \quad (40)$$

which only differs from Equation 29 by its overlap spectrum

$$J = \int E_D(\lambda) \epsilon_A(\lambda) \lambda^4 d\lambda. \quad (41)$$



In Equation 29,  $\epsilon$  refers to the molar extinction coefficient of an electronic acceptor such as a praseodymium ion. The above expression for the overlap integral, however, refers to the molar extinction coefficient of a vibrational acceptor such as organic molecules or glasses [105].

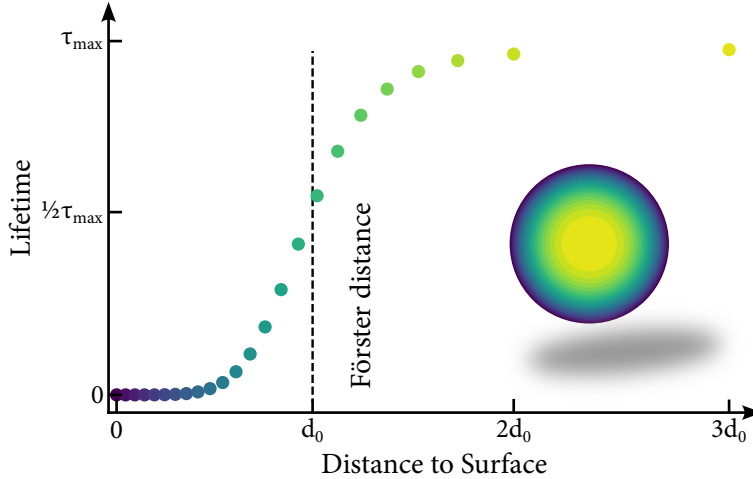


Figure 13: The influence of multiphonon quenching on the excited state lifetime can be illustrated using an onion shell model. The different shells are highlighted with different colors. Increasing the distance between the lanthanide ions and the vibrational energy acceptor will decrease the quenching efficiency which can be achieved with an undoped shell around the nanocrystal.

Interaction between praseodymium ions and the vibrational acceptors in the surrounding medium is the main reason for multiphonon quenching which reduces the excited state lifetime significantly.

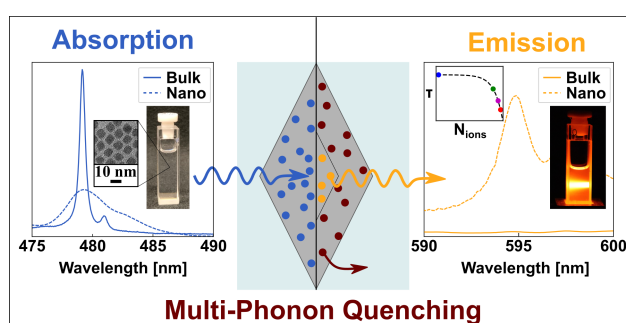
Phenomenological insight can be obtained from a simple onion shell model. The model assumes a spherical nanocrystal geometry and the active ions to be distributed equally in the volume. The particle is divided in onion shells of equal volume to provide for an equal amount of active ions per onion shell. The excited state lifetime of a bulk  $\text{LiYF}_4:\text{Pr}^{3+}$  crystal is put into Equation 28 as lifetime of the donor  $\tau_D$  to calculate the lifetime of each onion shell. The average over all onion shells yields the total decay and from its time weighted average the excited lifetime of such nanocrystal is obtained. In Figure 13, the lifetime is shown dependent on the distance of every onion shell to the surface of such nanocrystal. This illustrates a prominent strategy to suppress Förster transfer driven multiphonon quenching: Adding an undoped shell around the nanocrystal will act as spacer between donor ions and vibrational acceptor and thus improve the excited state lifetime and the quantum yield of the nanocrystals [34, 107–113].



## Part II

### SPECTROSCOPY

In this part, a comprehensive spectroscopic analysis of  $\text{LiYF}_4:\text{Pr}^{3+}$  nanocrystals was performed. The spectroscopic



Graphical summary of the presented results.

behavior of the nanocrystals is compared to macroscopic bulk crystals, and strong multiphonon quenching was observed, which results in reduced quantum yields. This effect is indeed disadvantageous for visible emission from these nanocrystals. At the same time, the multiphonon quenching efficiently populates the subjacent energy level, which yields unexpected yet intense emission at 595 nm with excited state lifetimes comparable to bulk crystals. Especially the excited state lifetime and quantum yield are used in Part III of this work.



## EXPERIMENTAL SETUPS

## Contents

5.1	Absorption . . . . .	41
5.2	Excited State Lifetimes . . . . .	42
5.3	Emission . . . . .	43
5.4	Quantum Yield . . . . .	43

In the present chapter, the experimental setups used to experimentally characterize the  $\text{LiYF}_4:\text{Pr}^{3+}$  nanocrystals are presented. The results of these characterizations follow in [Chapter 7](#) and [Chapter 8](#). For the experimental investigation, the nanocrystal dispersions were filled into cuvettes with a length of 1 cm. These cuvettes were used to measure the absorption, spontaneous emission, and the dynamics (lifetime and quantum yield).

## 5.1 ABSORPTION

Transmission spectra of the samples were measured using a UV-VIS-NIR photospectrometer (Perkin Elmer Lambda 1050). This photospectrometer can be used for measurements from 175 nm to 3300 nm. The setup is sketched in [Figure 14](#). The photospectrometer consists

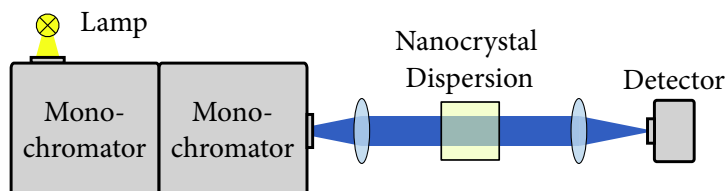


Figure 14: Schematic of the setup used for the measurement of the absorption spectra. The second measuring channel was not drawn in for the sake of simplicity.

of a tungsten-halogen and a deuterium lamp. The wavelength of this light can be tuned with a holographic grating monochromator which contains two gratings with 1440 lines/mm blazed at 240 nm and 350 lines/mm blazed at 1100 nm, respectively, in Littrow configuration. Three detectors are available: the entire UV/VIS wavelength range can be measured from 175 nm to 860 nm with a photomultiplier tube, and the IR wavelength range can be measured using an InGaAs detector for 860-2500 nm or an PbS detector for 2500-3300 nm.

In the present case, the spectral resolution was set to 0.05 nm for measurements of the nanocrystal dispersions, and the integration

time of the detector was set to 0.5 s. Spectra were recorded in a range of 400-500 nm as well as 560-610 nm to account for the  $^3P_0$  and  $^1D_2$  transitions, respectively. The spectral range between these two sections was not measured to reduce the acquisition time.

First, a baseline was recorded with a cuvette containing just the organic solvent (Toluene) and then, the dispersions were measured. This measurement was corrected by the baseline to obtain raw transmission spectra. Besides the expected peaks that can be attributed to the Praseodymium ions in the nanocrystals, the transmission shows a sigmoid-like underground. This behavior is due to the oleic acid ligands which are used to stabilize the nanocrystals in the solvent, c.f. [Chapter 6](#).

## 5.2 EXCITED STATE LIFETIMES

The lifetime of the excited state was determined through temporal measurement of the spontaneous emission decay. The setup is depicted in [Figure 15](#). A pulsed optical parametric oscillator (OPO, Spectra Physics ULD-240) operating at a repetition rate of 10 Hz delivered 4 ns short pulses which served as excitation source. The tuning range spans from 405 nm to 2.75  $\mu\text{m}$  and maximum pulse energies of 70 mJ are reached at around 500 nm. The OPO was tuned to 479 nm to excite the praseodymium in the nanocrystals from the ground level  $^3H_4$  to the  $^3P_0$  level. The excitation pulses were focussed into the cuvette using a lens with 500 mm focal length. A parabolic mirror of 2" diameter was used to collect emission from the nanocrystals. The collected light was focussed to a monochromator using high numerical aperture (NA) lenses. The monochromator was tuned to the emission wavelength of interest, here: 639 nm and 595 nm for emission originating from the  $^3P_0$  and  $^1D_2$  level, respectively. A 100 MHz Si-photodiode with integrated gain module (Femto, OE-300-SI-30) has been used to detect the emission dynamics. The excitation pulses cannot be resolved with this setup since the response time of the photodiode limits the resolution to 10 ns. This, however, did not limit the analysis of the lifetimes since this analysis was done in a fitting procedure as described in [Chapter 8](#). The photodiode was connected to a 500 MHz oscilloscope (Tektronix, 620B) with a sampling rate of 2.5 GSa/s terminated by a 50  $\Omega$  resistor. This oscilloscope was connected to a computer for data collection. An average of 100 measurements was sufficient to reduce noise and the influence of energy fluctuations of the OPO pulses to a level that enabled successful fitting of the lifetimes. Despite the monochromator acting as a filtering element to the emitted light a fast component was detected in the temporal signal which corresponded to residual excitation light. Using optical long pass filters and housing of the beam paths the residual excitation light was strongly reduced, however, not fully removed.

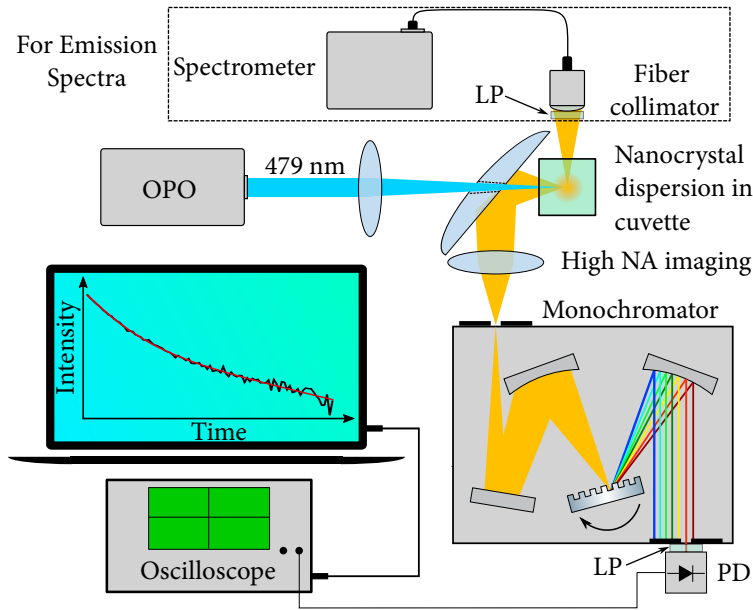


Figure 15: Schematic of the setup used for the measurement of the spontaneous emission decay and spectra.

### 5.3 EMISSION

Spontaneous emission spectra were measured with the setup presented above. For such measurement a fiber coupled USB-spectrometer with a spectral resolution of 0.42 nm was added to the setup in Figure 15. A commercial optical multimode fiber with a core diameter of 1.5 mm and an numerical aperture of 0.5 was used to couple as much light as possible to the spectrometer. At the front, this fiber was connected to a commercial fiber collimator to collect the spontaneous emission from the samples. An optical longpass filter with a cut-on wavelength at 500 nm served to filter residual pump light. These optics were positioned orthogonal to the pump beam in front of the cuvette.

### 5.4 QUANTUM YIELD

The quantum yield is defined as the ratio of emitted and absorbed photons. For this thesis, it was measured with a commercial photoluminescence spectrometer (Edinburgh Instruments FLS 1000) sketched in Figure 16.

In this setup, light from a 450 W ozone-free xenon arc lamp is spectrally filtered through a Czerny-Turner-type double monochromator. Each monochromator has a focal length of 325 mm. In the experiments, the monochromators were set to 444 nm and 479 nm with a spectral width of 10 nm. The emission is recorded perpendicular respective to the excitation beam path. The emission is spectrally re-

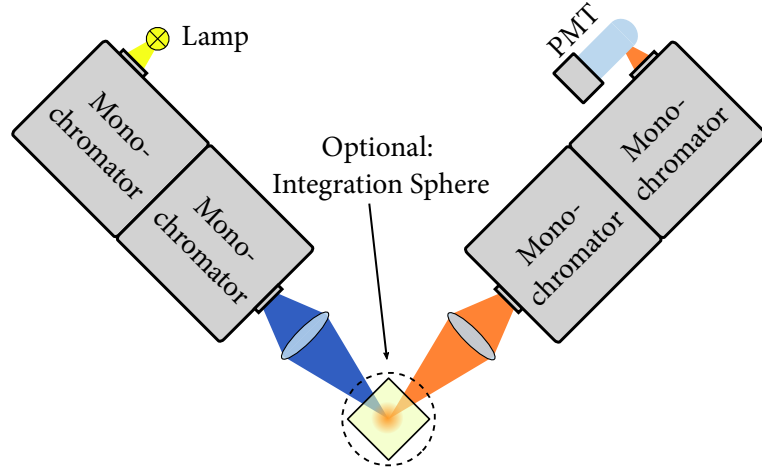


Figure 16: Schematic of the setup used for emission spectra. With an integration sphere, this setup can also be used to determine the quantum yield of a certain sample.

solved with a second Czerny-Turner type double monochromator. Again, each monochromator has a focal length of 325 mm but here, the spectral resolution was set to 1 nm. The signal was recorded with a photomultiplier tube covering a spectral range of 200-900 nm and a response widths of 600 ps.

The quantum yield measurement takes place in an integration sphere to collect the photons in all spatial directions. First, excitation and emission spectra  $S_0^{exc}(\lambda)$  and  $S_0^{em}(\lambda)$  of toluene filled cuvettes were recorded in the respective spectral range. Next, both spectra  $S^{exc}(\lambda)$  and  $S^{em}(\lambda)$  were measured for the nanocrystal dispersions. The quantum yield QY was obtained from these spectra via

$$QY(\lambda_{em}, \lambda_{exc}) = \frac{\int_{em} S^{em}(\lambda_{em}) d\lambda - \int_{em} S_0^{em}(\lambda_{em}) d\lambda}{\int_{exc} S^{exc}(\lambda_{exc}) d\lambda - \int_{exc} S_0^{exc}(\lambda_{exc}) d\lambda}. \quad (42)$$

The measurement error of this setup is 5 percentage-points which may seem comparatively high. However, specialty quantum yield measurement setups also only achieve errors of 2 percentage-points [114]. As will turn out in Part III of this thesis, this measurement error was sufficient for the quantum yield to act as further control parameter in addition to the excited state lifetimes in the simulations.



## THE ORGANIC LIGAND: OLEIC ACID

As introduced in [Chapter 2](#), the organic ligand of the nanocrystals is oleic acid which, depending on the purity, might contain other fatty acids. These acids can oxidize or form more complex structures in presence of oxygen at high temperatures. Such processes lead to a yellowish or brownish coloration of the reaction mixture that is accompanied by changes in the spectroscopic behavior of the samples. This can be highlighted in a simple experiment where the absorption and emission spectra of slightly and strongly colored oleic acid was measured. The slightly and strongly colored samples were obtained by leaving one sample of oleic acid for several hours at room temperature and heating a second sample to 300 °C for four hours, respectively. The absorption and emission spectra are shown in [Figure 17](#). The emission spectra were obtained by irradiating the samples at a wavelength of 479 nm which is the same wavelength that was used to excite the  $^3P_0$  level in  $\text{LiYF}_4:\text{Pr}^{3+}$ .

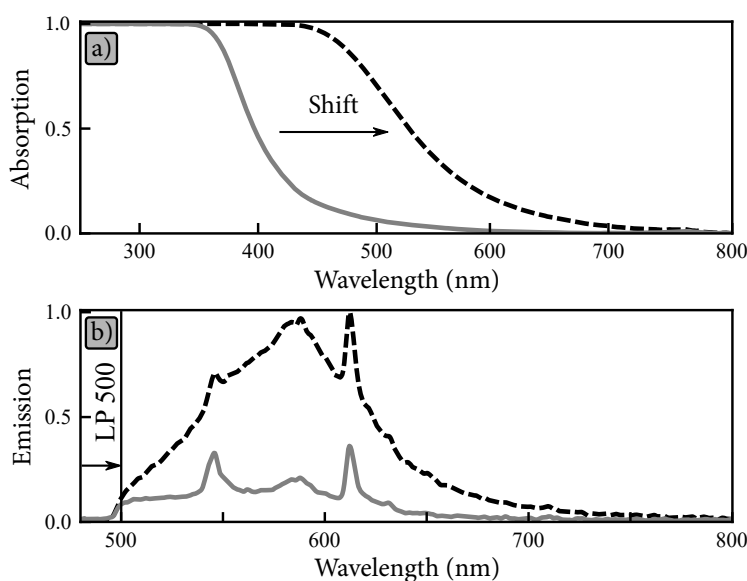


Figure 17: a) Absorption spectra of oleic acid (OA) shifts toward red wavelengths with oxidation (black dashed curve). b) Emission spectrum of OA intensifies with oxidation, the excitation was removed from the signal with a longpass filter.

The colored samples exhibit strong absorption at short wavelengths that redshifts for higher oxidation levels, see [Figure 17a](#). At 479 nm, the absorption increases from 9% for the low oxidized sample to 85% for the highly oxidized sample explaining the strong increase in emission. This means that a significant part of incident light will be

absorbed from the organic ligand when using nanocrystal dispersions with highly oxidized oleic acid.

When exciting colored oleic acid with mJ-level ns-pulses, respective emission lines appear in the visible spectrum and intensify for stronger colorization, see Figure 17b. In improperly synthesized  $\text{LiYF}_4:\text{Pr}^{3+}$  nanocrystal dispersions, the characteristic absorption and emission lines of the  $\text{Pr}^{3+}$  ions and colorized oleic acid are superimposed, thus distorting the optical properties of the  $\text{Pr}^{3+}$  emission. Therefore, it is evident that oxidation of the oleic acid ligands also falsely increases the measured quantum yield.

The excited state lifetime of oleic acid is discussed in Chapter 8.

In general, oxidized oleic acid lowers the optical quality of the nanocrystal dispersions. Figure 18 shows the emission spectra of  $\text{LiYF}_4:\text{Pr}^{3+}$  nanocrystal dispersions with low, acceptable, and high oxidation state. Emission from the nanocrystals and the oleic acid are not distinguishable from spectra with high oxidation state. Therefore, cross sections cannot be determined properly and quantum yields might be strongly distorted.

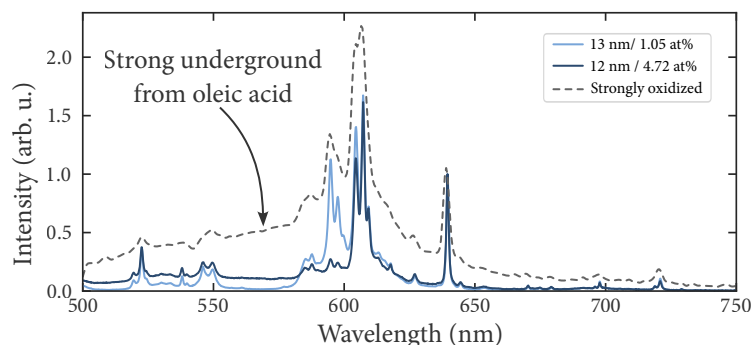


Figure 18: Influence of the fatty acids' oxidation state on the emission spectra of  $\text{LiYF}_4:\text{Pr}^{3+}$  nanocrystals, normalized to the peak at 639.5 nm. The gray line shows a sample with very high oxidation that was considered unusable. Samples of the size series show somewhat higher background than the samples of the concentration series but are considered usable.

Fortunately, the evaluation of the optical quality of a nanocrystal dispersion is comparatively simple as comparison of at least 30 different samples has shown: If no colorization is visible the sample is likely to show excellent spectroscopic behavior. Nevertheless, even for high-quality samples the oleic acid has a relevant influence on the spectroscopic properties of the samples. This requires careful handling of the spectroscopic results. Regarding absorption spectroscopy, even high-quality samples show a sigmoid-like underground resulting from the oleic acid absorption, c.f. Figure 17, that strongly reduces the transmission in the UV and blue spectrum. This calls for post-measurement treatment of absorption spectra as discussed in the next chapter. Regarding emission spectroscopy, even marginal ox-

idation of the oleic acid falsely contributes to the measured quantum yield which is important to consider for samples with low quantum yields.



---

**Contents**


---

7.1	Absorption Cross Sections . . . . .	49
7.2	Fitting the Absorption Cross Section . . . . .	50
7.2.1	Fitting Procedure . . . . .	50
7.2.2	Discussion of the Fitting Results . . . . .	52
7.3	Discussion . . . . .	53

---

In this chapter, the results of the absorption spectroscopy are described and discussed. A new fitting procedure was applied to quantify the broadening and shift of the absorption spectra compared to the bulk spectra. This procedure was developed by Dr. Michael Steinke and has been published previously in reference [54].

### 7.1 ABSORPTION CROSS SECTIONS

The raw transmission spectra show discrete peaks which can be assigned to the well-known absorption lines of Praseodymium ions. Furthermore, a broad sigmoid-like absorption can be observed. This absorption can be assigned to the oleic acid ligands around the nanocrystals, c.f. [Chapter 6](#).

The transmission spectrum of the oleic acid was subtracted from the transmission  $T$ . Due to the very small particle size, which is around a factor of 50 smaller than the wavelength, scattering is assumed to be negligible. Lambert-Beer's law

$$I(\lambda) = I_0 \cdot \exp(-\alpha(\lambda)l) \quad (43)$$

was applied to the transmission data with the transmission  $T = I(\lambda, z)/I_0$  of the input signal  $I_0$ ,  $l$  being the length of the cuvette, and the absorption coefficient  $\alpha$ . The ion density  $N$  was calculated using the nanocrystal dimensions and doping concentrations determined in [Chapter 2](#) so that the absorption cross sections were obtained from

$$\sigma_{\text{abs}} = \frac{\alpha(\lambda)}{N}. \quad (44)$$

The resulting absorption cross sections for every sample investigated in this work are depicted in [Figure 19](#) and [Figure 20](#). The peaks of the cross sections differ by roughly 50% which can be attributed to

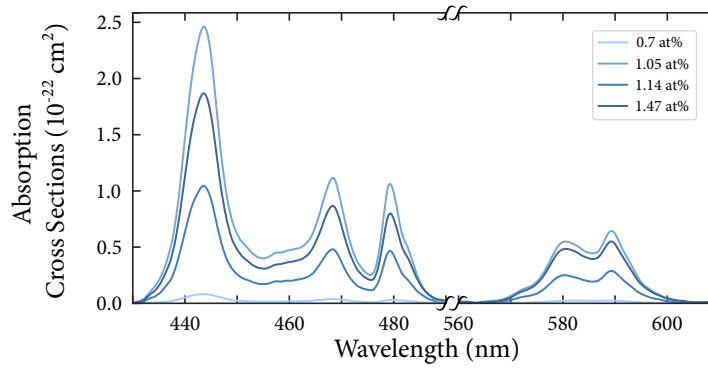


Figure 19: Absorption cross sections of the concentration series of  $\text{LiYF}_{44}:\text{Pr}^{3+}$  nanocrystals.

inaccuracies in the size distribution analysis as well as the EDX analysis. Typically, one would expect the same cross sections for doping concentrations as low as investigated in this work.

The peak absorption cross sections differs by three orders of magnitude with respect to the cross section of bulk crystals. While bulk crystals exhibit a peak absorption cross section of up to  $1.7 \cdot 10^{-19} \text{ cm}^2$  at 444 nm, the nanocrystals' is  $3.4 \cdot 10^{-22} \text{ cm}^2$ . At the same time, the spectral linewidths are strongly broadened and shifted compared to their bulk counterparts. Therefore, instead of comparing the peak values, the integrated cross sections should be compared, which only differ by a factor of 45. The absorption lines of bulk crystals are well described by Lorentzian profiles, see inset of [Figure 21](#), representing homogenous broadening mechanisms. In contrast, the corresponding transitions in nanocrystals deviate from this line shape. However, fitting each individual transition in both bulk and nanocrystal absorption and comparing them is not promising as such a fit is heavily overdetermined.

## 7.2 FITTING THE ABSORPTION CROSS SECTION

To quantify the deviations between nanocrystal and bulk absorption spectra, a novel fitting approach was employed that only requires a few fit parameters to easily determine line shape deviations and the nature of spectral broadening [54].

### 7.2.1 Fitting Procedure

The mechanism influencing the absorption of the nanocrystals can be both, homogenous and inhomogeneous. A combination of homogenous and inhomogeneous broadening mechanisms can be described

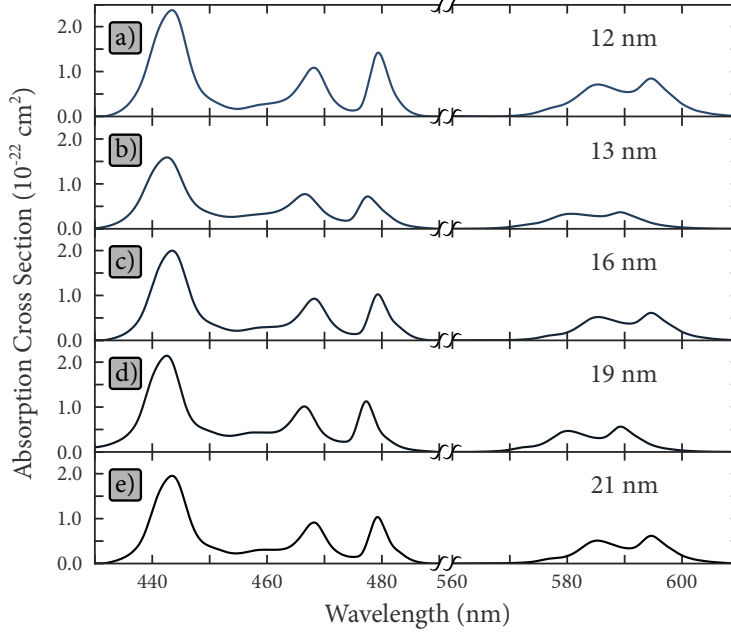


Figure 20: Absorption cross sections of the size series of  $\text{LiYF}_4:\text{Pr}^{3+}$  nanocrystals.

by a convolution of Lorentzian- and Gaussian-profile, respectively, represented by the so-called Voigt-profile

$$V(\lambda, A, \lambda_c, \sigma, \gamma) = \frac{A \cdot \Re[w(z)]}{\sigma \cdot \sqrt{2\pi}} \quad (45)$$

where  $\Re[w(z)]$  is the real part of

$$w(z) = \exp(-z^2) \cdot \text{erf}(-iz) \text{ with } z = \frac{\lambda - \lambda_c + i\gamma}{\sigma\sqrt{2}}, \quad (46)$$

and  $\text{erfc}(x)$  is the complementary error function. Furthermore,  $A$ ,  $\lambda_c$ ,  $\sigma$ , and  $2\gamma$  are the amplitude, central wavelength of the peak, standard

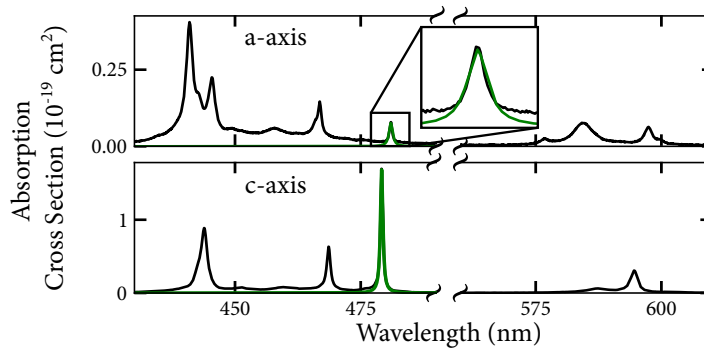


Figure 21: Absorption cross sections of the a- and c-axis of  $\text{LiYF}_4:0.65 \text{ at\% Pr}^{3+}$  bulk crystal and exemplary fit of a Lorentzian-profile to the peak corresponding to the  ${}^3\text{H}_4 \rightarrow {}^3\text{P}_0$  transition.

deviation of the Gaussian part, and the scale parameter, which specifies the full-width at half-maximum (FWHM) of the Lorentzian part, respectively.

It is assumed that there are two classes of ions [58]: (i) ions which are fully affected and (ii) ions that are not at all affected by the mechanism which leads to the spectral changes since fitting the broadening and shift of each transition individually would over-determine the fit. A global fitting approach was chosen and assuming that all energy levels are affected equally (convolutions are associative) it is sufficient to convolve a single Voigt-profile with a weighted sum of the bulk absorption spectra for both axes. The weight factor was also set as fit parameter. In the fitting procedure, one global spectral shift for both spectra is allowed. Furthermore, a non-broadened part is included in the fit function to account for the not-affected ions. Using a Voigt-profile accounts for both homogenous and inhomogeneous broadening mechanisms.

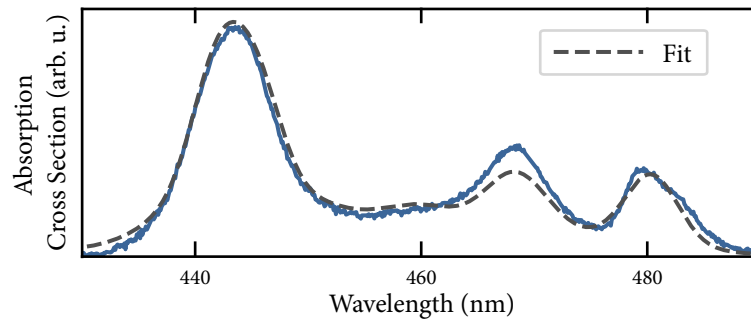


Figure 22: Absorption cross section and fit from bulk spectra of the 1.47% doped nanocrystals of 10 nm size.

Such fit was performed for all absorption spectra of the concentration series with comparable results. Therefore, the results are discussed exemplarily for the 1.47 at% doped sample, depicted in Figure 22. Besides this discussion, it can be seen from this figure that the assumptions made for this fitting procedure are not precisely correct as the peak at 468 nm is not well fitted. This indicates that the broadening mechanism does not affect all transition in the same way. From the energy level scheme in Figure 11, it can be seen that this absorption band results from a superposition of transitions from the ground state  $^3H_4$  to either the  $^1I_6$  or the  $^3P_1$  level. These two levels are thermally coupled and thus might not behave equally to the  $^3P_2$  and  $^3P_0$  level. Nevertheless, applying a global fitting routine is sufficient for a qualitative discussion regarding the broadening mechanisms.

### 7.2.2 Discussion of the Fitting Results

The fit resulted in a shift of the bulk spectra of around  $\Delta\lambda = 2$  nm, and the ratio of the bulk spectra was fitted to be around 0.3 to 0.4,



which means that around  $2/3$  of the absorption originates from the two a-axes and around  $1/3$  from the c-axis as expected due to the random orientation of the nanocrystals in the organic solvent. The Voigt profile contained mainly the Gaussian component with a full width at half maximum (FWHM) of 4-6 nm. A non-broadened component was allowed in the fit, too, which was, however, less than 2 % of the non-broadened spectrum.

The Gaussian nature of the broadening of the absorption spectra indicates an inhomogeneous broadening mechanism. From the observed spectral shift, it can be inferred that the field of the surrounding medium has a strong influence on the  $\text{Pr}^{3+}$  ions, which results in the inhomogeneous broadening. Assuming a nearly uniform distribution of  $\text{Pr}^{3+}$  ions, significantly more ions are located at the surface than within the nanocrystal's volume due to its high surface-to-volume ratio as already known from the literature [115, 116]. The ratio of the non-broadened component is indeed small (<2 %), but non-zero. Therefore, it can be deduced that only a small number of ions are not influenced by the field of the surrounding medium.

The fits of the absorption spectra of the size series were only possible with a significantly lower goodness of fit. The fitting program, among others, returns the result of Pearson's  $\chi^2$  test [117]. This value increased from  $\chi^2 < 0.2$  for the concentration series to  $\chi^2 < 3$  for the size series. In addition to the inaccuracies of the fitting procedure discussed in Section 7.2.1, the following reasons could be responsible for the problems with fitting the absorption spectra of the size series: At higher doping concentrations, the absorption spectra of bulk crystals might change making the available bulk absorption spectra of 0.65 at%-doped crystals inapplicable for 5 at%-doped nanocrystals. Furthermore, these nanocrystals might exhibit more defects due to the slightly different size of the  $\text{Pr}^{3+}$  ions that replace the  $\text{Y}^{3+}$  ions in the  $\text{LiYF}_4$  lattice. These defects might lead to changes in the local field and thus result in spectral shifts. Therefore, the fitting results for the size series were not considered in the present work.

Nevertheless, to allow for comparison of the absorption spectra of the different nanocrystal samples, the differences in peak wavelengths and widths at the different transitions are discussed in the next chapter.

### 7.3 DISCUSSION

The peak wavelengths of the important absorption transitions are depicted in Figure 23 for all samples together with the peak wavelength of the bulk crystal.

First, it is noticeable that for the  $^3\text{P}$  transitions, two samples of the size series deviate strongly from the trend of the other samples. The peak positions of these other samples deviate slightly from the bulk

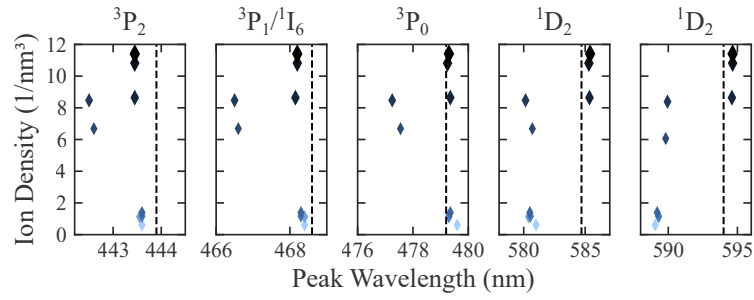


Figure 23: Absorption peak wavelengths of the concentration and size series separated by the final energy levels. The dashed line represents the peak wavelength of bulk crystals.

crystal but this deviation becomes smaller for longer wavelengths. This changes for the  $^1D$  transitions where the peak positions of the concentration series start to follow the trend of the two deviating samples in the size series. However, the peak position of the remaining samples of the size series stays close to the peak position of the bulk crystal although slightly red-shifted.

As already pointed out in the previous chapter, the local field effects do not affect all transitions in the same way. This explains the peak position shift for the different transitions that switches from a blue-shift to a red-shift. The strong shift of the two size series samples might originate from defects in the crystal lattice because these two samples were synthesized in another batch than the remaining three samples. The strong shift of peak position for the concentration series in the case of the  $^1D$  absorption might originate from the small size and weak doping concentration that result in a high percentage of ions being located at the nanocrystals surface and, thus, influenced by the local field.

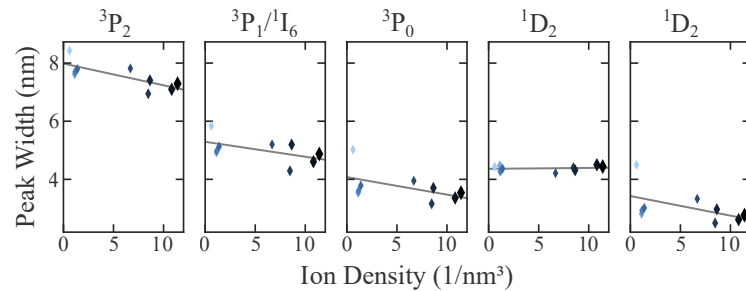


Figure 24: Spectral widths of the five absorption peaks for the concentration and size series, gray line indicates a linear fit.

The spectral widths of the respective peaks are depicted in [Figure 24](#) for all samples together with a linear fit. In case of the  $^3P$ -levels, the FWHM was considered. In case of the  $^1D$ -levels the full widths at 85% maximum was used as measure for the spectral width of the absorption peaks because both peaks are too close to distinguish them.

This seems to have influenced the results as the fit for the first peak of the  $^1D_2$  absorption slightly increases with the ion density while all the other fits show a negative slope.

From the fits it is evident that the absorption peaks become narrower with increasing ion density which is due to the nanocrystals getting larger. The local field of the surrounding medium has less influence on the  $Pr^{3+}$  ions at larger particle scales resulting in the narrowing of the spectra. To further exploit this effect in the future, an undoped shell around the nanocrystals may be considered since it increases the distance to the surrounding medium and thus prevents a distortion of the  $Pr^{3+}$  ions.



---

**Contents**

8.1	Spontaneous Emission Spectra . . . . .	57
8.2	Excited State Lifetime and Quantum Yield . . . . .	61
8.2.1	Analysis of the Excited State Lifetime . . . . .	61
8.2.2	Analysis of the Quantum Yield . . . . .	63
8.2.3	Discussion on the Decay Dynamics . . . . .	64
8.2.4	Estimation of Characteristic Lengths . . . . .	65

---

In this chapter, the results of the emission spectroscopy are described and discussed. This includes the spectra of spontaneous emission as well as the lifetimes and quantum yields of the nanocrystals. The experimental results on the excited state lifetimes and quantum yield play an important role as control parameters in the simulations, c.f. Part III of this thesis. Although, it was found to be sufficient to employ the measured  $^3P_0$  lifetimes for that the quantum yield was included as an important indicator of the nanocrystals' performance. Furthermore, the  $^1D_2$  lifetimes were considered during the setup of the numerical model.

In the experiments, the nanocrystals were irradiated either at 444 nm or 479 nm to excite the  $Pr^{3+}$  ions to the  $^3P_2$  or  $^3P_0$  level, respectively. When using 444 nm, the ions also transition to the  $^3P_0$  level due to fast thermal processes. Consequently, the experimental results for both of these excitation wavelengths did not differ significantly and thus only results for excitation at 479 nm are discussed in the following.

### 8.1 SPONTANEOUS EMISSION SPECTRA

The emission spectra exhibit a variety of peaks in the visible spectrum as expected for  $LiYF_4:Pr^{3+}$  and can be seen exemplarily in [Figure 18](#). In case of the samples investigated in this thesis, no or neglectable underground was observed, which points to a very low oxidation state of the oleic acid ligands and, thus, a high quality of the samples.

Emission cross sections were obtained applying the Füchtbauer-Ladenburg equation [118]

$$\sigma_{em} = \frac{1}{8\pi cn^2 \tau_{rad}} \cdot \frac{\lambda^5 I(\lambda)}{\int I(\lambda) \lambda d\lambda}. \quad (47)$$

Here,  $c$  is the speed of light,  $n$  the refractive index  $\tau$  the excited state lifetime, and  $I$  the intensity of the emission. The refractive index was

obtained from Maxwell-Garnets effective medium theory [96] and the excited state lifetime was obtained from the measurements described below. It is noteworthy, that the Füchtbauer-Ladenburg equation uses approximations that are not valid in many cases. For example, the equation works only for narrow spectra and when all lines of the spectrum are considered. If the lines spread over a substantial spectral range, the narrow line approximation is not fulfilled as in the present case. Therefore, the McCumber theory [119], which relates the absorption and emission cross sections to each other, is often used as a supplement to support the plausibility of the results with the Füchtbauer-Ladenburg equation. To apply the McCumber theory, however, low-temperature spectroscopic measurements are necessary. This type of spectroscopy is difficult to perform with solution-processed nanomaterials such as the present  $\text{LiYF}_4:\text{Pr}^{3+}$  nanocrystals because the solution freezes which changes the spectroscopic properties of the samples. Additionally, as a simple practical impediment, the respective measurement equipment was not accessible during the period this thesis has been created. Therefore, only the Füchtbauer-Ladenburg equation was applied, although it should be noted that the results may be subject to uncertainties since the respective approximations are not completely fulfilled. The resulting emission cross sections are depicted in Figure 25 and Figure 27.

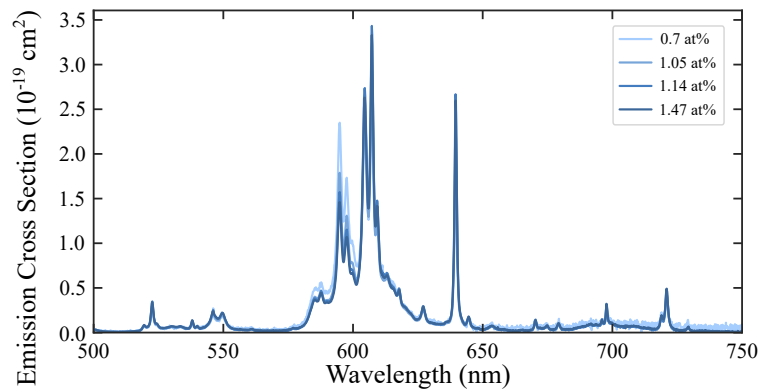


Figure 25: Emission cross sections of the concentration series of  $\text{LiYF}_4:\text{Pr}^{3+}$  nanocrystals.

All these cross sections of the nanocrystals only differ by a few percent which can be attributed to the different lifetimes (c.f. Section 8.2.1) since the cross sections are inversely proportional to the excited state lifetime, see Equation 47. As for the absorption cross sections, measurement inaccuracies have to be attributed to uncertainties of the relevant parameters such as lifetime or refractive index. Since the measured samples are nanoscaled counterparts of the bulk crystals a comparison of the emission cross sections promises conclusions on their respective differences. Therefore, emission cross sections of a

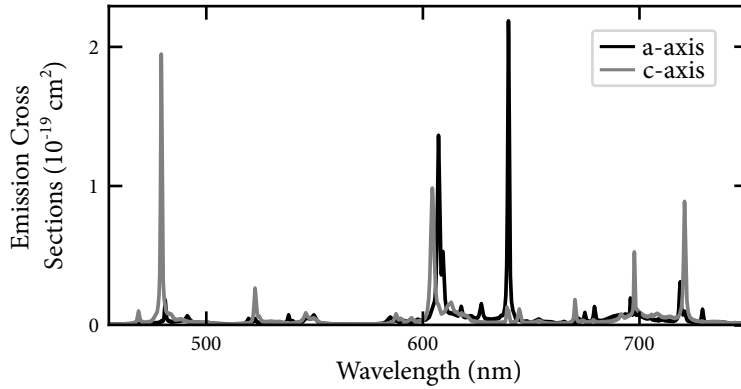


Figure 26: Emission cross sections of the c- and a- axis of a 0.65 at% doped bulk crystal.

bulk crystal being based on each of the different crystal axes (a and c) are depicted in [Figure 26](#).

Exemplarily, the nanocrystals of the concentration series with 1.47 at% doping concentration were compared in detail to the bulk crystals of 0.65 at% doping concentration. Bulk crystals exhibit peak emission cross sections of up to  $2.2 \cdot 10^{-19} \text{ cm}^2$  at an emission wavelength of 640 nm. A similar value of  $3.4 \cdot 10^{-19} \text{ cm}^2$  was obtained for the nanocrystals, albeit at another transition, at 607 nm. At 640 nm, however, the emission cross section of the nanocrystals is comparable to the bulk crystals.

The emission spectra show neither broadening nor spectral shifts, which is unexpected since a comparable behavior for emission and absorption spectra is predicted by McCumber theory [[119](#)]. However, at the nanoscale, mainly the ions in the center of the nanocrystal, the so-called bulk ions, contribute to the emission. In contrast, ions at the surface of the nanocrystals experience not only the crystalline environment but also the environment of the surrounding medium. This results, on the one hand, in spectral broadening of these surface ions through the local field of the surrounding medium as described in [Chapter 7](#). On the other hand, the surface ions interact with the surrounding medium which causes a transition from the excited  $^3P_0$  to the lower  $^1D_2$  level via multiphonon quenching. The unbroadened emission spectra indicate that multiphonon quenching has a greater characteristic length scale than the local field effect which causes the spectrally broadened absorption. Ions potentially contributing to a broadened emission spectrum lose their energy due to multiphonon quenching.

Further, a strong emission line was observed at 595 nm which corresponds to a transition from the  $^1D_2$  level and is evident in the cross sections of the nanocrystals. Although populating the  $^1D_2$  level via reabsorption of the  $^3P_0$  emission at 604 nm and 607 nm is in principle possible, this effect is estimated to be very weak due to the low

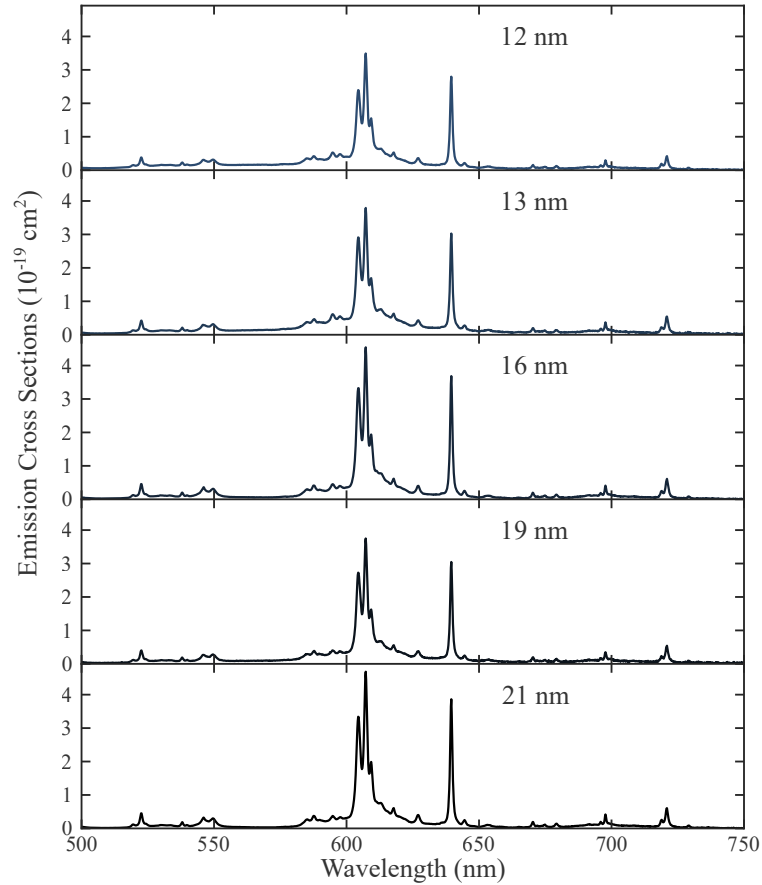


Figure 27: Emission cross sections of the size series of  $\text{LiYF}_4:\text{Pr}^{3+}$  nanocrystals.

respective absorption cross sections. It thus can be inferred that, multiphonon quenching leads to a significant population of the  $^1\text{D}_2$  level. The  $^1\text{D}_2$  level does not only emit at 595 nm but in a broad spectral range from 570 nm to 610 nm. Within this spectral range,  $^3\text{P}_0$  emission takes place as well, which means that the emission in this particular range is a superposition of  $^1\text{D}_2$  and  $^3\text{P}_0$  emissions. This superposition shifts the spectral position of the peak emission cross section from 607 nm in bulk crystals to 640 nm in the nanocrystals.

To better compare the  $^1\text{D}_2$  emission of the different samples, the relevant spectral range of the cross sections is depicted in Figure 28. To suffice the Füchtbauer-Ladenburg Equation 47 these emission cross sections were calculated with the actual lifetime of the  $^1\text{D}_2$  level instead of the lifetimes of the  $^3\text{P}_0$  level as in Figure 25 and Figure 27. The cross sections of the  $^1\text{D}_2$  level shown in Figure 28 therefore deviate from the ones included in Figure 25 and Figure 27.

The nanocrystals from the concentration series exhibit well-distinguishable and defined peaks while the cross sections of the size series are less defined and distinguishable. The 1.14 at% doped nanocrystals from the concentration series show the maximum of  $\approx 0.6 \cdot 10^{-19} \text{ cm}^2$



which can again be attributed to the lifetime of this sample, see [Figure 31b](#). The  $^1D_2$  cross sections of the size series decrease with the size of the nanocrystals because the percentage of ions that undergo quenching at the nanocrystal surface decreases.

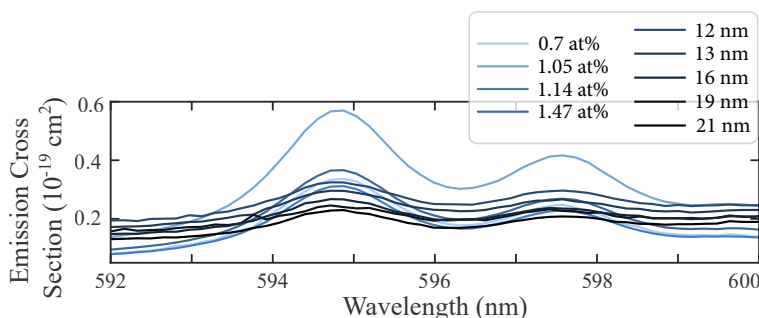


Figure 28: Cross sections of the emission originating from the  $^1D_2$  level. These cross sections differ from those depicted in [Figure 25](#) and [Figure 27](#) because, here, they were calculated with the measured lifetimes of the  $^1D_2$  level.

## 8.2 EXCITED STATE LIFETIME AND QUANTUM YIELD

Here, the experimental results of the excited state lifetime and quantum yield measurement are presented. They were employed as important control parameters in the simulations presented in Part III of this thesis. The results are jointly discussed since both measurements deliver similar evidence for the decay dynamics.

### 8.2.1 Analysis of the Excited State Lifetime

The measured decay traces result from a superposition of three different signals. The first one arises from the residual pump light, which could not be properly filtered from the optical signal and has no physical meaning (c.f. [Chapter 5](#)). The second contribution is the emission of the nanocrystals. This signal is superimposed with the third signal which is the emission from the organic ligands. Both of these signals are expected to have time constants about three orders of magnitude higher than the signal of the pump signal.

The original trace was corrected by the noise at the beginning and the end of the data. Then, a region of interest (ROI) was selected as shown in [Figure 29](#) to cut out insignificant data such as parts of the baseline without signal and especially the residual pump signal. The ROI is set by cutting the decay signal between the time stamps  $t_1$  and  $t_2$ . The initial time stamp  $t_1$  is used to cut the pump signal while the final time stamp  $t_2$  marks the point where the signal approaches the baseline noise. Furthermore, a moving average filter to smoothen the data was applied to reduce the signal noise. To extract the time

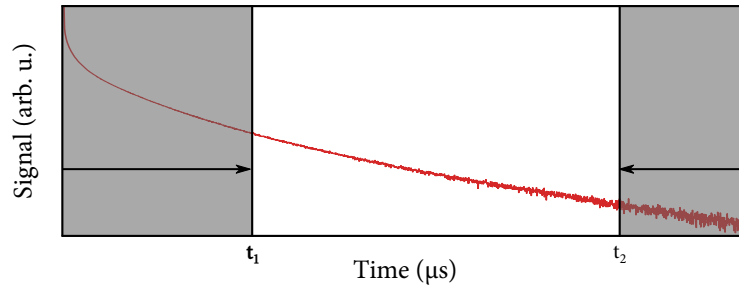


Figure 29: Schematic of the cutting of the region-of-interest.

constants of the decay from the samples a bi-exponential function of the form

$$y(t) = y_0 + ae^{-t/\tau_1} + be^{-t/\tau_2} \quad (48)$$

was fitted to the data in the ROI. One of the exponential functions represents the decay of the organic ligands emission while the other one represents the decay of the spontaneous emission originating from the nanocrystals. Preliminary investigations on oleic acid showed that the time constant of this decay is in the order of some microseconds. From bulk crystals it is known that the excited state lifetime of the nanocrystals may range in the order of some tens of microseconds. Therefore, the higher time constants can be allocated to the response of the nanocrystals.

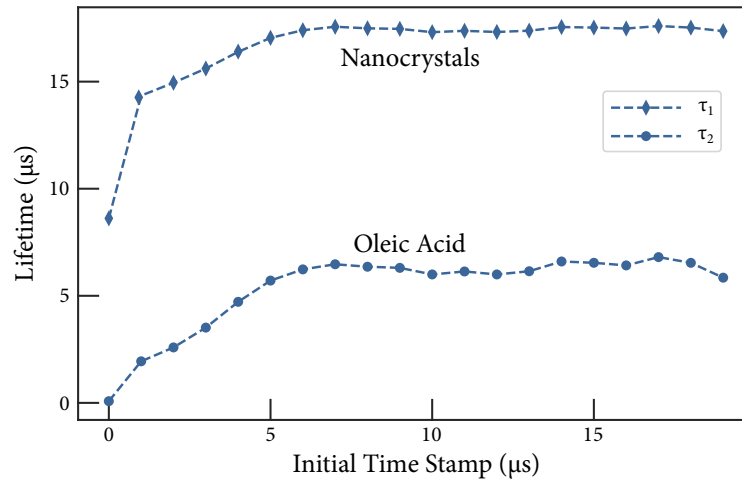


Figure 30: Dependence of the fit result on the initial time stamp, e.g., the  $^3P_0$  excited state lifetime for the 1.47 at% doped  $\text{LiYF}_4:\text{Pr}^{3+}$  nanocrystals.

To ensure the independence of the obtained time constants from the choice of fitting parameters, an extensive analysis of the influence of the initial time stamp  $t_1$  was performed in a first step. Bi-exponential fits were applied for a varying length of the initial time stamp. As an example, the result for the  $^3P_0$  lifetime of the 10 nm sized sample

with 1.47 at% doping concentration is given in Figure 30. The complete results for the  $^3P_0$  and  $^1D_2$  lifetimes are depicted in Figure 56 to Figure 59, respectively, in the Appendix. Due to the presence of the residual pump light in the decay signal it is expected that the obtained time constant strongly depends on the choice of  $t_1$  within the first microseconds. This is clearly the case for all samples. After that, the fitted lifetimes stay constant with increasing  $t_1$ . A comprehensive investigation on the second time stamp  $t_2$  was not needed as this time stamp was readily determinable from the noise level of the raw data. The lifetimes were obtained by calculating the arithmetic mean of the fitted lifetimes from  $5 \mu\text{s}$  to the end of the curves in Figure 56 to Figure 59, respectively. The lifetimes are summarized in Figure 31.

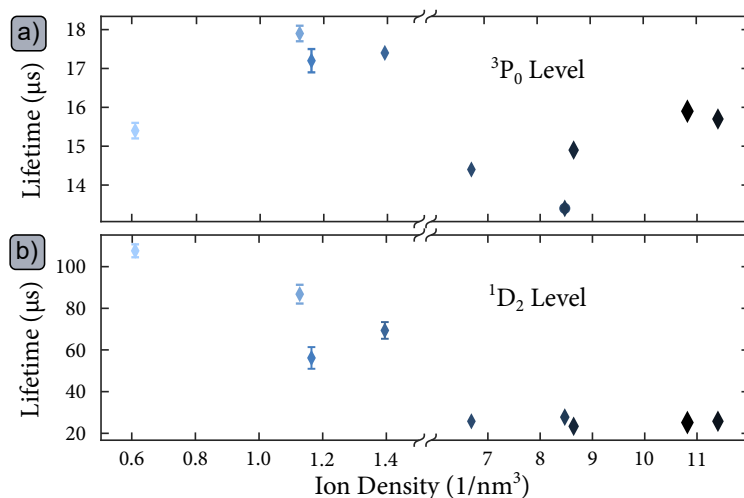


Figure 31: The lifetimes of a) the upper energy level  $^3P_0$  and b) the sub-adjacent  $^1D_2$  level. Note that the lifetime errors for the size series are considerably small and, thus, not visible in the graph.

### 8.2.2 Analysis of the Quantum Yield

The quantum yield was obtained according to Equation 42: The absorption and emission spectra of the sample and the reference were integrated, and the reference value was subtracted from the sample value. Finally, the quantum yield was obtained from the ratio of these values. For the quantum yield of the size series, a broad underground in the emission spectra of the nanocrystals was observed during the measurement. This underground might originate from oleic acid content, see Chapter 6. This underground could not be readily removed from the measurement. Therefore, the real experimental quantum yield has to be estimated to be at least 1% lower than the values depicted in Figure 32.

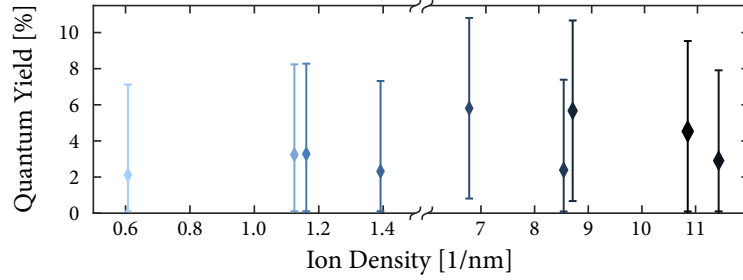


Figure 32: The quantum yields of all samples.

### 8.2.3 Discussion on the Decay Dynamics

The measured excited state lifetimes of the  $^3P_0$  level range between  $13 \mu\text{s}$  and  $18 \mu\text{s}$  as evident from Figure 31a. Richter and co-workers reported a lifetime of  $35.7 \mu\text{s}$  for bulk crystal doped with 0.65 at% [8]. In comparison to that, the 0.7% doped nanocrystals show an experimentally determined quantum yield of 3.2% and a lifetime of  $15.2 \pm 0.2 \mu\text{s}$ , which is about 40% of the excited state lifetime in bulk crystals, c.f. Figure 31. From that, one would expect either a somewhat higher quantum yield or a lower excited state lifetime, as high lifetimes are associated with well suppressed nonradiative transitions resulting in high quantum yields. In case of the nanocrystals, however, the strong multiphonon quenching of the surface ions increases the nonradiative rates. A nonradiative-to-radiative-rates ratio can be obtained from the quantum yield  $\eta$ . The nonradiative rate is represented by  $1 - \eta$ . Thus, the ratio can be estimated via  $(1 - \eta)/\eta$ . From that, it can be estimated that the nonradiative rates are around 20–50 times higher than the radiative rates. The contribution of the surface ions to the spontaneous emission from the  $^3P_0$  level is thus suppressed so that ions in the center reveal emission properties comparable to bulk crystals. The measured excited state lifetimes of the  $^1D_2$  level populated via multiphonon quenching are surprisingly high. For the 0.7% and 1.14% doped nanocrystals the lifetimes of  $108 \mu\text{s}$  and  $87 \mu\text{s}$  are well comparable to bulk lifetimes from that level which are  $101 \mu\text{s}$  and  $66 \mu\text{s}$ , respectively [71].

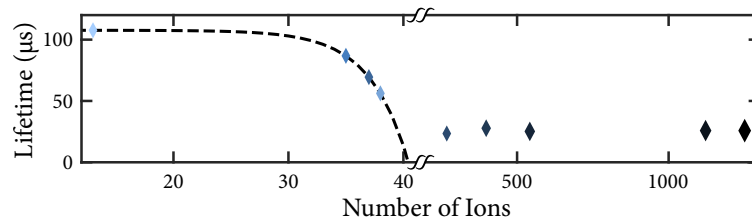


Figure 33: The lifetime of the  $^1D_2$  level decreases exponentially with the number of ions within the nanocrystals.

The  $^1D_2$  lifetimes of the nanocrystals decrease exponentially with the number of  $Pr^{3+}$  ions as depicted in Figure 33. To confirm that this behavior is no size effect, a measurement of the  $^1D_2$  decay was performed for the samples of the size series since these nanocrystals are 10-20 nm big and are doped with significantly more than 50 ions per nanocrystal. The resulting lifetimes were determined to be around  $25 \pm 2 \mu s$  and showed no dependence to the size or number of ions of the nanocrystals as inferred from Figure 33. From that, it can be concluded that cross relaxations drive the  $^1D_2$  depopulation. The mechanism starts with two adjacent ions which are in states ( $^1D_2$ ,  $^3H_4$ ), respectively, and exchange energy so that their final states are ( $^1G_4$ ,  $^3F_4$ ), compare Figure 11 [116].

#### 8.2.4 Estimation of Characteristic Lengths

The spectroscopic investigation of the concentration series yielded important observations that help to estimate characteristic lengths of the involved effects.

First, the nanocrystals experience strong multiphonon quenching which results in a very low quantum yield of  $<5\%$ . From that, the characteristic length for multiphonon quenching in the present nanocrystal system can be estimated to be around the half of the shortest dimensions of the nanocrystals which is  $\sim 3-4$  nm.

Second, there is a strong spectral broadening in the absorption but none in the emission. From that, it can be inferred that ions with spectrally broadened emission undergo multiphonon quenching. Following, the penetration depth of the local field into the nanocrystals is smaller than 3 nm.

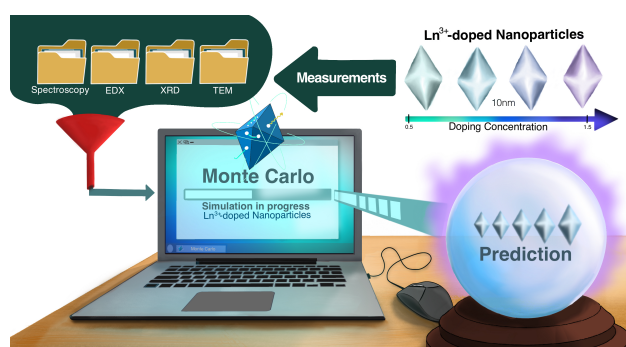
In the next part of this thesis, it will turn out that the characteristic length estimation for multiphonon quenching is quite accurate.



## Part III

### NUMERICS

In this part, a versatile modeling and simulation approach is presented that is able to reliably predict the excited state lifetimes and quantum yield of lanthanide-doped nanocrystals, here  $\text{LiYF}_4:\text{Pr}^{3+}$ . The model parameters were fitted to the experimental results of the concentration series presented and characterized in the previous parts. These parameters were employed to predict the experimental data of the size series with a maximum uncertainty of 12.6%. This numerical model is a powerful tool



for understanding, predicting, and optimizing lanthanide-doped nanocrystals regarding their emission dynamics.





---

**Contents**


---

9.1	The Numerical Approach . . . . .	69
9.2	From Rates to Probabilities . . . . .	71
9.2.1	Rates . . . . .	71
9.2.2	Spectral Overlap . . . . .	74
9.2.3	Relationship Between Energy Migration/Hopping and the Cross-Relaxations . . . . .	74
9.2.4	Process Probabilities . . . . .	75
9.3	Software and Computation . . . . .	76
9.3.1	Implementation . . . . .	76
9.3.2	Computational Resources . . . . .	77

---

In this chapter, the numerical model to understand and predict the spontaneous emission dynamics of lanthanide-doped nanocrystals is described. The most striking difference between the approach presented in this thesis and previously existing approaches is the spatial resolution of the presented approach that is achieved by transitioning from averaging rates to individual probabilities. The present chapter describes how to achieve this transition and concludes with technical information on the implementation of the approach and necessary computational resources.

### 9.1 THE NUMERICAL APPROACH

In the past, nanocrystal researchers already started to complement their experimental investigations with numerical simulations to gain deeper insights in the underlying dynamics. Most prominently, this has been the case for upconverting nanocrystals that allow for non-linear excitation of anti-Stokes emission by co-doping [110, 120–124], modeled in terms of a set of differential rate equations. This approach is widely used to model lasers [3, 47] and was iteratively improved to model nanocrystals. However, these simulations reach their limits at nanoscopic scales, which restricts them to a complementary role in nanocrystal research. Here, this limitation was addressed by employing a Monte Carlo approach which is depicted in the flow chart in Figure 34. It follows the subsequent steps:

At the start, the ions are randomly distributed within a nanocrystal of a given dimension. For this purpose, a database is created that contains one entry for every given ion. In this entry, the position of the

ion is stored as a three-dimensional coordinate. The ions are assigned one unit cell and one a unit cell is doped it cannot be assigned another ion. Each ion is assigned a flag for every involved process and initialize the flags as zero.

Next, excitation is randomly distributed within the available ions. To achieve this, the excitation flag of randomly chosen ions is set to one. The maximum excitation density is set to 50% which allows to neglect net amplification effects. After calculating the process rates, the probability for each process to occur is determined. This is based on probability theory considerations (see [Section 9.2.4](#) for details).

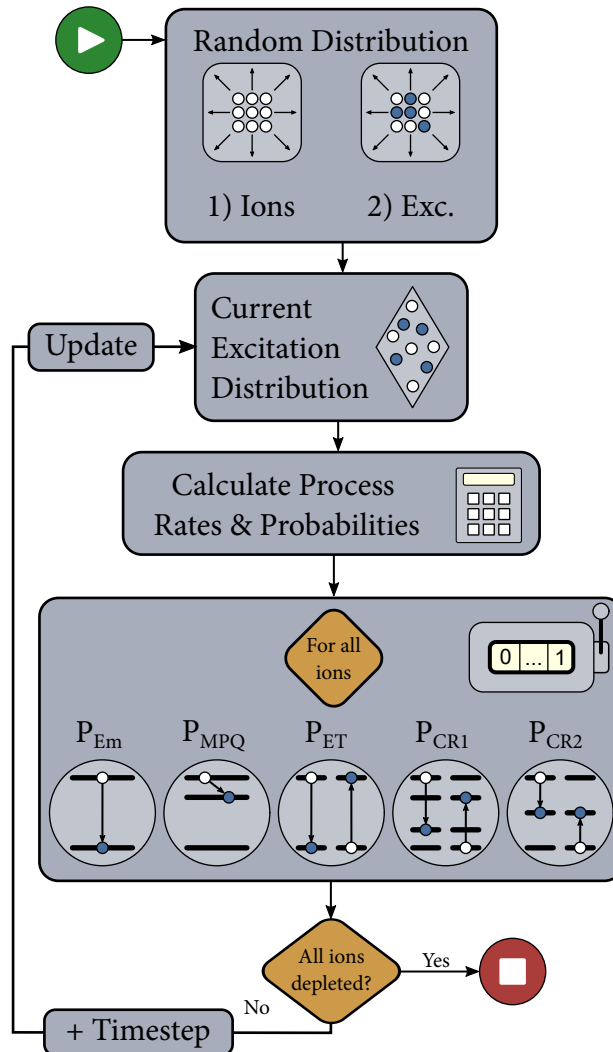


Figure 34: Flow chart of the Monte Carlo approach detailed in the main text. After randomly distributing the ions and the excitation energy the decision which process will occur is made for every ion based on probabilities and repeat this for as many timesteps as necessary to deplete all ions.

The main part determines the process that will occur. For every ion, first, the process rates are calculated and with that the probability for

every process. Next, one random variable between zero and one is generated and compared to the process probabilities to decide what happens. In the case of spontaneous emission, the excitation flag of the current ion is set to zero meaning that this excitation left the nanocrystal as a photon. For energy transfer, the flag of the current ion is set to zero and the flag of the respective adjacent ion to one. The levels involved in cross-relaxation,  $^1G_4$  and  $^3H_6$ , are known to exhibit lifetimes in the range of several milliseconds [71, 72, 125]. Since these lifetimes exceed the typical simulation window of around  $300 \mu\text{s}$  ( $\approx 10\tau_{\text{Bulk}}$ ) by around one order of magnitude, the energy is considered to be trapped in these levels during the further simulation. Respective ions are excluded from interaction with other ions or the surrounding medium. However, the situation is different for processes that involve the  $^1D_2$  level. As has been shown in Part II, emission from this level plays a special role in the spectroscopy of  $\text{LiYF}_4:\text{Pr}^{3+}$  nanocrystals. Therefore, spontaneous emission from that level was implemented in the numerical model.

Once the processes have been chosen for every ion the process flags are stored as part of the process statistics for later post-processing. A timestep of  $20 \text{ ns}$  is added which was considered a good trade-off between time consumption for the simulations and considerable changes of the probabilities. Then, the process restarts for the updated excitation distribution until all ions are depleted. The process statistics and spatial information of the decay dynamics are returned.

## 9.2 FROM RATES TO PROBABILITIES

Every individual ion is assigned a rate for each possible process whose mathematical foundations were already summarized in [Chapter 3](#). From these rates the process probabilities have to be calculated. The relevant details are presented subsequently.

### 9.2.1 Rates

The emission of photons occurs spontaneously and can be described by the Einstein coefficient  $A$  which is the inverse of the excited state lifetime  $\tau$  of a single ion in the nanocrystalline matrix. Spontaneous emission can be expressed as rate  $R_{\text{SpEm}}$  by

$$R_{\text{SpEm}} = -A \cdot t \quad (49)$$

which depends on the time  $t$ . Followingly, local field effects have to be taken into account since the surrounding medium affects the lifetime [96, 126, 127].

Lanthanide ions exchange energy either via electron exchange or through dipole-dipole interaction. These processes were described by Dexter and Förster [90, 91], respectively, and take place on different

length scales. While electron exchange occurs in the sub-nanometer range (typ.  $< 20 \text{ \AA}$ ) the dipole-dipole interaction can cover some nanometers (typ.  $< 10 \text{ nm}$ ). Therefore, Dexter energy transfer (DET) is referred to as energy migration and Förster energy transfer (FET) as energy hopping [128, 129]. The rate of the Dexter energy transfer

$$R_{\text{DET}} = \frac{1}{\tau} \exp \left[ \gamma \cdot \left( 1 - \frac{r}{r_0} \right) \right], \quad (50)$$

with  $\gamma = 2r_0/L$  and  $L$  being the effective Bohr radius. The rate of the Förster energy transfer is

$$R_{\text{FET}} = \frac{1}{\tau} \cdot \frac{d_0^6}{d^6}, \quad (51)$$

with the distances  $r$  (Dexter) and  $d$  (Förster) between donor and acceptor. Both processes depend on the excited state lifetime and a characteristic length of  $r_0$  (Dexter) or  $d_0$  (Förster) [90, 91, 130]. These two lengths are defined as follows: For the so-called Dexter radius, the energy transfer rate is equal to the rate for spontaneous emission. For the Förster distance, the energy transfer rate is 50% of the rate for spontaneous emission (c.f. Figure 13 in Section 4.3). Both characteristic lengths depend on spectral overlap of the energy donor and acceptor. The spectra relevant to this thesis are depicted in Figure 35. In the case of  $\text{LiYF}_4:\text{Pr}^{3+}$ , the energy donor is a Praseodymium ion in the upper-level  $^3\text{P}_0$  and the energy acceptor is a Praseodymium ion in the ground level  $^3\text{H}_4$ . Accordingly, two ions in levels ( $^3\text{P}_0$ ,  $^3\text{H}_4$ ) enter levels ( $^3\text{H}_4$ ,  $^3\text{P}_0$ ), see Figure 35a. Since the sum of energy in the  $^3\text{P}_0$  level does not change through this energy transfer it is considered energy-conserving.

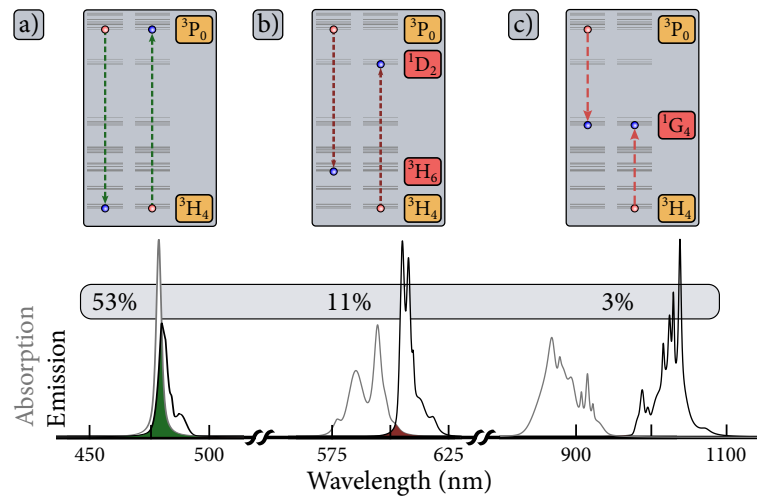


Figure 35: Representation of energytransfer (a) and cross-relaxations (b and c) considered in the model in the energy level diagram and their respective spectral overlap. NIR spectra were kindly provided by Leibniz Institut für Kristallzüchtung in Berlin.

Energy transfer between ions with complex energy level schemes can include intermediate energy levels resulting in well-known up-conversion or cross-relaxation (c.f. [Chapter 4](#)). In the case of  $\text{LiYF}_4:\text{Pr}^{3+}$ , two cross-relaxation processes are prominent and involve two ions in levels ( $^3\text{P}_0$ ,  $^3\text{H}_4$ ) that either enter the levels ( $^3\text{H}_6$ ,  $^1\text{D}_2$ ) or ( $^1\text{G}_4$ ,  $^1\text{G}_4$ ) (compare [Figure 35b](#) and [c](#)) [[69](#), [131](#)]. Even though this process conserves the sum of the excitation energy in the nanocrystal, it is considered lossy, as it depopulates the upper  $^3\text{P}_0$  level. The energy transfer rates only differ by the spectral overlap of the involved transitions. Therefore, the characteristic lengths for the lossy cross-relaxations and conserving energy transfer can be related to each other by a ratio of the spectral overlap, see [Section 9.2.2](#) for a detailed mathematical description.

Besides spontaneous emission and cross-relaxations, multiphonon quenching can depopulate the upper  $^3\text{P}_0$  level and populate the adjacent  $^1\text{D}_2$  level. Although this process is highly unlikely in bulk crystals, as the low phonon energy of  $480\text{ cm}^{-1}$  requires at least 7 phonons. This process gains relevance in the case of nanocrystals because they are dispersed in organic solvents, which exhibit higher phonon energies, leading to lower-order multiphonon interaction. In this thesis, the nanocrystals were dispersed in toluene with oleic acid as ligand system that both accept vibrational energies of the C-H bonds of up to ca.  $3000\text{ cm}^{-1}$  [[132](#)]. The energy difference between the  $^3\text{P}_0$  and  $^1\text{D}_2$  lies in that same order of magnitude consequently allowing for a single phonon transition. As already discussed in Part II,  $\text{LiYF}_4:\text{Pr}^{3+}$  nanocrystals thus exhibit an additional emission line at  $595\text{ nm}$  originating from the  $^1\text{D}_2$  level populated via the efficient multiphonon quenching pathway.

Multiphonon quenching is also a form of Förster energy transfer with the organic solvent acting as energy acceptor [[106](#)]. Consequently, multiphonon quenching, as an energy transfer mechanism, depends on a characteristic length mainly determined by the spectral overlap of the involved transitions. This length can in principle be calculated, but the single input parameters such as the dipole orientation strongly depend on the experimental conditions and are not readily accessible [[101](#)]. As these conditions are unknown, simple calculations to obtain the characteristic lengths are not possible. In this thesis, the characteristic lengths were obtained by comparison between experimentally and numerically determined excited state lifetimes. The lifetime acts as the main control parameter which in principle is sufficient but here, the measurement uncertainty of the quantum yield was much higher than the respective uncertainty of the lifetimes. Therefore, the quantum yield was only employed as additional control parameter to provide a simple cross check.

### 9.2.2 Spectral Overlap

According to Equation 29, Equation 30, and Equation 34, the ratio between the characteristic length scales of energy migration and cross relaxation can be determined from the spectral overlap between the interacting ions. Therefore, the absorption and emission spectra of the relevant transitions have to be measured. These spectra are depicted in Figure 35. For the cross relaxation mechanisms, from all possible mechanisms two were taken into account [131, 133, 134] whose spectroscopic data were experimentally available. The respective wavelength range can be estimated from the energy levels between the involved states. Therefore, absorption and emission spectra in the blue spectral region are needed for the energy migration and in the red region for the cross relaxation.

The spectra were recorded using different spectrometers such as described in Chapter 7 and Chapter 8 but also USB-spectrometers were used especially for the emission spectra. A bulk crystal with 0.5 at% doping concentration served as sample for these measurements.

To determine the spectral overlap the peaks actually involved in the respective transfer mechanism were selected and the spectrum was cut to this particular region of interest. The number of peaks in the measured spectrum was determined and then a respective number of functions were fitted to the data. Pseudo-Voigt profiles served as fit functions to account for all broadening mechanisms, c.f. Section 7.2.1. The fit was accepted if its integral did not deviate more than 0.5 % from the measured curve integral.

The fits of every absorption band were normalized on the photon energy scale so that the integral of the curve is one [91, 130]. From this data, the percental overlap was determined to be 53 %, 11 %, and 3 % for the blue, the red, and the infrared spectral range, respectively. The spectra and the overlap are depicted in Figure 35. on the wavelength scale.

### 9.2.3 Relationship Between Energy Migration/Hopping and the Cross-Relaxations

For the Dexter processes, Equation 34 and Equation 30 were used to obtain

$$\frac{r'_0}{r_0} = \frac{\ln J'}{\ln J}. \quad (52)$$

In this equation,  $r_0$  and  $r'_0$  are the characteristic lengths,  $J$  and  $J'$  the spectral overlap of the Dexter-process driven energy transfer and cross-relaxations, respectively.

For the Förster processes, Equation 29 was used and it is evident that  $d_0^6 \propto J$  and thus

$$\frac{d'_0}{d_0} = \frac{\sqrt[6]{J'}}{\sqrt[6]{J}}. \quad (53)$$

The ratios in Equations Equation 52 and Equation 53 were used in the simulations to express the characteristic lengths of the cross-relaxations through the characteristic length of the energy migration and hopping, respectively.

#### 9.2.4 Process Probabilities

The process probabilities for one ion were calculated from the respective rates  $R_i$  considering basic probability theory. There are six different events that are independent. These events are enumerated 1-6. Additionally, there is the probability that nothing happens. First, the probability for event  $i$  to occur is calculated in the time interval  $[0, \Delta t]$  while another event is still possible:

$$\begin{aligned} \mathbb{P}_{\text{event } i \text{ occurs in } [0, \Delta t]} &= \int_0^{\Delta t} R_i \exp(-R_i \cdot t) dt \\ &= 1 - \exp(-R_i \cdot \Delta t). \end{aligned} \quad (54)$$

Next, the probability for event  $i$  to occur is calculated within the above mentioned time interval but no further event  $n$ ,  $n \neq i$  occurs within this interval:

$$\mathbb{P}_{i \text{ occurs, others don't}} = \int_0^{\Delta t} R_i \exp(-R_i \cdot t) \prod_{\substack{n=1 \\ n \neq i}}^6 \exp(-R_n \cdot t) dt. \quad (55)$$

Here,  $\exp(-R_n \cdot t)$  is the probability that event  $n$  does not occur (c.f. Equation 54):

$$1 - \mathbb{P}_{\text{event } n \text{ occurs in } [0, \Delta t]} = \exp(-R_n \cdot \Delta t). \quad (56)$$

From that, Equation 55 can be reformulated:

$$\begin{aligned} \mathbb{P}_{i \text{ occurs, others don't}} &= R_i \int_0^{\Delta t} \exp\left(-\left(\sum_{n=1}^6 R_n\right) t\right) dt \\ &= \frac{R_i}{\sum_{m=1}^6 R_m} (1 - \exp\left(-\left(\sum_{n=1}^6 R_n\right) \Delta t\right)). \end{aligned} \quad (57)$$

Since only one of the events is possible the probabilities must sum up to unity. Therefore, the probability that nothing happens

$$\bar{\mathbb{P}} = 1 - (\mathbb{P}_1 + \dots + \mathbb{P}_6), \quad (58)$$

with

$$\begin{aligned}
 \mathbb{P}_1 + \dots + \mathbb{P}_6 &= \sum_{i=1}^6 \frac{R_i}{\sum_{n=1}^6 R_n} (1 - \exp(-\left(\sum_{n=1}^6 R_n\right) \Delta t)) \\
 &= 1 - \exp(-\left(\sum_{n=1}^6 R_n\right) \Delta t) \\
 &= 1 - \prod_{n=1}^6 \exp(-R_n \Delta t)
 \end{aligned} \tag{59}$$

and therefore  $\bar{\mathbb{P}}$  becomes

$$\bar{\mathbb{P}} = \prod_{n=1}^6 \exp(-R_n \Delta t). \tag{60}$$

Additional events can be accounted for by extending the number of processes in the sums and products.

### 9.3 SOFTWARE AND COMPUTATION

The previously presented numerical model was implemented and used to simulate the excitation dynamics of  $\text{LiYF}_4:\text{Pr}^{3+}$  nanocrystals. In this section the implementation details and the resources that were used for the computation are described.

#### 9.3.1 Implementation

The model has been implemented in Python 3. The program only needs the NumPy module (version > 1.18.4) for operation. NumPy is considered the fundamental package for scientific computing. Regarding the program, the random library provided by NumPy plays a prominent role since it provides the random numbers.

Generating true random variables is a complex task which can only be accomplished using physical experiments [135, 136]. In numeric investigations it is sufficient to generate pseudo-random numbers. Sequences from such generators are calculated using deterministic algorithms and thus can be repeated. In the present implementation the pseudo-random number generator is provided by the Python package NumPy.

Random variables generated with NumPy in Python are represented in floating-point arithmetic. This representation causes a round-off of any considered number, and introduces an error that is referred to as truncation error. Specifically, NumPy uses double precision type floating-point numbers, which are reliable up to 15–16 decimal places. The resulting loss in precision leads to the notion of a finite machine precision, which, in the given situation, is on the order of  $10^{-16}$ . In the simulations, this loss of precision affects all floating-point numbers



likewise. Consequently, random variables and probabilities underlie the same precision which was considered sufficient.

The model was implemented into a highly modular program. It can be readily extended to account for additional mechanisms or different geometries. To properly distribute the ions in the bi-pyramidal geometry of the  $\text{LiYF}_4:\text{Pr}^{3+}$  nanocrystals the spatial library provided by the SciPy module (version >0.12.0) was employed. The SciPy module offers a collection of mathematical algorithms and convenience functions for scientific computing which are built on the NumPy module.

### 9.3.2 *Computational Resources*

The simulations were run on a scientific computing cluster with 80 nodes provided by the Leibniz University IT Services (LUIS). Each node consisted of two Intel Cascade Lake Xeon Gold 6230N 2.3 GHz CPUs with 20 cores per CPU (40 cores per node, 3200 cores in total). A total memory of 192 GB was available per node. Total storage of 100 GB was available and necessary since files containing the process statistics easily exceeded 10 GB for one sample. The cluster is managed through the SLURM workload manager [137]. The respective jobscripts were generated automatically using Python 3 and included information on the computing resources, the necessary software, and the parameters relevant to the simulation. To make use of all available computing resources the simulations were parallelized. While simulations with <50 Ions and  $N=100$  repetitions took only 5-10 minutes per task more costly simulations with > 1k ions and  $N=10k$  took more than 24 hours.



## DETERMINATION OF THE CHARACTERISTIC LENGTHS

### Contents

10.1	Statistics . . . . .	79
10.2	Parameter Search . . . . .	80
10.3	Plausibility . . . . .	84

The characteristic lengths are crucial parameters to the simulations because they determine the rates and probability for the different Dexter and Förster processes. The determination of these lengths was a time consuming and complex task presented in this chapter.

### 10.1 STATISTICS

Before determining the characteristic lengths, the nanocrystals of the concentration series were simulated with arbitrary parameters and multiple simulations were run to determine the statistical deviation. The standard deviation  $\sigma$  was calculated by

$$\sigma = \sqrt{\frac{1}{N} \sum_{i=0}^N (\tau_i - \bar{\tau})^2}, \quad (61)$$

where  $\bar{\tau}$  is the average simulated lifetime and  $\tau_i$  the  $i^{\text{th}}$  simulated lifetime from a finite data set of  $N$  simulation runs.

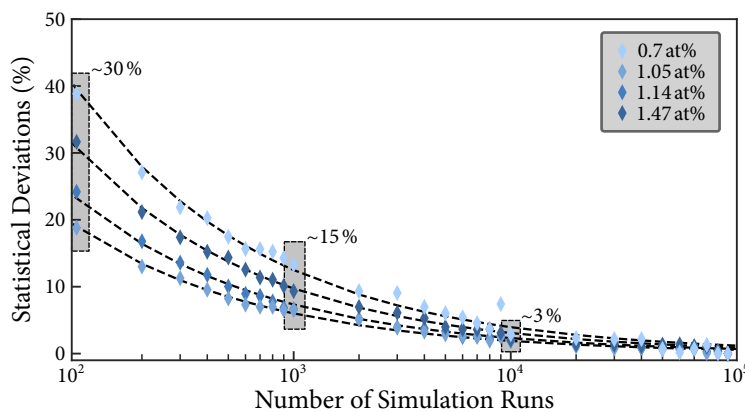


Figure 36: The standard deviation of the simulations decreases by  $1/\sqrt{N}$  with the number of simulation runs as expected from a simple sampling Monte Carlo approach. The numerical error is determined from this plot.

In [Figure 36](#), the standard deviations of the simulated excited state lifetimes is depicted for an increasing number of simulations. The depicted relation matches the expected  $1/\sqrt{N}$  trend: For a total of  $N=100$  simulations, the standard deviation amounts to 20 to 40% depending on the sample. For  $N=1000$  simulations, this deviation decreases to 10 to 15% and finally to 2 to 3% for  $N=10\,000$ .

## 10.2 PARAMETER SEARCH

To obtain the characteristic lengths, the respective three-dimensional parameter space was scanned in an iterative approach as depicted in [Figure 37](#). First, the parameter space was scanned with  $N=100$  simulations and broad parameter ranges of (0.1 – 8 nm, 2 – 20 Å, 0.1 – 11 nm) at a scanning resolution of (1 nm, 2 Å, 1 nm) for multiphonon quenching (MPQ), Dexter energy transfer (DET), and Förster energy transfer (FET), respectively. To gradually narrow down this parameter space, both, the number of simulations and the resolution of the parameters were iteratively increased (see [Figure 37](#)).

In this way, more precise results could be obtained as the actual parameters were approached.

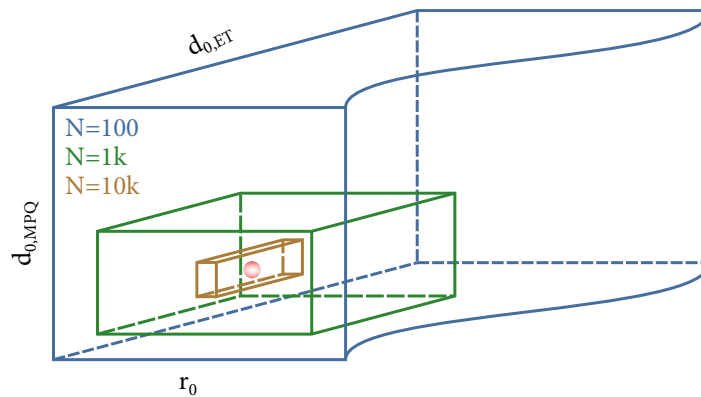


Figure 37: Graphical representation of the parameter search: To find the parameters in the three-dimensional parameter space an iterative algorithm was applied that increases resolution and numerical certainty at the cost of a broader scanning range.

To extract information from the parameter scans, the simulated lifetimes were averaged in two dimensions of the parameter space for all four samples of the concentration series and the result was plotted as a function of the remaining parameter. To further narrow down the relevant parameter space the averaging window was iteratively reduced in the two dimensions. This procedure was limited by simulation accuracy and resolution of the parameter steps. For the first scan, a polynomial of 6th order as well as an exponential function were fitted to the numerical results of the Förster and Dexter energy transfer-related processes, respectively, see [Figure 38](#).

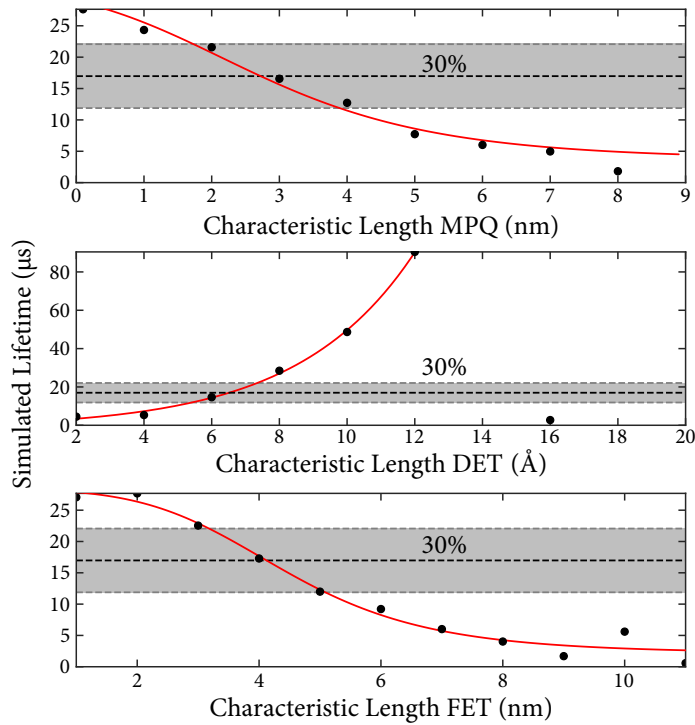


Figure 38: Graphical representation of the parameter search: To find the parameters in the three-dimensional parameter space, we applied an iterative algorithm that increases resolution and numerical certainty at the cost of a broader scanning range. The indicated 30% represent the expected standard deviation of the simulated data and limit the accepted parameter range.

This served as a first cross-check for the validity of the simulations because these analytical functions govern the respective processes. For the first iteration, those parameters which deviated around  $\pm 30\%$  from the average measured values (c.f. [Figure 36](#)) were chosen.

For the second scan,  $N=1000$  independent instances were analyzed with a resolution of  $0.5 \text{ nm}$ ,  $1 \text{ \AA}$ ,  $0.5 \text{ nm}$  for multiphonon quenching, Dexter and Förster energy transfer, respectively. The results correlate linearly, consequently, linear functions were fitted to the data which yielded coefficients of determination close to one indicating an excellent fit quality, see [Figure 39](#).

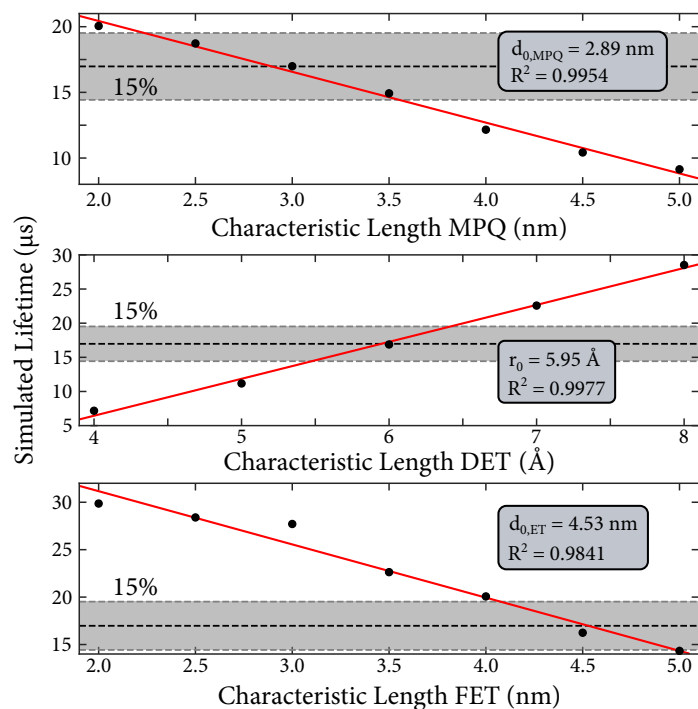


Figure 39: Graphical representation of the parameter search: To find the parameters in the three-dimensional parameter space, we applied an iterative algorithm that increases resolution and numerical certainty at the cost of a broader scanning range. The indicated 15% represent the expected standard deviation of the simulated data and limit the accepted parameter range.

To determine the first set of the characteristic lengths, the intersection between the linear functions and the averaged value from the measurement were calculated. For improved accuracy, parameters that deviated only around  $\pm 15\%$  from the average measured excited state lifetime were simulated. From this last parameter scan, the characteristic lengths were identified to be 3 nm, 6  $\text{\AA}$ , 4.5 nm for multiphonon quenching, Dexter, and Förster energy transfer, respectively, see [Figure 40](#).

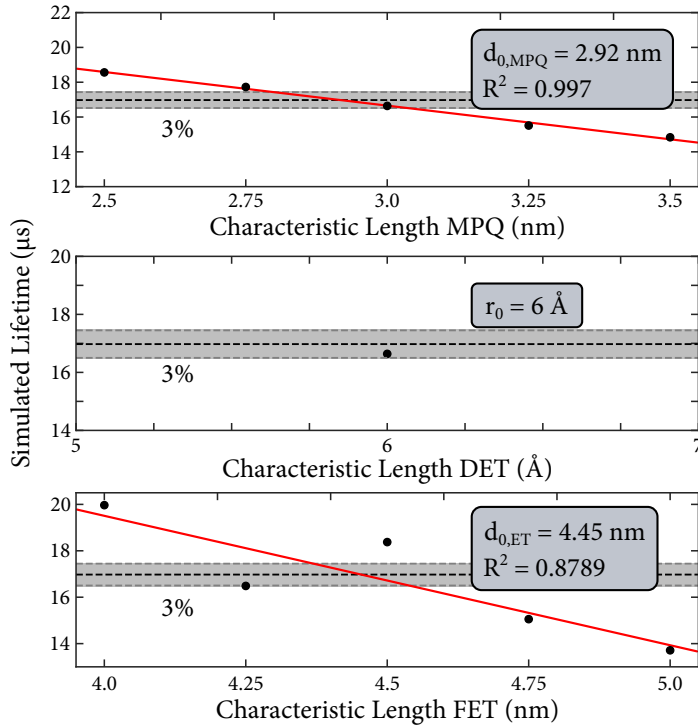


Figure 40: Graphical representation of the parameter search: To find the parameters in the three-dimensional parameter space, we applied an iterative algorithm that increases resolution and numerical certainty at the cost of a broader scanning range. The indicated 3% represent the expected standard deviation of the simulated data and limit the accepted parameter range.

The characteristic lengths were obtained by including the measured excited state lifetime of the  $^1\text{D}_2$  level in the simulations. However, having to include this level constitutes a disadvantage because the  $^1\text{D}_2$  lifetime needs to be known prior to any simulation thus preventing predictions of unknown nanocrystals with the presented numerical approach. To check for the potential to further simplify the energy level scheme and enable predictions with the numerical approach the last parameter scan was repeated with different  $^1\text{D}_2$  lifetimes, see [Figure 41](#). Finally, parameters were obtained that deviated by less than 7% from the initial scan by neglecting emission from the  $^1\text{D}_2$  level. Consequently, the simulations were continued with this less complex model.

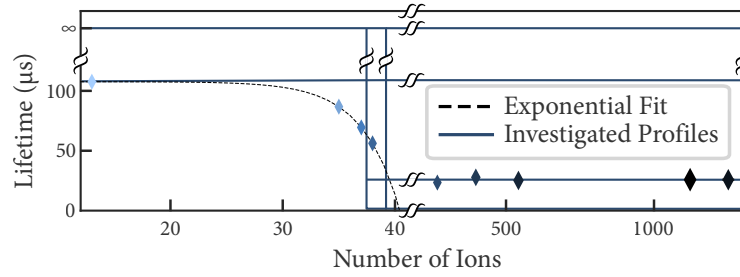


Figure 41: Lifetimes of the  $^1D_2$  level investigated to further simplify the energy level scheme. The symbols depict the measured lifetimes and the blue lines constitute different approximations. Each possible combination of lifetimes represented by the lines was investigated.

### 10.3 PLAUSIBILITY

In Section 8.2.4, a characteristic lengths of  $\sim 3 - 4$  nm was estimated for multiphonon quenching from the spectroscopic results. With the numerically determined characteristic length of 3 nm the experimental estimate turned out surprisingly accurate and the spectroscopic result serves as a first plausibility check.

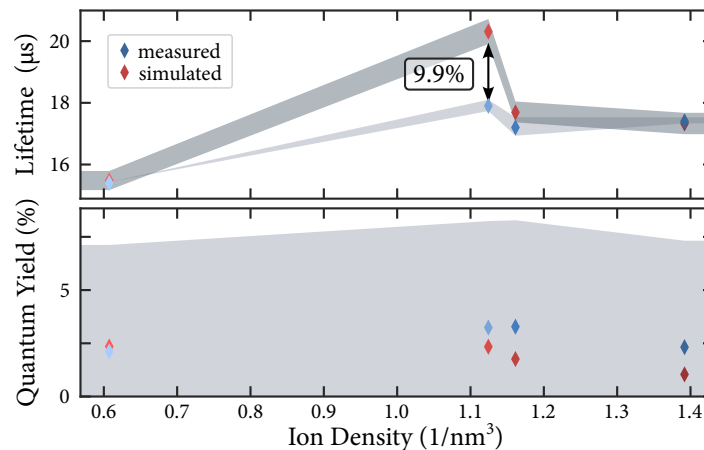


Figure 42: Comparison of the experimental figure-of-merit with the simulated results obtained with the parameters from the characteristic length determination. Note, that the markers represent the samples of the concentration series.

As a second check, the samples of the concentration series were simulated with the identified characteristic lengths, and it was found that the numerical results match the experimental value extraordinarily well. As evident from Figure 42, the maximum deviation of simulation and measurement amounts to only 10%, taking into account the numerical and experimental errors of the excited state lifetime. For the quantum yield, this deviation can not be determined accurately due to the large experimental measurement error.



Overall, the chosen numerical approach and the determined characteristic lengths seem to describe the excitation dynamics of the nanocrystals. For further verification, the samples of the size series were employed, as described in the next chapter.



### Contents

11.1 Prediction of the Size Series . . . . .	87
11.2 Process statistics . . . . .	88

Since the samples of the size series were not involved in the parameter search they are suitable to independently verify whether the numerical approach and the characteristic lengths can describe and, more importantly, predict the excitation dynamics in the nanocrystals. Therefore, the characteristic length were used to simulate the excitation dynamics of the size series. The results of these simulations are presented in the present chapter.

#### 11.1 PREDICTION OF THE SIZE SERIES

The simulations of the size series yielded that the excited state lifetimes were predictable with a maximum deviation of only 12.6%. These samples were not involved in determining the characteristic lengths. Furthermore, the ion density of these samples is one order of magnitude higher than in the concentration series. It can be concluded that these simulations verify and validate the numerical model.

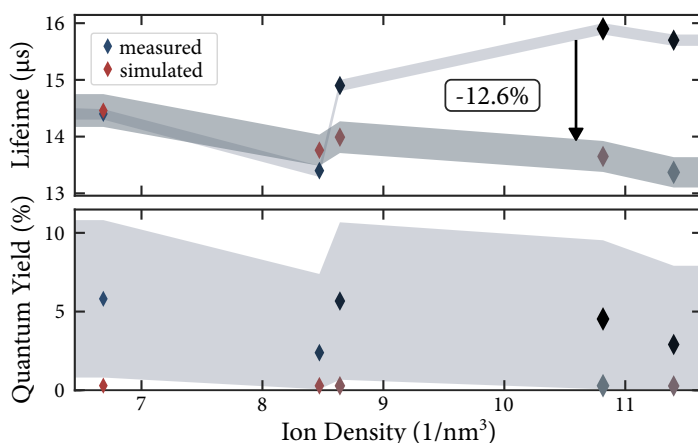


Figure 43: Measured and simulated lifetime and quantum yield of the size series. The numerical model predicts the spectroscopic performance of these samples.

Below ion densities of 8.5 ions per nm<sup>3</sup>, the simulation and measurement agree within the respective uncertainties, see [Figure 43](#).

Above this value, the deviation increases. Interestingly, the deviations increase with the size of the nanocrystals indicating that the model becomes less accurate for larger nanocrystals with a doping concentration of 5 at%. On one hand, this could result from the simplifications introduced within the numerical model. For example, the determined characteristic lengths might underlie inaccuracies if the considered cross relaxations need to compensate for the cross relaxations that were not considered in the model. Furthermore, the model traps energy that is quenched via cross relaxations although it might return to the dynamics via upconversion processes. On the other hand, the decreasing agreement of experiment and simulation with increasing nanocrystal size could result from the slight size mismatch of the  $\text{Pr}^{3+}$  ions that occupy the site of an  $\text{Y}^{3+}$  ion in the nanocrystals. This mismatch might result in distortions and defects within the nanocrystal that lead to the observed deviations. Altogether, one has to keep in mind that the simulated dynamics do not necessarily constitute the actual dynamics within the nanocrystals. However, the simulated dynamics constitute a model that is able to return the correct control parameters, namely the lifetime and quantum yield. Since the experimentally and numerically obtained lifetime deviates by only  $\approx 1.5 \mu\text{s}$  for 5 at% doped nanocrystals of 21 nm size the mismatch between experiment and simulation might be acceptable for most applications.

For the quantum yield of the size series, the broad underground in the emission spectra of the nanonano-crystals originating from oleic acid content could not be readily removed from the measurement. Therefore, the real experimental quantum yield is estimated to be at least 1% lower than the values depicted in [Figure 43](#). Due to the comparatively large experimental error, the true deviation is difficult to determine as described in [Section 10.3](#).

## 11.2 PROCESS STATISTICS

To gain a deeper insight into the excitation dynamics inside the nanocrystals the process statistics were analyzed. Interestingly, those processes dominating the excitation dynamics start at a high level and drastically decrease within the first microsecond, see [Figure 60](#) to [Figure 68](#) in the Appendix.

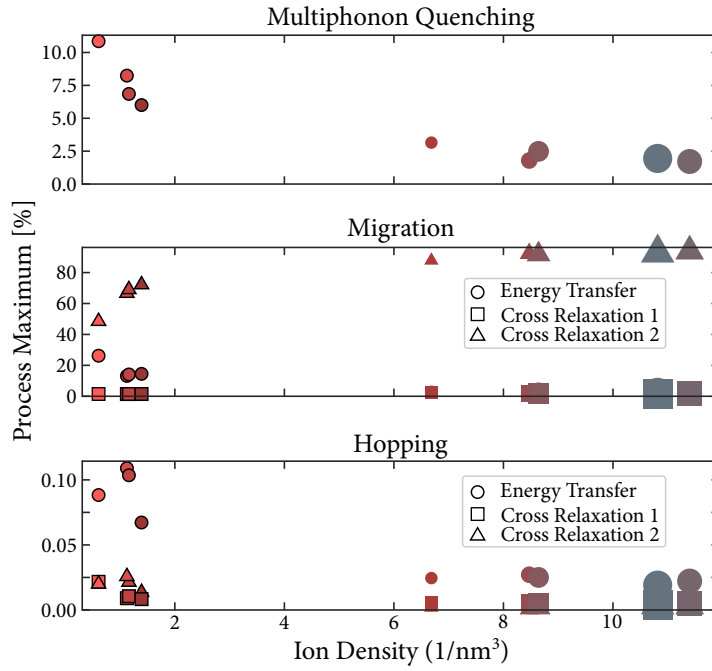


Figure 44: The process statistics of all samples exhibit that multiphonon quenching decreases with the nanocrystal size, and concentration quenching drastically limits the performance of the nanocrystals.

However, the relative process maxima vary for the different samples as depicted in Figure 44. The multiphonon quenching shows a maximum of around 10% for low ion densities and decreases with higher ion density. This is plausible since the nanocrystal volume increases and approaches bulk-like situations in which the surface-to-bulk-ion ratio decreases and thus reduces the relevance of multiphonon quenching to the surrounding medium. While hopping processes are negligible with relative process maximums well below 1%, the migration processes strongly influence the dynamics. Migrating energy transfer decreases with the ion density at the cost of an increase in migrating cross-relaxation. This is comprehensible as concentration quenching is known to increase for high doping concentrations [7]. Furthermore, the decrease in the multiphonon quenching coincides with the decrease in the migrating energy transfer. It can be inferred that energy migrates to the surface of the nanocrystals where the quenching occurs. This process loses relevance with increasing ion density as concentration quenching becomes more dominant.



---

**Contents**

12.1 Simulation of Core-Shell nanocrystals . . . . .	91
12.2 Process Statistics . . . . .	92
12.3 Resource-related Potential . . . . .	93

---

The previous chapter demonstrated that the numerical approach can be employed to predict the excitation dynamics of the nanocrystals. This finding implies that optimization of lanthanide nanocrystals can be done numerically without the time consuming and resource consuming synthesis of nanocrystals necessary for an experimental approach. To showcase that, the results of a simple optimization approach are presented in this chapter.

### 12.1 SIMULATION OF CORE-SHELL NANOCRYSTALS

To demonstrate the numerical optimization potential, all nanocrystal samples were simulated with an inert shell, see [Figure 45a](#). This numerical optimization step is only possible because the presented modeling approach accounts for the spatial distribution enabling to simulate the underlying surface effects in contrast to previous numerical approaches based on rate equations [58, 138]. Based on simple estimations, it is evident that the efficiency of the dipole-dipole interaction decreases to 1.5% if the distance between the energy donor and acceptor is twice the characteristic length, see [Figure 13](#) and [Equation 51](#). Therefore, a shell thickness of 6 nm was chosen since it is twice the characteristic length the parameter search revealed.

[Figure 45b](#) depicts the measured lifetimes and quantum yields of the synthesized samples and the respective simulated results of the numerically optimized nanocrystals (red-to-blue color coded bipyramids with border). The undoped shell led to a drastic increase in the excited state lifetime. The lifetime of the concentration and size series increased by 32% and 44%, respectively, with a maximum of above 20  $\mu\text{s}$ . On the other hand, the quantum yield increases to a maximum of 6%. This is only one percentage point above the measurement uncertainty of the setup used in this thesis but constitutes an increase factor of 3 compared to the value obtained without shell. Furthermore, the increase of the quantum yield strongly depends on the ion density and becomes vanishingly small at densities above one ion per  $\text{nm}^3$ , see [Figure 45b](#). Altogether, there is no trend observable

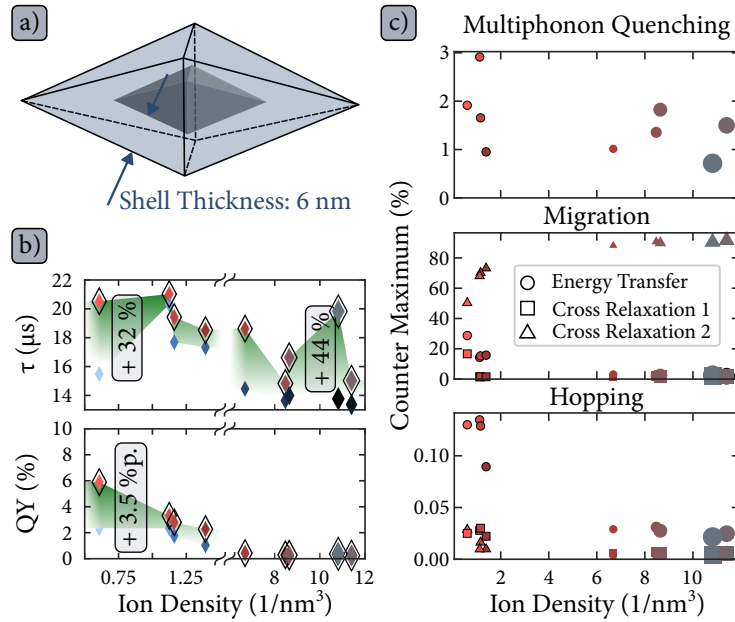


Figure 45: a) Schematic of the core-shell nanocrystals with a shell thickness of 6 nm. b) The shell (red-to-blue color-coded bipyramids with border) drastically increases the excited state lifetime by a maximum of 44% and also improves the quantum yield by 3.5 percentage points. c) The shell suppresses multi-phonon quenching. The performance of such nanocrystals is limited through concentration quenching.

in the results. This emphasizes the complex nature of the excitation dynamics in lanthanide-doped nanocrystals and highlights that understanding the behavior of the nanocrystals through interpolation of experimental data is not readily possible.

## 12.2 PROCESS STATISTICS

Again, the process statistics were analyzed to gain deeper insights into the underlying physics. As in the case of the core-only nanocrystals, the processes dominating the excitation dynamics start at a high level and drastically decrease within the first microsecond (see Figure 69 to Figure 77 in the Appendix). Again, the relative process maxima vary for the different samples as depicted in Figure 45c. The shell reduces multiphonon quenching by a factor of approximately 5. It can be inferred that this reduction allows for the higher simulated excited state lifetimes [34, 109–113]. Since the further processes show no significant deviation from the core-only nanocrystals it can be furthermore inferred that in core-shell nanocrystals concentration quenching based on the Dexter transfer is the limiting process and prevents higher quantum yields.



### 12.3 RESOURCE-RELATED POTENTIAL

It is trivial that simulations save resources. However, in the case of lanthanide nanocrystals the resource-related saving potential is enormous because approaching the strategy of experimentally adding a shell around lanthanide nanocrystals includes:

1. Synthesis of the core nanocrystals and growing the shell,
2. structural characterization (TEM, EDX, XRD, etc.), and
3. optical characterization (lifetimes and quantum yield).

This effort can now be replaced by the simulations and allows to save aforementioned resources.

Additionally, the necessary experimental effort is optimistically estimated to consume at least one person-month (20 days à 8 h; 160 h) plus operating costs for the synthesis and characterization instruments. In contrast, the numerical approach took 2 hours at maximum to start the simulations and another 6 hours at maximum for analysis resulting in a time saving of more than 95 % compared to the experimental approach. The simulations themselves took approximately 48 hours, however, no human interaction was necessary during this period. Indeed, a high-end computing cluster was used but these simulations could also run on a personal computer.

Altogether, this highlights the potential the presented simulations to save resources and their relevance to the field of nanocrystal synthesis.



Part IV

CONCLUSION



---

**Contents**


---

13.1 Spatial Decay Dynamics . . . . .	97
13.2 Intelligent Optimization . . . . .	98
13.3 Prospect on Potential Application of Optimized Nanocrystals in Photonics . . . . .	100

---

The ability of the numerical approach to track the spatial dynamics within the nanocrystals will for example allow to research effects that currently cannot be investigated experimentally. Another promising direction is to numerically optimize  $\text{LiYF}_4:\text{Pr}^{3+}$  nanocrystals and transfer these nanocrystals into application. Such potential fields of application are presented in this chapter as well, and a special focus lies on applications that were already investigated during the creation of this thesis.

### 13.1 SPATIAL DECAY DYNAMICS

The presented simulation approach enables the spatiotemporal analysis of the dynamics within nanocrystals and, thus, can open up new research topics. To highlight this advantage, single core-only as well as core-shell nanocrystals were simulated and the average distance of the excitation energy from the center of the nanocrystals was calculated, see [Figure 46](#).

Independent of the structural characteristics, energy seems to move toward the surface of the nanocrystals, even in the case of core-shell structures. This is indeed an interesting observation, but it has to be kept in mind that these results only depict the spatial energy movement in one single nanocrystal.

Nonetheless, it is noteworthy that some of the nanocrystals exhibit oscillations of the average energy position, see the insets in [Figure 46](#). These oscillations point towards a special type of energy trapping where energy transfer occurs so fast that no competing loss mechanism can extract the energy from the nanocrystal. These oscillations were observed only for nanocrystals from the concentration series and, therein, only for the two samples with the lowest number of ions. The longest continuous oscillation lasted for about  $1\ \mu\text{s}$  (6% of the lifetime) and took place between 1 nm and 2 nm from the center of the respective nanocrystal. However, a series of short-timed oscillations (ca.  $300\ \text{ns}$ , 1.5% of the lifetime) that were interrupted

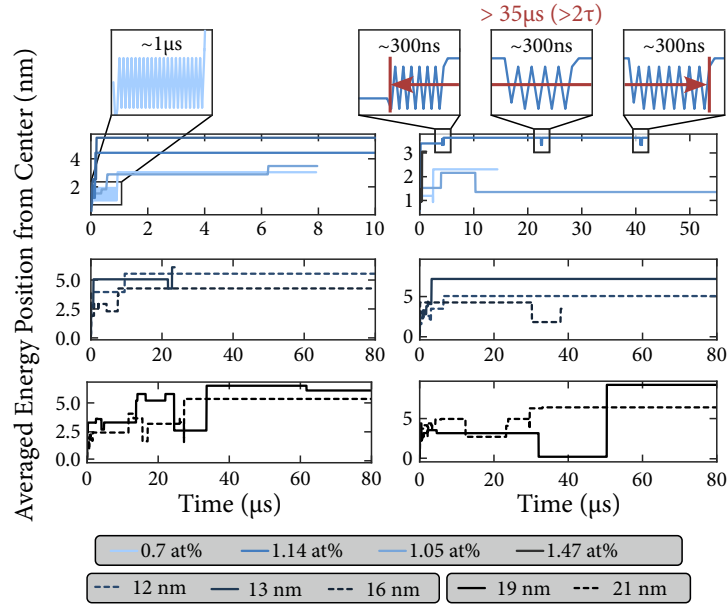


Figure 46: Spatial analysis of single nanocrystals consisting of core-only (left) and core-shell (right): Energy tends to move towards the particle surface and that some ion pairs seem to act as oscillating energy traps.

by periods of stagnation at one position was also observed within one nanocrystal. This whole series lasted about  $35 \mu\text{s}$  and took place about  $3.5 \text{ nm}$  from the center of the nanocrystal. Remarkably, the energy has been trapped in this individual nanocrystal for more than twice the lifetime determined in the experiments and simulations. It can be speculated that such an effect can be exploited to drastically increase the spontaneous emission lifetime or to store information within nanocrystals.

To draw more detailed conclusions multiple simulations and an in-depth analysis are required. Both will be performed in future works. At the same time, the experimental demonstration of these effects poses a great challenge since the motion of the energy needs to be spatially tracked on a sub-nanoscale. This could be achieved by combining atomic resolution electron tomography [139] with real-time single photon detection [140].

### 13.2 INTELLIGENT OPTIMIZATION

Apart from that, Monte Carlo approaches will allow for further investigations on the excitation dynamics within nanocrystals. During the time this thesis was written, first manuscripts were published that employed Monte Carlo approaches, e.g., for enhancement of the upconversion emission of  $\text{NaYF}_4:\text{Er}^{3+}, \text{Yb}^{3+}$  nanocrystals [141], to prevent quenching in  $\text{LiYF}_4:\text{Yb}^{3+}$  nanocrystals [67], or to investigate the influ-

ence of different quenching mechanisms in  $\text{K}_2\text{TiF}_6:\text{Mn}^{4+}$  phosphors [142].

One obvious application of the Monte Carlo approach presented in this work is to numerically optimize lanthanide nanocrystals. The most simple nanocrystal optimization approach would be an iterative scanning approach, comparable to the parameter search presented in Chapter 10. In this case, the parameters to be optimized, e.g., doping concentration, core geometry, and shell thickness, would be employed as parameter space and simulations for every parameter triple need to be run. The experiences drawn during the present thesis show that such a procedure is extremely time-consuming.

Therefore, intelligent optimization approaches could be highly favorable. One promising strategy is called Bayesian optimization which is a probabilistic, model-based approach for finding the global optimum, e.g. maximum or minimum, of black-box functions. It consists of four components as sketched in Figure 47 (i) the black-box function, (ii) the surrogate model, (iii) the acquisition function, and (iv) an optimizer. The black-box function refers to the target function that needs to be optimized. This function is typically unknown or expensive-to-evaluate. The surrogate model is typically a Gaussian Process that approximates the black-box function as a multivariate Gaussian distribution. A Gaussian Process models the black-box function as a collection of random variables with a mean and covariance function determined by the available observations. The mean and covariance function together form a probabilistic model of the black-box function that can be used to predict unobserved points. The acquisition function balances exploration and exploitation by guiding the selection of the next evaluation point. One often-used acquisition function is the so-called expected improvement which is a measure of the expected increase in the target function compared to the current best value. The optimizer is used to maximize the acquisition function to determine the next evaluation point. Once the global optimum is found or a pre-defined stopping criterion is met the optimization process stops.

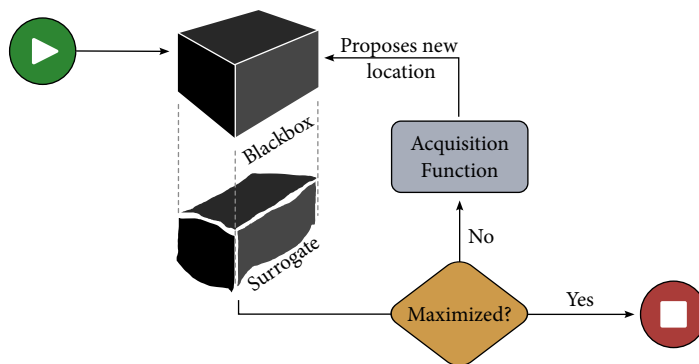


Figure 47: Flow chart of a Bayesian optimization algorithm.

Since Bayesian optimization can find the global maximum of a unknown function, it is particularly interesting for the maximization of the lifetime and quantum yield of  $\text{LiYF}_4:\text{Pr}^{3+}$  nanocrystals. In the case of the excitation dynamics simulations, the numerical approach presented in this thesis will be assigned to generate observed points that serve to explore the black-box function. The optimization process can reveal optimal parameters for doping concentration, core size, and shell thickness. Such optimization process might lead to completely new nanocrystal designs. This approach will be pursued further in future works.

### 13.3 PROSPECT ON POTENTIAL APPLICATION OF OPTIMIZED NANOCRYSTALS IN PHOTONICS

Praseodymium-doped nanocrystals with high excited state lifetimes and quantum yields are predestined for several applications. To give a further outlook, these applications will be highlighted and supplemented in this section.

Bulk crystals of  $\text{LiYF}_4:\text{Pr}^{3+}$  are well-known for efficient lasing in the visible spectral range but can be only implemented in alignment-prone free-space resonators. Nanocrystals, on the other hand, have the potential to be applied in arbitrary forms. For example, combining nanocrystals with polymers of optical quality such as PMMA might yield novel opportunities in combination with additive manufacturing, especially, since common laser-active dopants for polymers such as Rhodamine B show extensive bleaching and need high pump energies as was demonstrated in [20]. Since the maximum amount of nanocrystals in such polymer is limited to 0.5 wt% the requirements for the efficiency of the nanocrystals is very high [40].

Another interesting host medium for a composite laser is fused silica glass since a  $\text{LiYF}_4:\text{Pr}^{3+}$  nanocrystal doped optical fiber would allow for a rugged and flexible visible fiber laser that is compatible to standard fiber components [6, 143]. However, doping  $\text{LiYF}_4$  nanocrystals into such glass is a big challenge because fused silica is manufactured at temperatures around  $2000^\circ\text{C}$  while  $\text{LiYF}_4$  melts at  $850^\circ\text{C}$  and will diffuse due to the high temperatures during preform manufacturing. This could be circumvented by filling capillary fibers with a dispersion consisting the nanocrystals. This approach is currently explored using CdSe/CdS core/crown nanoplatelets [37].

Optimized lanthanide nanocrystals also find application in nanothermometry that uses two thermally coupled energy levels in lanthanide ions to measure temperature via ratiometry of the respective emission lines. This measurement principle has been applied to different sensing concepts. For example, a sensor based on a polymer fiber was demonstrated that can withstand high electric fields of up to  $12.5\text{ kV/cm}$  [40]. In another concept, upconversion nanocrystals



were attached to a fused silica fiber to measure the temperature inside a proton exchange membrane water electrolysis cell [37]. In a further numerical work, it was demonstrated that lanthanide-doped nanocrystals can be used for nanothermometry below the diffraction limit [44]. The nanocrystals used in this field are mostly  $\text{NaYF}_4:\text{Er}^{3+}, \text{Yb}^{3+}$  nanocrystals, so-called upconversion particles. They are excited in the infrared spectrum and nonlinear energy transfers between the absorbing Yb and emitting Er ions allow for visible emission, however, at quantum yields well-below a few percent. The low quantum yields call for comparatively high optical excitation powers that result in self heating and might distort the measurement [40]. Therefore, optimized  $\text{LiYF}_4:\text{Pr}^{3+}$  nanocrystals with high quantum yields exhibit the potential to replace the upconversion nanocrystals. The presented numerical approach might hence contribute to the optimization of upconversion nanocrystals.

With their forbidden 4f transitions, trivalent lanthanides exhibit lifetimes in the range of micro- and milliseconds which makes them promising candidates for quantum memories. One challenge in this field is to find quantum memories compatible with the world-wide fiber network, i.e., such memories need to be implemented in fiber technology and operate in the telecom wavelength range. Praseodymium-doped nanocrystals could play an integral role since they exhibit optical transitions compatible with telecommunication, e.g., the ones involving the  $^1\text{G}_4$  level. Although there is currently no approach known to integrate single  $\text{LiYF}_4:\text{Pr}^{3+}$  nanocrystals in fused silica fibers or respective fiber components solving this constitutes an interesting challenge for future works. In any case, it would have to be ensured that the ions in a quantum memory nanocrystal cannot interact with each other to prevent information loss. This could be achieved through low doping concentrations at comparatively large particle sizes or multiply alternating doped cores and undoped shells with suitable thickness.

Altogether, the work presented in this thesis forms an excellent basis to further research fundamentals and applications of lanthanide-doped nanocrystals. „There is plenty of room at the bottom“ [30].



SUMMARY

---

The numerical simulations on the excitation dynamics in lanthanide nanocrystals presented in this thesis contribute to a deeper understanding of the underlying processes. They carry the potential to enable the numerical optimization of nanocrystals and reveal new spatiotemporal effects. So far, current approaches were based on rate equations and spatially limited because they consider an averaging model that cannot account for single ions. These approaches origin from the modeling of laser active bulk crystals and, consequently, play a minor role in nanocrystals research.

This thesis presented a new numerical approach based on a Monte-Carlo algorithm that can describe and, more importantly, predict the excitation dynamics in lanthanide-doped nanocrystals. The presented approach accounts for all relevant processes that determine the excitation dynamics. Physical processes, energy levels, or custom nanocrystal geometries can readily be added or removed which makes the approach flexible and, thus, applicable for all types of lanthanide-doped nanocrystals.

The performance of the numerical approach was demonstrated employing  $\text{LiYF}_4:\text{Pr}^{3+}$  nanocrystals. A total of nine samples, of which four constituted a concentration series and five constituted a size series, were investigated. These samples were synthesized and structurally characterized at the Fraunhofer CAN. The structural characterization presented in the first part of this thesis yielded important key input parameters to the numerical simulations of the nanocrystals such as the morphology, size, and number of  $\text{Pr}^{3+}$  ions.

A comprehensive spectroscopic analysis was carried out and presented in Part II of this thesis. This analysis consists of absorption and emission spectroscopy, i.e., emission spectra, excited state lifetimes, and quantum yield. By comparison of the spectroscopic behavior of the nanocrystals to macroscopic bulk crystals strong multiphonon quenching was found which results in small quantum yields well below 5%. At the same time, the multiphonon quenching efficiently populates the  $^1\text{D}_2$  state, which yields strong emission at 595 nm that cannot be observed by exciting the  $^3\text{P}_0$  level in bulk crystals. The excited state lifetime of this transition was found to be limited by cross-relaxations and is comparable to the  $^1\text{D}_2$  lifetimes of bulk crystals for small nanocrystals with low doping concentration. The results of the spectroscopic analysis supported building the numerical model that was used to simulate the excitation dynamics. The excited state

lifetimes and quantum yields acted as control parameters for the numerical results.

The numerical approach and simulation results were presented in Part III of this thesis. A Monte Carlo algorithm was developed that can model the excitation dynamics by taking the spatial position of single ions into account. The underlying physical processes rely on a characteristic length that cannot readily be determined analytically since relevant experimental parameters such as dipole-dipole orientation or the local overlap spectra, are not experimentally accessible. Consequently, these parameters were determined in an iterative scanning approach using only the nanocrystals from the concentration series. With these parameters, the central result of the present thesis was achieved: the numerical results predicted the lifetimes and quantum yields of the size series with a maximum deviation of 12.6%. Furthermore, analysis of the process statistics enabled insight into the mechanisms that drive the excitation dynamics in the nanocrystals. In a first optimization step, a prominent strategy to improve the quantum yields of lanthanide-doped nanocrystals was applied, and simulations with a undoped shell added to the nanocrystals were performed. This optimization yielded drastically increased lifetimes and quantum yields of which the maximal values were improved by 44% and 3.5 percentage points, respectively. It is worth to mention that these simulations consumed much less resources than previous employed experimental approaches. Consequently, the numerical approach presented in this thesis carries the potential to constitute a paradigm change in nanocrystal research. Apart from that, the model allows for new insights in dynamics inside lanthanide-doped nanocrystals. For example, the spatial analysis of the excitation dynamics in single nanocrystals revealed oscillations that point towards a new type of energy trapping.

In the future, this numerical approach will be combined with intelligent optimization algorithms to develop  $\text{LiYF}_4:\text{Pr}^{3+}$  nanocrystals with bulk-like  $^3\text{P}_0$  lifetimes and high quantum yields with applications in laser physics, nanothermometry, or even quantum memories. The possibility to resolve the spatial dynamics enables investigations on spatiotemporal effects in lanthanide-doped nanocrystals that are currently not accessible in experiments. The universality of the numerical approach allows for application in other lanthanide nanocrystal systems such as the prominent classes of upconversion or photon avalanching nanocrystals.

Part V

APPENDIX



## ADDITIONAL RESULTS FROM THE STRUCTURAL CHARACTERIZATION

**Contents**

15.1	Transmission Electron Microscopy Pictures . . . . .	107
15.2	Element Mapping and Linescans . . . . .	110

The results presented in this part of the Appendix were obtained and provided by the Fraunhofer Center for Applied Nanotechnology.

## 15.1 TRANSMISSION ELECTRON MICROSCOPY PICTURES

Figure 48 shows detailed TEM pictures for the concentration series.

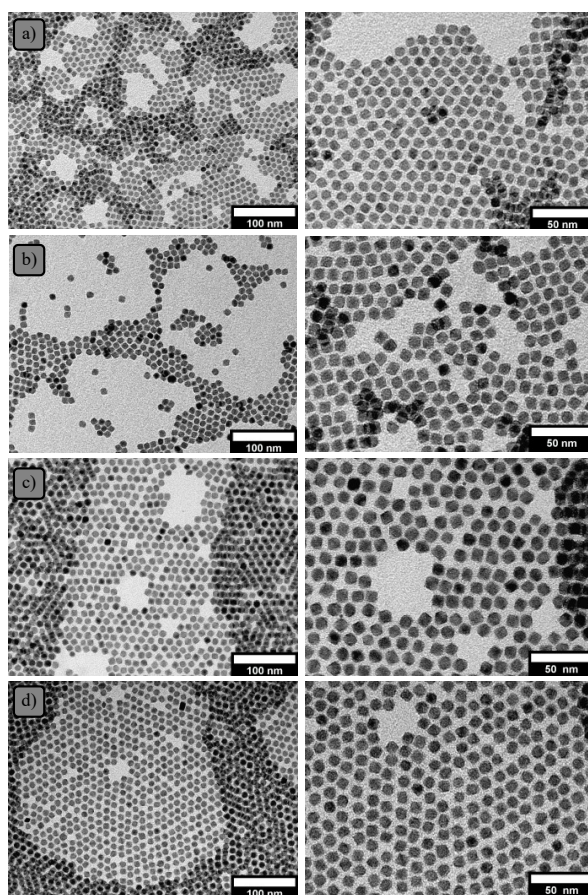


Figure 48: TEM pictures of the concentration series a) 0.7 at%, b) 1.05 at%, c) 1.14 at%, d) 1.47 at%.

Figure 49 shows detailed TEM pictures for the first sample of the size series.

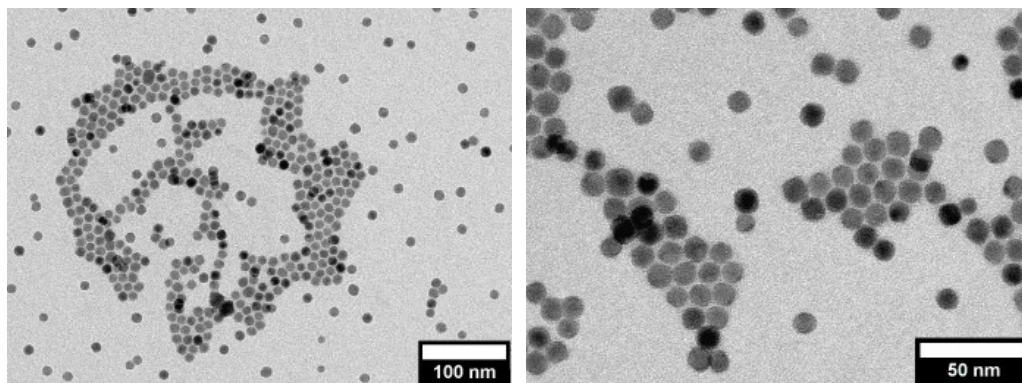


Figure 49: TEM pictures of the 12 nm sized nanocrystals with 5 at% doping concentration

Figure 50 shows detailed TEM pictures for the first sample of the size series.

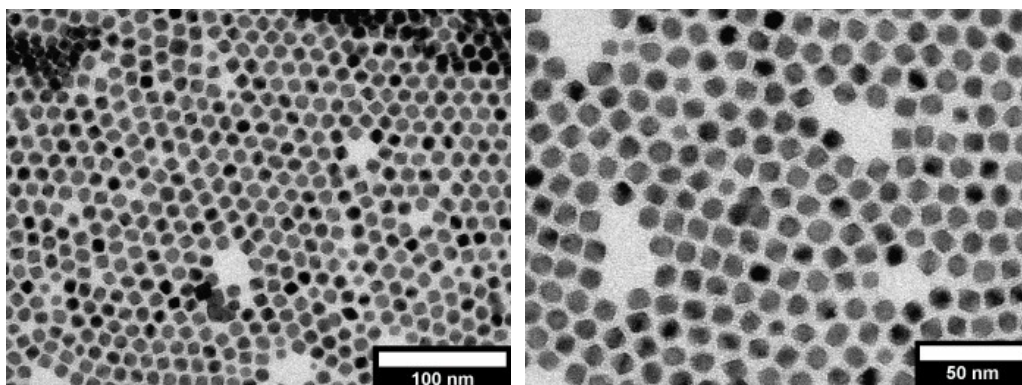


Figure 50: TEM pictures of the 13 nm sized nanocrystals with 5 at% doping concentration



Figure 51 shows detailed TEM pictures for the first sample of the size series.

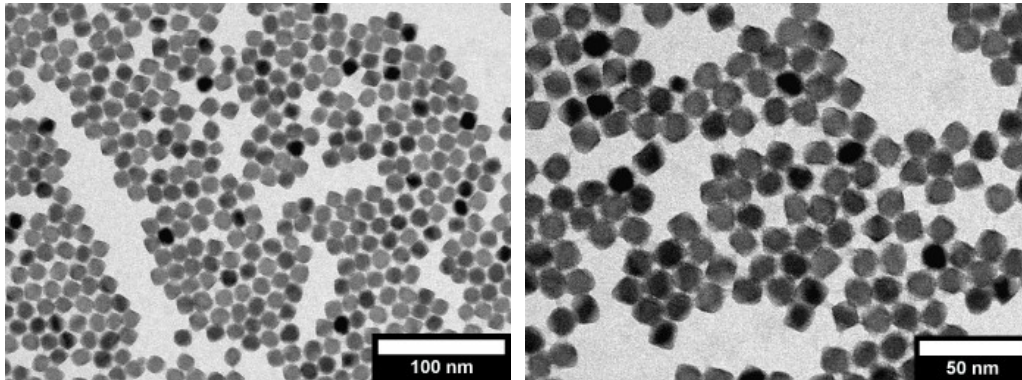


Figure 51: TEM pictures of the 16 nm sized nanocrystals with 5 at% doping concentration

Figure 52 shows detailed TEM pictures for the first sample of the size series.

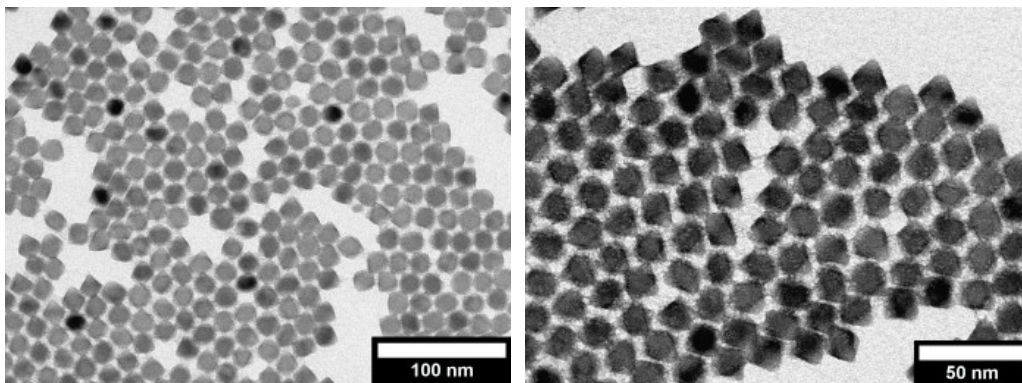


Figure 52: TEM pictures of the 19 nm sized nanocrystals with 5 at% doping concentration

Figure 53 shows detailed TEM pictures for the first sample of the size series.

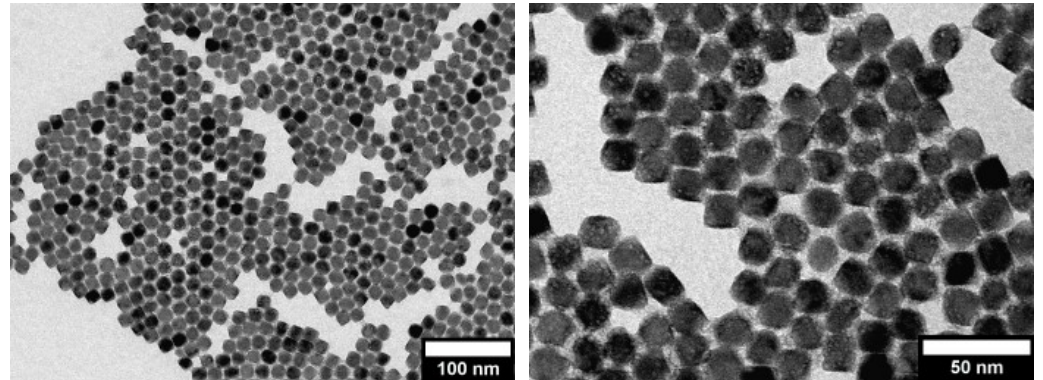


Figure 53: TEM pictures of the 21 nm sized nanocrystals with 5 at% doping concentration

## 15.2 ELEMENT MAPPING AND LINESCANS

Figure 54 exemplarily shows the element mapping of the 1.05 at% doped nanocrystals with 10 nm size and one 5 at% doped sample resulting from the EDX analysis. The mapping shows Fluorine, Yttrium, and Praseodymium inside the nanocrystals. Note, that the section for the 1.05 at% doped nanocrystals is much smaller than for the 5 at% doped nanocrystals which distorts the impression of the real Praseodymium doping concentration in the mapping pictures.

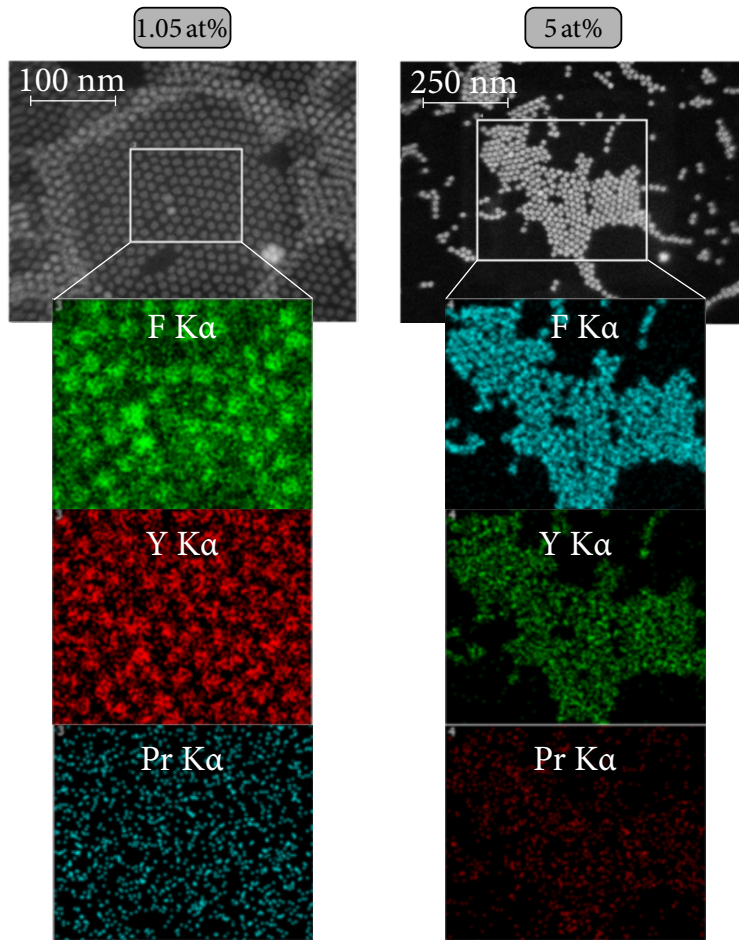


Figure 54: Mapping

Figure 55 shows an exemplary linescan over 75 nm of 5 to 6 nanocrystals doped with 1.47 at% that reveals a high resolution information about the Fluorine, Yttrium, and Praseodymium content in the nanocrystals. Such linescan is obtained by recording an EDX spectrum across a chosen line (indicated yellow in Figure 55. While the Fluorine and Yttrium lines clearly indicate the presence of the nanocrystal in the scanned line the Praseodymium line is less clear. This is due to the fact that the nanocrystals used for this linescan exhibit an average of only 37 ions per nanocrystal. The resolution of the used EDX seems to reach a limit at such low ion density.

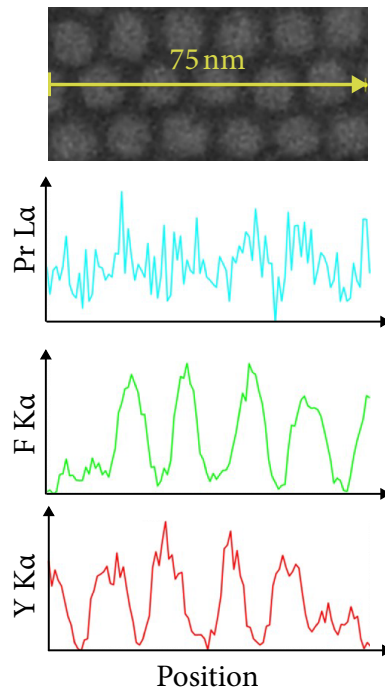


Figure 55: Mapping

## LIFETIME FITTING RESULTS

Figure 56 shows the fitting result for the  $^3P_0$  lifetime measurement of the concentration series.

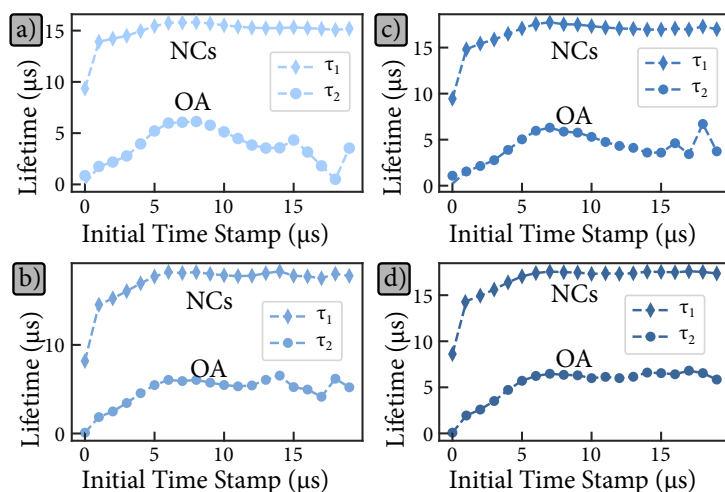


Figure 56: Dependence of the fit result of the  $^3P_0$  excited state lifetimes for the concentration series of LiYF<sub>4</sub>:Pr<sup>3+</sup> nanoparticles on the initial time stamp. a) 0.7 at%, b) 1.05 at%, c) 1.14 at%, d) 1.47 at%.

Figure 57 shows the fitting result for the  $^1D_2$  lifetime measurement of the concentration series.

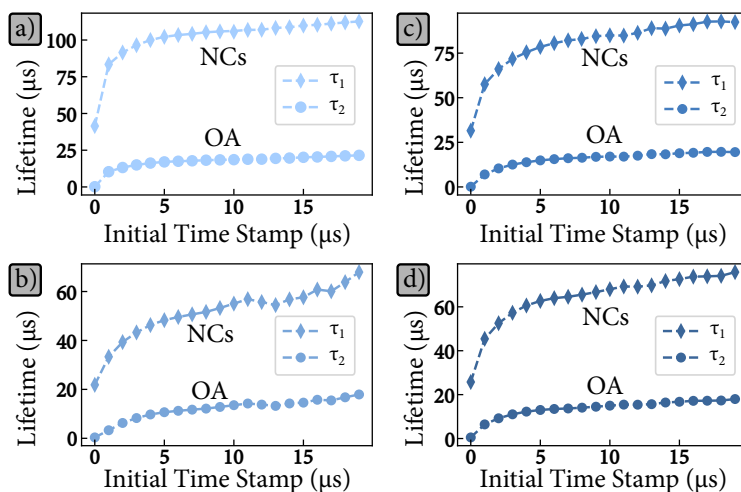


Figure 57: Dependence of the fit result of the  $^1D_2$  excited state lifetimes for the concentration series of LiYF<sub>4</sub>:Pr<sup>3+</sup> nanoparticles on the initial time stamp. a) 0.7 at%, b) 1.05 at%, c) 1.14 at%, d) 1.47 at%.

Figure 58 shows the fitting result for the  $^3P_0$  lifetime measurement of the size series.

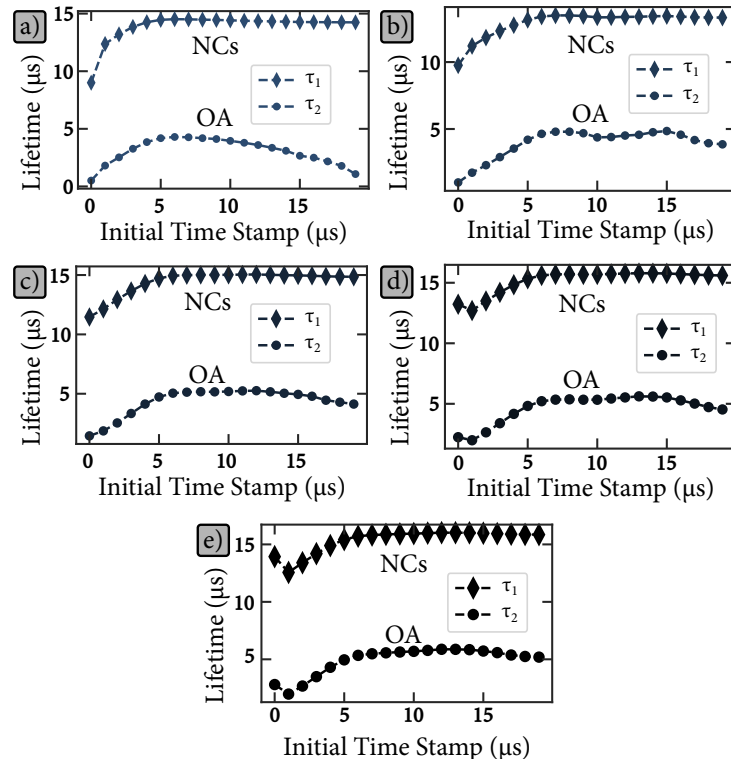


Figure 58: Dependence of the fit result of the  $^3P_0$  excited state lifetimes for the size series of  $\text{LiYF}_4:\text{Pr}^{3+}$  nanoparticles on the initial time stamp. a) 12 nm, b) 13 nm, 16 nm, 19 nm, 21 nm.

Figure 59 shows the fitting result for the  $^1D_2$  lifetime measurement of the concentration series.

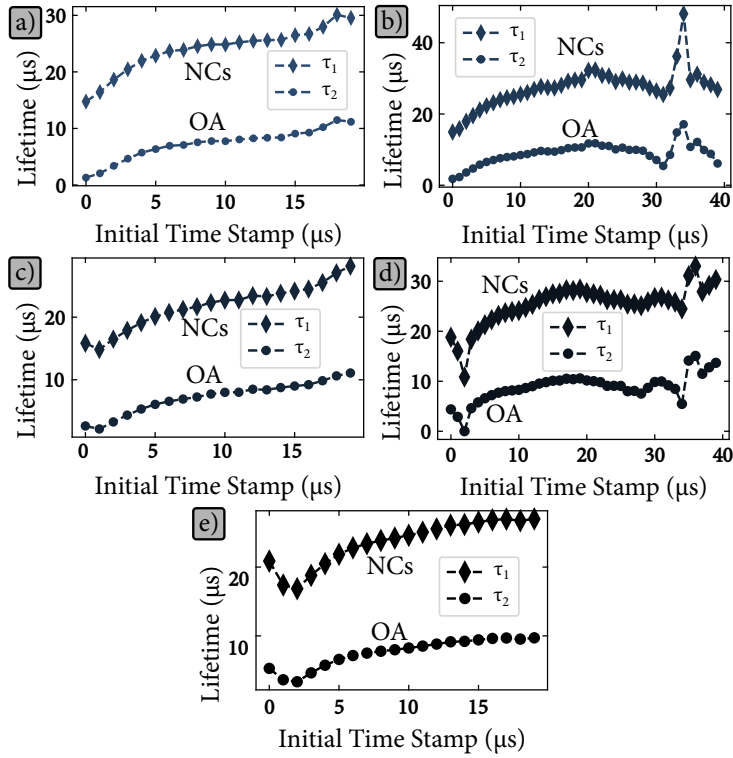


Figure 59: Dependence of the fit result of the  $^1D_2$  excited state lifetimes for the size series of  $\text{LiYF}_4:\text{Pr}^{3+}$  nanoparticles on the initial time stamp. a) 12 nm, b) 13 nm, 16 nm, 19 nm, 21 nm.





## PROCESS STATISTICS RESULTS

## Contents

17.1 Core-Only Nanocrystals . . . . .	117
17.2 Core-Shell Nanocrystals with 6 nm shell thickness	122

This part of the appendix provides the individual process statistics of the core-only nanocrystals (Section [Section 17.1](#)) and core-shell nanocrystals (Section [Section 17.2](#))

## 17.1 CORE-ONLY NANOCRYSTALS

[Figure 60](#) shows the process statistics for the 0.7 at% doped nanocrystals.

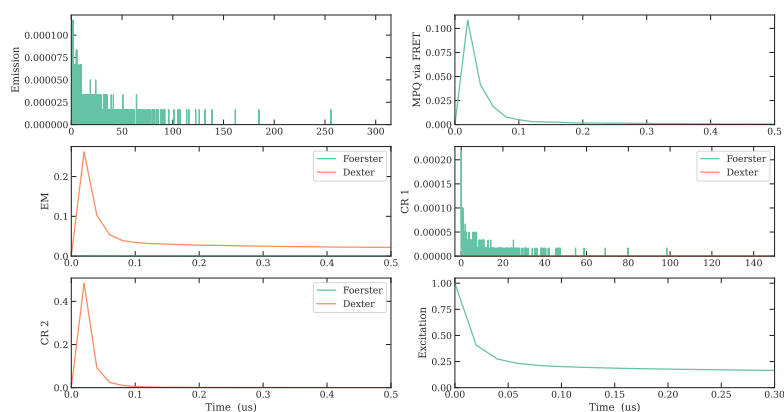


Figure 60: Process statistics of 0.7 at% doped  $\text{LiYF}_4:\text{Pr}^{3+}$  nanoparticles.

Figure 61 shows the process statistics for the 1.05 at% doped nanocrystals.

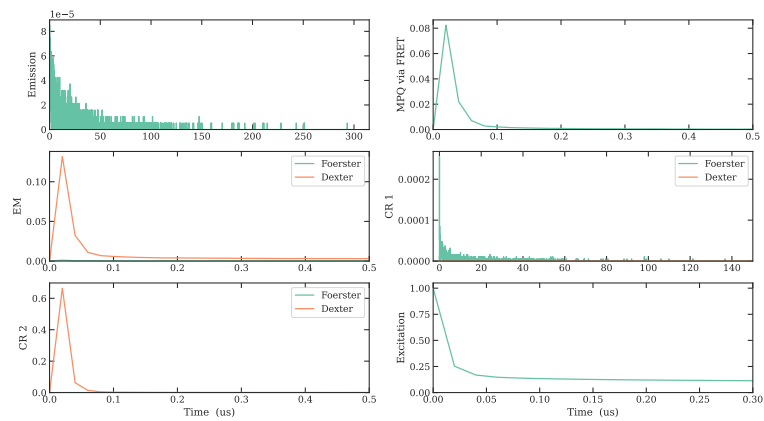


Figure 61: Process statistics of 1.05 at% doped  $\text{LiYF}_4:\text{Pr}^{3+}$  nanoparticles.

Figure 62 shows the process statistics for the 1.14 at% doped nanocrystals.

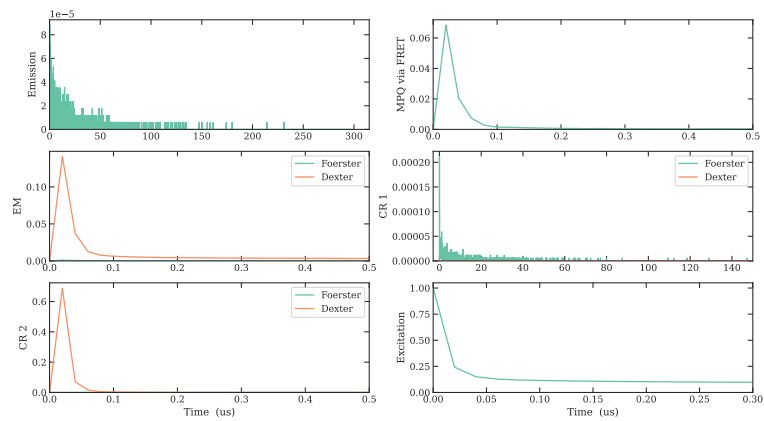


Figure 62: Process statistics of 1.14 at% doped  $\text{LiYF}_4:\text{Pr}^{3+}$  nanoparticles.

Figure 63 shows the process statistics for the 1.47 at% doped nanocrystals.

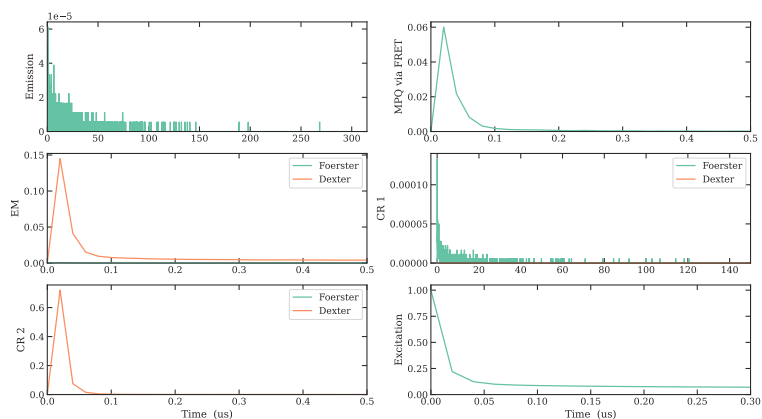


Figure 63: Process statistics of 1.47 at% doped  $\text{LiYF}_4:\text{Pr}^{3+}$  nanoparticles.

Figure 64 shows the process statistics for the 5 at% doped and 12 nm sized nanocrystals.

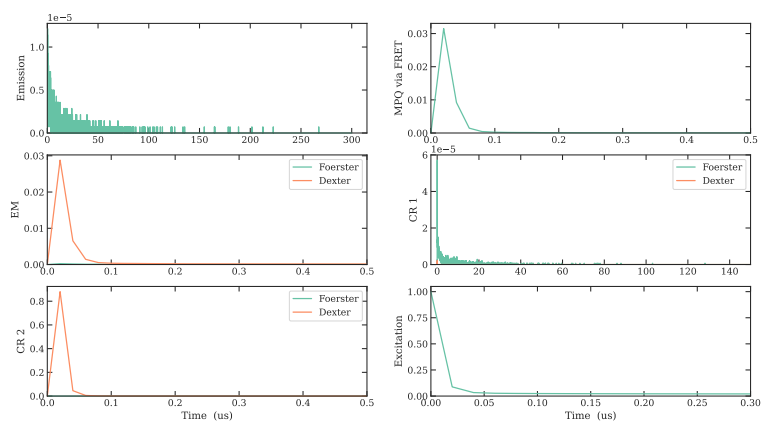


Figure 64: Process statistics of  $\approx 5$  at% doped  $\text{LiYF}_4:\text{Pr}^{3+}$  nanoparticles with 12 nm size.

Figure 65 shows the process statistics for the 5 at% doped and 13 nm sized nanocrystals.

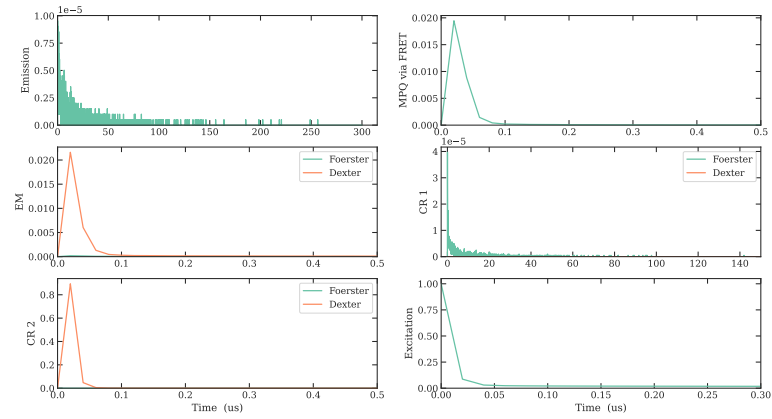


Figure 65: Process statistics of  $\approx 5$  at% doped  $\text{LiYF}_4:\text{Pr}^{3+}$  nanoparticles with 13 nm size.

Figure 66 shows the process statistics for the 5 at% doped and 16 nm sized nanocrystals.

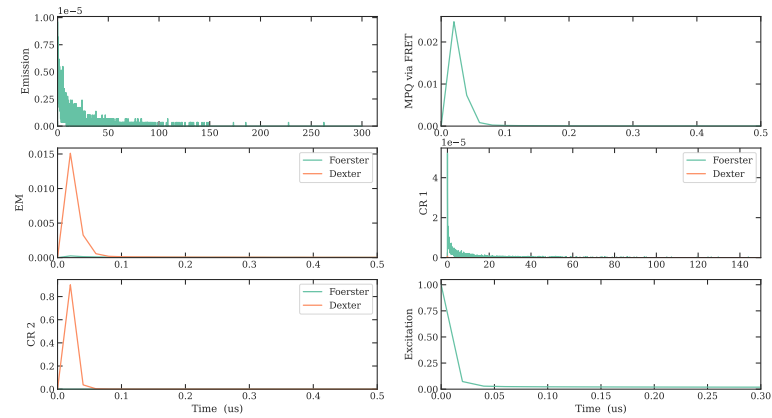


Figure 66: Process statistics of  $\approx 5$  at% doped  $\text{LiYF}_4:\text{Pr}^{3+}$  nanoparticles with 16 nm size.

Figure 67 shows the process statistics for the 5 at% doped and 19 nm sized nanocrystals.

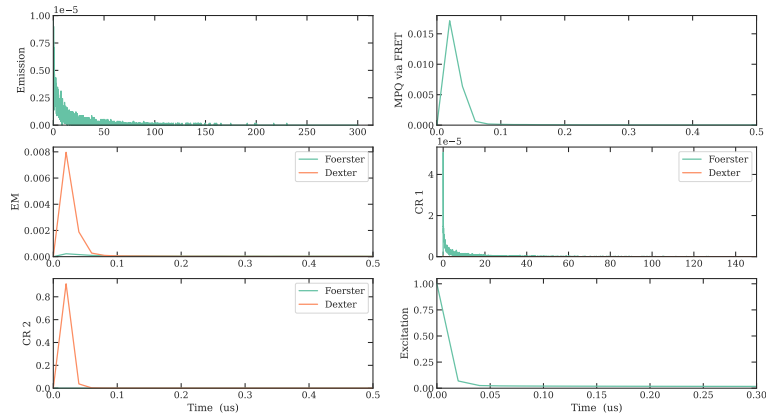


Figure 67: Process statistics of  $\approx 5$  at% doped LiYF<sub>4</sub>:Pr<sup>3+</sup> nanoparticles with 19 nm size.

Figure 68 shows the process statistics for the 5 at% doped and 21 nm sized nanocrystals.

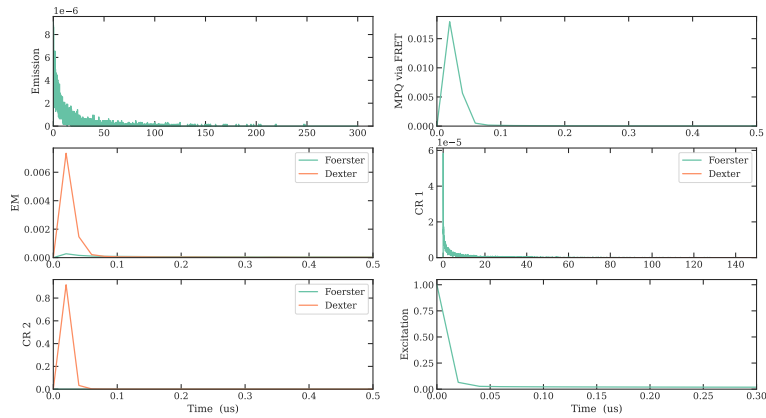


Figure 68: Process statistics of  $\approx 5$  at% doped LiYF<sub>4</sub>:Pr<sup>3+</sup> nanoparticles with 21 nm size.

## 17.2 CORE-SHELL NANOCRYSTALS WITH 6 NM SHELL THICKNESS

Figure 69 shows the process statistics for the 0.7 at% doped core-shell nanocrystals.

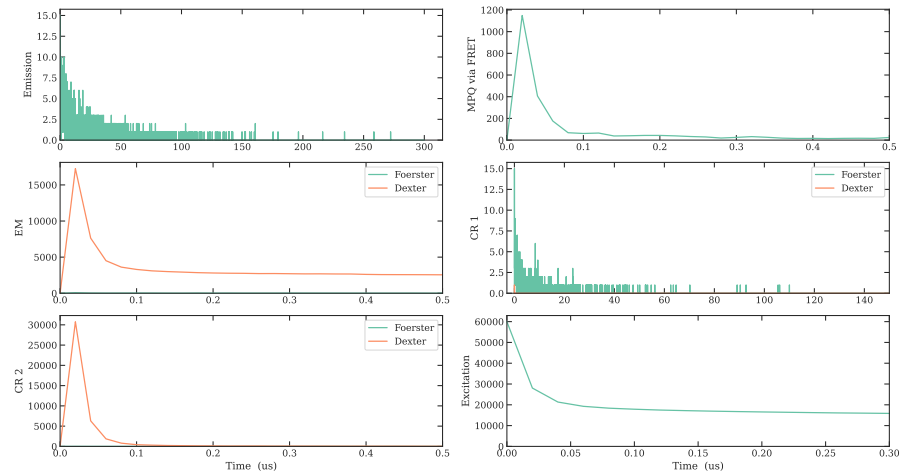


Figure 69: Process statistics of 0.7 at% doped  $\text{LiYF}_4:\text{Pr}^{3+}$  nanoparticles with a shell of 6 nm thickness.

Figure 70 shows the process statistics for the 1.05 at% doped core-shell nanocrystals.

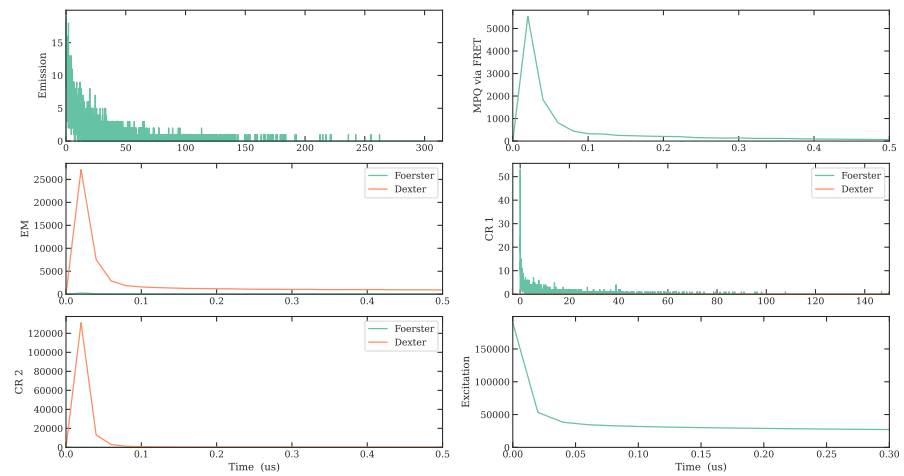


Figure 70: Process statistics of 1.05 at% doped  $\text{LiYF}_4:\text{Pr}^{3+}$  nanoparticles with a shell of 6 nm thickness.

Figure 71 shows the process statistics for the 1.14 at% doped core-shell nanocrystals.

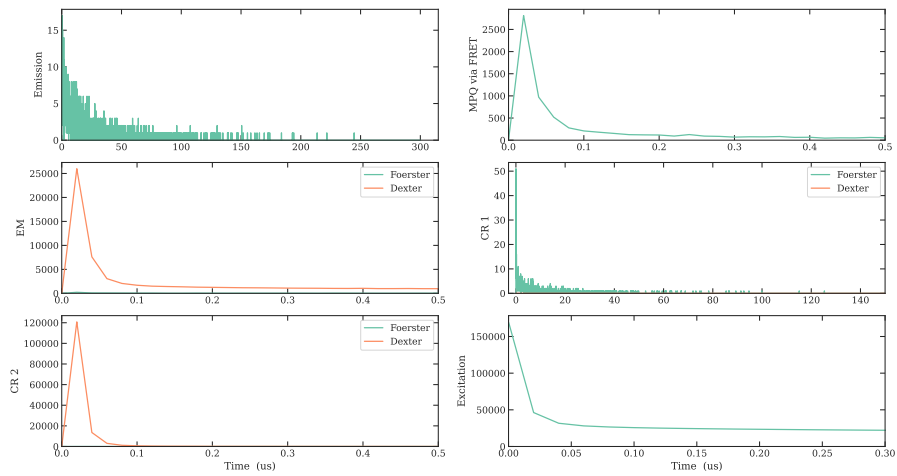


Figure 71: Process statistics of 1.14 at% doped  $\text{LiYF}_4:\text{Pr}^{3+}$  nanoparticles with a shell of 6 nm thickness.

Figure 72 shows the process statistics for the 1.47 at% doped core-shell nanocrystals.

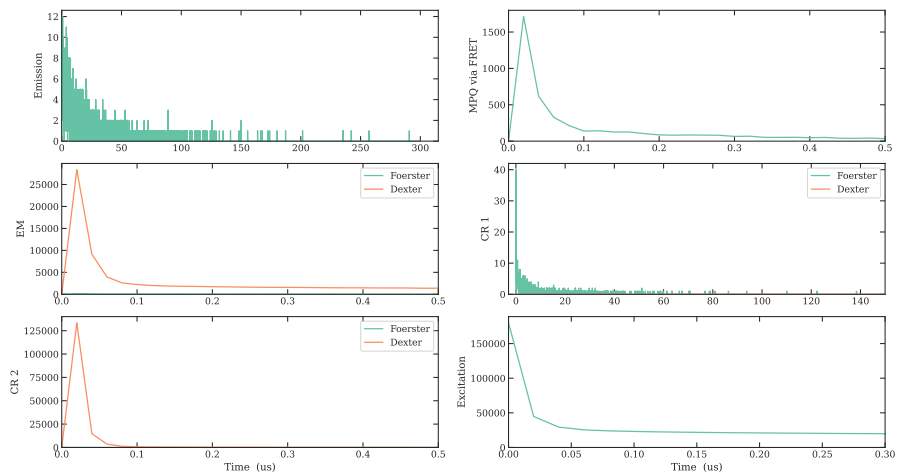


Figure 72: Process statistics of 1.47 at% doped  $\text{LiYF}_4:\text{Pr}^{3+}$  nanoparticles with a shell of 6 nm thickness.

Figure 77 shows the process statistics for the 5 at% doped and 12 nm sized core-shell nanocrystals.

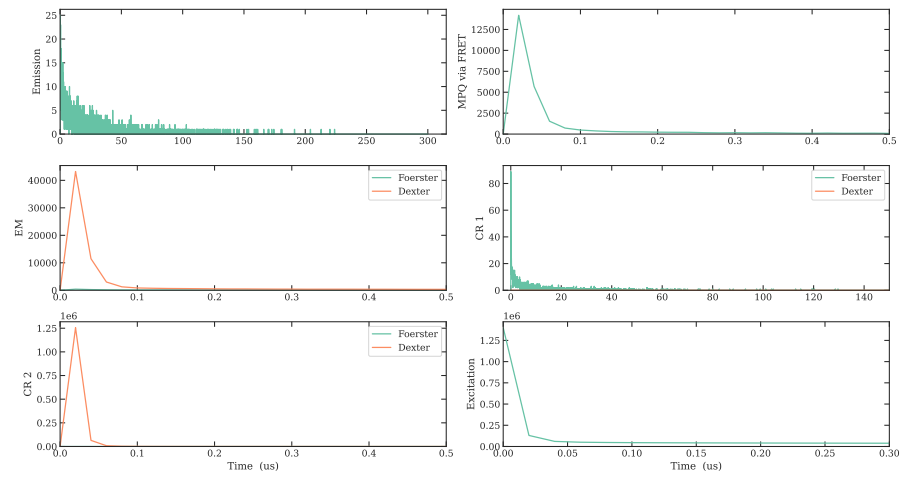


Figure 73: Process statistics of  $\approx 5$  at% doped  $\text{LiYF}_4:\text{Pr}^{3+}$  nanoparticles with 12 nm size and a shell thickness of 6 nm.

Figure 74 shows the process statistics for the 5 at% doped and 13 nm sized core-shell nanocrystals.

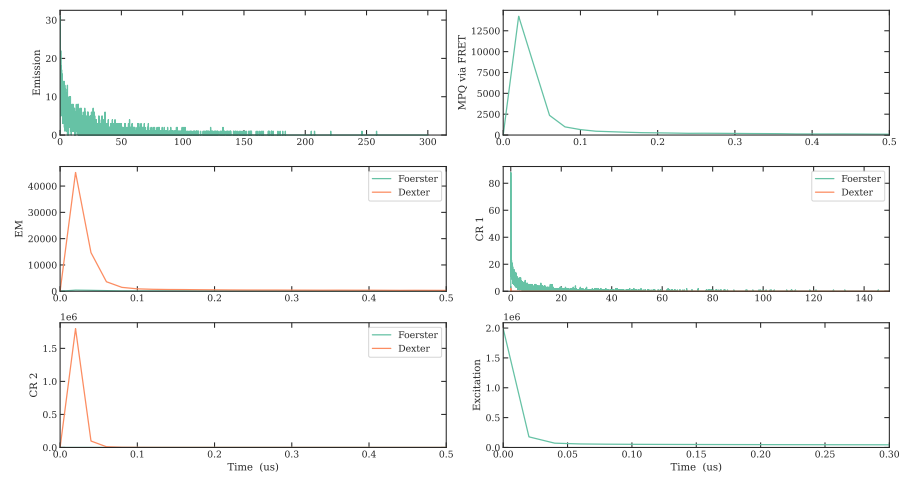


Figure 74: Process statistics of  $\approx 5$  at% doped  $\text{LiYF}_4:\text{Pr}^{3+}$  nanoparticles with 13 nm size and a shell thickness of 6 nm.



Figure 75 shows the process statistics for the 5 at% doped and 16 nm sized core-shell nanocrystals.

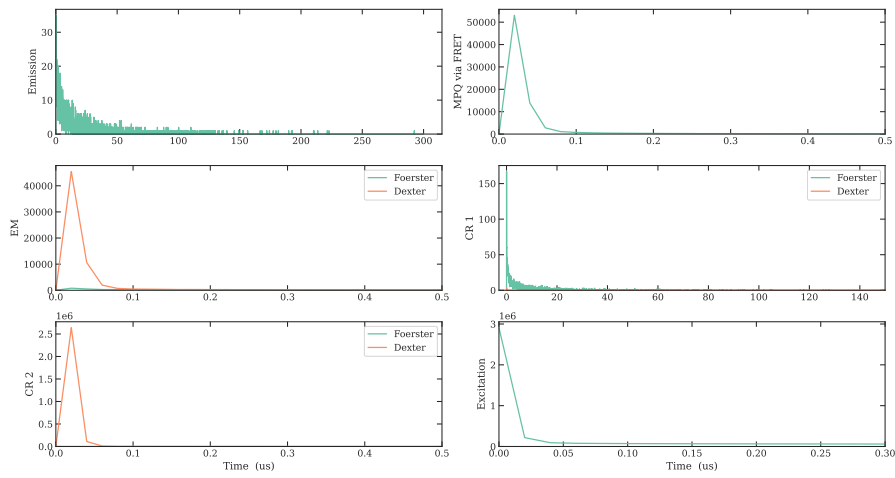


Figure 75: Process statistics of  $\approx 5$  at% doped  $\text{LiYF}_4:\text{Pr}^{3+}$  nanoparticles with 16 nm size and a shell thickness of 6 nm.

Figure 76 shows the process statistics for the 5 at% doped and 19 nm sized core-shell nanocrystals.

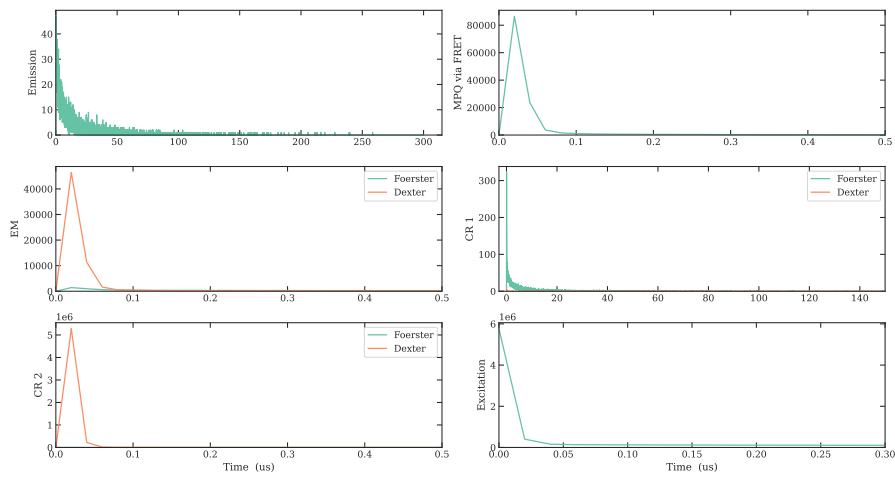


Figure 76: Process statistics of  $\approx 5$  at% doped  $\text{LiYF}_4:\text{Pr}^{3+}$  nanoparticles with 19 nm size and a shell thickness of 6 nm.

Figure 77 shows the process statistics for the 5 at% doped and 21 nm sized core-shell nanocrystals.

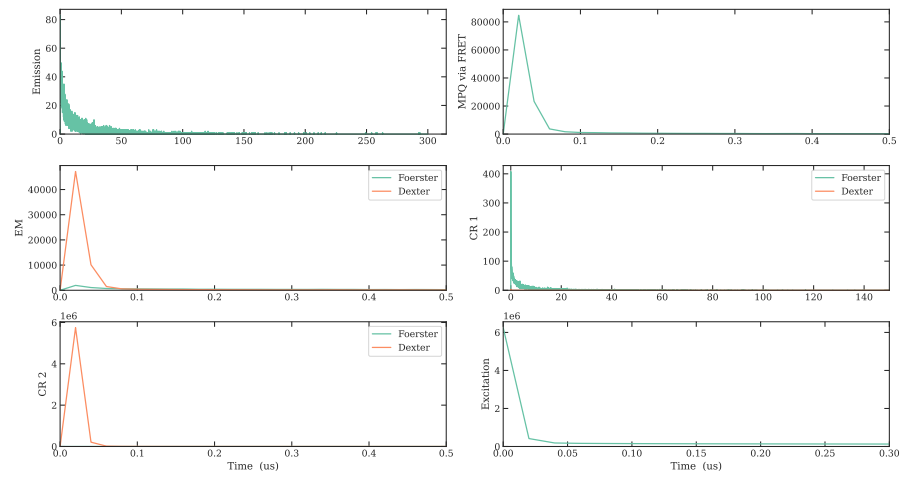


Figure 77: Process statistics of  $\approx 5$  at% doped LiYF<sub>4</sub>:Pr<sup>3+</sup> nanoparticles with 21 nm size and a shell thickness of 6 nm.

## ADDITIONAL SIMULATION PARAMETERS

---

Apart from the parameters mentioned in the main text of this work, the parameters summarized in [Table 3](#) were used in the numerical simulations,

PARAMETER	VALUE	UNIT
Single Ion Lifetime	~ 50	$\mu\text{s}$
Local field corrected lifetime	48.35	$\mu\text{s}$
Refractive Index $\text{LiYF}_4$	1.4526	
Refractive Index Toluene	1.4969	
Effective Bohr radius	1.8	$\text{\AA}$

Table 3: Summary of the parameters used in the simulation. Parameters that are not stated in this table are to be found in the main text of the paper.



## BIBLIOGRAPHY

---

- [1] Mark Lundstrom. "Moore's Law Forever?" In: *Science* 299.5604 (2003), pp. 210–211. DOI: [10.1126/science.1079567](https://doi.org/10.1126/science.1079567).
- [2] Reinhart Poprawe. "Photonics in the 21<sup>st</sup> Century – The European Technology Platform photonics21." In: *International Congress on Applications of Lasers & Electro-Optics 2007.1* (2007), p. 11. DOI: [10.2351/1.5060994](https://doi.org/10.2351/1.5060994).
- [3] Oratio Svelto and David C. Hanna. *Principles of Lasers*. Plenum Press, 1998.
- [4] Xian Qin, Xiaowang Liu, Wei Huang, Marco Bettinelli, and Xiaogang Liu. "Lanthanide-Activated Phosphors Based on 4f-5d Optical Transitions: Theoretical and Experimental Aspects." In: *Chemical Reviews* 117.5 (2017), pp. 4488–4527. DOI: [10.1021/acs.chemrev.6b00691](https://doi.org/10.1021/acs.chemrev.6b00691).
- [5] Tian Zhong and Philippe Goldner. "Emerging rare-earth doped material platforms for quantum nanophotonics." In: *Nanophotonics* 8.11 (2019), pp. 2003–2015. DOI: [doi : 10.1515/nanoph-2019-0185](https://doi.org/10.1515/nanoph-2019-0185).
- [6] M. Steinke, S. Spelthann, A. Rühl, and D. Ristau. "Absorption and multi-phonon quenching in nanocrystal doped SiO<sub>2</sub> fibers." In: *Optical Materials Express* 11.6 (2021), p. 1631. DOI: [10.1364/ome.424116](https://doi.org/10.1364/ome.424116).
- [7] A. Richter, E. Heumann, E. Osiac, G. Huber, W. Seelert, and A. Dening. "Diode pumping of a continuous-wave Pr<sup>3+</sup>-doped LiYF<sub>4</sub> laser." In: *Opt. Lett.* 29.22 (2004), pp. 2638–2640. DOI: [10.1364/OL.29.002638](https://doi.org/10.1364/OL.29.002638).
- [8] A. Richter, E. Heumann, G. Huber, V. Ostroumov, and W. Seelert. "Power scaling of semiconductor laser pumped Praseodymium-lasers." In: *Opt. Express* 15.8 (2007), pp. 5172–5178. DOI: [10.1364/OE.15.005172](https://doi.org/10.1364/OE.15.005172).
- [9] Nils-Owe Hansen, Aude-Reine Bellancourt, Ulrich Weichmann, and Günter Huber. "Efficient green continuous-wave lasing of blue-diode-pumped solid-state lasers based on praseodymium-doped LiYF<sub>4</sub>." In: *Appl. Opt.* 49.20 (2010), pp. 3864–3868. DOI: [10.1364/AO.49.003864](https://doi.org/10.1364/AO.49.003864).
- [10] Philip Werner Metz, Fabian Reichert, Francesca Moglia, Sebastian Müller, Daniel-Timo Marzahl, Christian Kränkel, and Günter Huber. "High-power red, orange, and green Pr<sup>3+</sup>:LiYF<sub>4</sub> lasers." In: *Opt. Lett.* 39.11 (June 2014), pp. 3193–3196. DOI: [10.1364/OL.39.003193](https://doi.org/10.1364/OL.39.003193).

- [11] C. Kränkel, D.-T. Marzahl, F. Moglia, G. Huber, and P. W. Metz. "Out of the blue: semiconductor laser pumped visible rare-earth doped lasers." In: *Laser & Photonics Reviews* 10.4 (2016), pp. 548–568. DOI: <https://doi.org/10.1002/lpor.201500290>.
- [12] Su Yeon Kim, Jong Seok Jeong, K. Andre Mkhoyan, and Ho Seong Jang. "Direct observation of the core/double-shell architecture of intense dual-mode luminescent tetragonal bipyramidal nanophosphors." In: *Nanoscale* 8 (19 2016), pp. 10049–10058. DOI: [10.1039/C5NR05722A](https://doi.org/10.1039/C5NR05722A).
- [13] Sara Espinoza, Max-Fabian Volhard, Heike Kätker, Heike Jenneboer, Anne Uckelmann, Markus Haase, Matthias Müller, Martin Purschke, and Thomas Jüstel. "Deep Ultraviolet Emitting Scintillators for Biomedical Applications: The Hard Way of Downsizing LuPO<sub>4</sub>:Pr<sup>3+</sup>." In: *Particle & Particle Systems Characterization* 35.12 (2018), p. 1800282. DOI: <https://doi.org/10.1002/ppsc.201800282>.
- [14] Benjamin Herden, Jörg Nordmann, R. Kompan, Markus Haase, and Thomas Jüstel. "Vacuum-UV excitation and visible luminescence of nano-scale and micro-scale NaLnF<sub>4</sub>:Pr<sup>3+</sup> (Ln=Y, Lu)." In: *Optical Materials* 35.12 (2013), pp. 2062–2067. DOI: <https://doi.org/10.1016/j.optmat.2013.05.020>.
- [15] Marek A. Gusowski, Hendrik C. Swart, Lisa S. Karlsson, and Monika Trzebiatowska-Gusowska. "NaYF<sub>4</sub>:Pr<sup>3+</sup> nanocrystals displaying photon cascade emission." In: *Nanoscale* 4 (2 2012), pp. 541–546. DOI: [10.1039/C1NR11249J](https://doi.org/10.1039/C1NR11249J).
- [16] T. Utikal, E. Eichhammer, L. Petersen, A. Renn, S. Götzinger, and V. Sandoghdar. "Spectroscopic detection and state preparation of a single praseodymium ion in a crystal." In: *Nature Communications* 5.1 (2014), p. 3627. DOI: [10.1038/ncomms4627](https://doi.org/10.1038/ncomms4627).
- [17] D. Rieländer, K. Kutluer, P. M. Ledingham, M. Gündogan, J. Fekete, M. Mazzera, and H. de Riedmatten. "Quantum Storage of Heralded Single Photons in a Praseodymium-Doped Crystal." In: *Phys. Rev. Lett.* 112 (4 2014), p. 040504. DOI: [10.1103/PhysRevLett.112.040504](https://doi.org/10.1103/PhysRevLett.112.040504).
- [18] Kangwei Xia, Roman Kolesov, Ya Wang, Petr Siyushev, Thomas Kornher, Rolf Reuter, Sen Yang, and Jörg Wrachtrup. "Spectroscopy properties of a single praseodymium ion in a crystal." In: *New Journal of Physics* 22.7 (2020), p. 073002. DOI: [10.1088/1367-2630/ab9555](https://doi.org/10.1088/1367-2630/ab9555).
- [19] R.M. Percival, M.W. Phillips, D.C. Hanna, and A.C. Tropper. "Characterization of spontaneous and stimulated emission from praseodymium (Pr<sup>3+</sup>) ions doped into a silica-based mono-mode optical fiber." In: *IEEE Journal of Quantum Electronics* 25.10 (1989), pp. 2119–2123. DOI: [10.1109/3.35724](https://doi.org/10.1109/3.35724).

- [20] S. Spelthann, S. Unland, J. Thiem, F. Jakobs, J. Kielhorn, P. Y. Ang, H.-H. Johannes, D. Kracht, J. Neumann, A. Ruehl, W. Kowalsky, and D. Ristau. "Towards Highly Efficient Polymer Fiber Laser Sources for Integrated Photonic Sensors." In: *Sensors* 20.15 (2020), p. 4086. DOI: [10.3390/s20154086](https://doi.org/10.3390/s20154086).
- [21] Esrom Kifle, Florent Starecki, Pavel Loiko, Solenn Cozic, Franck Joulain, Thibaud Berthelot, Thierry Georges, Dragan Stojcevski, Damien Deubel, and Patrice Camy. "Watt-level visible laser in double-clad Pr<sup>3+</sup>-doped fluoride fiber pumped by a GaN diode." In: *Opt. Lett.* 46.1 (Jan. 2021), pp. 74–77. DOI: [10.1364/OL.413673](https://doi.org/10.1364/OL.413673).
- [22] Mohammed Saad. "Fluoride glass fiber: state of the art." In: *Fiber Optic Sensors and Applications VI*. Ed. by Eric Udd, Henry H. Du, and Anbo Wang. Vol. 7316. International Society for Optics and Photonics. SPIE, 2009, 73160N. DOI: [10.1117/12.824112](https://doi.org/10.1117/12.824112).
- [23] Marie-Pier Lord, Frederic Maes, Vincent Fortin, Martin Bernier, and Real Vallee. "Watt-level visible laser emission in a double-clad praseodymium-doped fluoride fiber." In: *Laser Congress 2020 (ASSL, LAC)*. Optica Publishing Group, 2020, ATH5A.6. DOI: [10.1364/ASSL.2020.ATH5A.6](https://doi.org/10.1364/ASSL.2020.ATH5A.6).
- [24] A. E. Vasdekis, G. E. Town, G. A. Turnbull, and I. D. W. Samuel. "Fluidic fibre dye lasers." In: *Opt. Express* 15 (2007), pp. 3962–3967. DOI: [10.1364/OE.15.003962](https://doi.org/10.1364/OE.15.003962).
- [25] Christiano J. S. de Matos, Leonardo de S. Menezes, Antônio M. Brito-Silva, M. A. Martinez Gámez, Anderson S. L. Gomes, and Cid B. de Araújo. "Random Fiber Laser." In: *Phys. Rev. Lett.* 99 (15 2007), p. 153903. DOI: [10.1103/PhysRevLett.99.153903](https://doi.org/10.1103/PhysRevLett.99.153903).
- [26] Xi Yang, Chaoyang Gong, Chenlin Zhang, Yanqiong Wang, Guo-Feng Yan, Lei Wei, Yu-Cheng Chen, Yun-Jiang Rao, and Yuan Gong. "Fiber Optofluidic Microlasers: Structures, Characteristics, and Applications." In: *Laser & Photonics Reviews* 16.1 (2022), p. 2100171. DOI: <https://doi.org/10.1002/lpor.202100171>.
- [27] Alberto Sottile, Eugenio Damiano, Alberto Di Lieto, and Mauro Tonelli. "Diode-pumped solid-state laser platform for compact and long-lasting strontium-based optical clocks." In: *Opt. Lett.* 44.3 (2019), pp. 594–597. DOI: [10.1364/OL.44.000594](https://doi.org/10.1364/OL.44.000594).
- [28] Himani Siva Prasad, Frank Brueckner, Joerg Volpp, and Alexander F. H. Kaplan. "Laser metal deposition of copper on diverse metals using green laser sources." In: *The International Journal of Advanced Manufacturing Technology* 107.3 (2020), pp. 1559–1568. DOI: [10.1007/s00170-020-05117-z](https://doi.org/10.1007/s00170-020-05117-z).

- [29] M. Jansen, G. P. Carey, R. Carico, R. Dato, A. M. Earman, M. J. Finander, G. Giaretta, S. Hallstein, H. Hofler, C. P. Kocot, S. Lim, J. Krueger, A. Mooradian, G. Niven, Y. Okuno, F. G. Patterson, A. Tandon, and A. Umbrasas. "Visible laser sources for projection displays." In: *Projection Displays XII*. Ed. by Ming H. Wu and Hoang Y. Lin. Vol. 6489. International Society for Optics and Photonics. SPIE, 2007, p. 648908. DOI: [10.1117/12.716285](https://doi.org/10.1117/12.716285).
- [30] Richard P. Feynman. "There's plenty of room at the bottom [data storage]." In: *Journal of Microelectromechanical Systems* 1.1 (1992), pp. 60–66. DOI: [10.1109/84.128057](https://doi.org/10.1109/84.128057).
- [31] Xiaomin Li, Fan Zhang, and Dongyuan Zhao. "Lab on upconversion Nanoparticles: optical properties and applications engineering via designed nanostructure." In: *Chem. Soc. Rev.* 44 (6 2015), pp. 1346–1378. DOI: [10.1039/C4CS00163J](https://doi.org/10.1039/C4CS00163J).
- [32] H.-L. Wei, W. Zheng, X. Zhang, H. Suo, B. Chen, Y. Wang, and F. Wang. "Tuning Near-Infrared-to-Ultraviolet Upconversion in Lanthanide-Doped Nanoparticles for Biomedical Applications." In: *Advanced Optical Materials* (2022), p. 2201716. DOI: <https://doi.org/10.1002/adom.202201716>.
- [33] M. Zhao, A. Sik, H.n Zhang, and F. Zhang. "Tailored NIR-II Lanthanide Luminescent Nanocrystals for Improved Biomedical Application." In: *Advanced Optical Materials* (2022), p. 2202039. DOI: <https://doi.org/10.1002/adom.202202039>.
- [34] Christian Würth, Stefan Fischer, Bettina Grauel, A. Paul Alivisatos, and Ute Resch-Genger. "Quantum Yields, Surface Quenching, and Passivation Efficiency for Ultrasmall Core/Shell Upconverting Nanoparticles." In: *Journal of the American Chemical Society* 140.14 (2018), pp. 4922–4928. DOI: [10.1021/jacs.8b01458](https://doi.org/10.1021/jacs.8b01458).
- [35] S. Fischer, R. D. Mehlenbacher, A. Lay, C. Siefe, A. P. Alivisatos, and J. A. Dionne. "Small Alkaline-Earth-based Core/Shell Nanoparticles for Efficient Upconversion." In: *Nano Letters* 19.6 (2019), pp. 3878–3885. DOI: [10.1021/acs.nanolett.9b01057](https://doi.org/10.1021/acs.nanolett.9b01057).
- [36] J. C. Goldschmidt and S. Fischer. "Upconversion for Photovoltaics – a Review of Materials, Devices and Concepts for Performance Enhancement." In: *Advanced Optical Materials* 3.4 (2015), pp. 510–535. DOI: [10.1002/adom.201500024](https://doi.org/10.1002/adom.201500024).
- [37] S. Spelthann, L. F. Klepzig, D. H. Chau, M. Chemnitz, S. Ju-naid, R. Stephan, K. Hausmann, M. Schmidt, J. Lauth, M. Steinke, and D. Ristau. "Optical emission characterization of liquid core fibers filled with colloidal nanoplatelets." In: *10th EPS-QEOD Europhoton Conference on Solid-State, Fibre, and Waveguide Coherent Light Sources (EUROPHOTON 2022)*. 2022.



- [38] S. Spelthann, D. H. Chau, L. F. Klepzig, D. A. Rudoph, M. Chemnitz, S. Junaid, D. Ristau, M. A. Schmidt, J. Lauth, and M. Steinke. "Microfluidic Filling and Spectroscopy of Colloidal CdSe/CdS Nanoplatelets in Silica Capillary Fibers." In: *Submitted to Optics Letters*. (2023). DOI: <https://doi.org/10.48550/arXiv.2303.09624>.
- [39] Fiorenzo Vetrone, Rafik Naccache, Alicia Zamarrón, Angeles Juarranz de la Fuente, Francisco Sanz-Rodríguez, Laura Martínez Maestro, Emma Martín Rodríguez, Daniel Jaque, José García Solé, and John A. Capobianco. "Temperature Sensing Using Fluorescent Nanothermometers." In: *ACS Nano* 4.6 (2010), pp. 3254–3258. DOI: [10.1021/nn100244a](https://doi.org/10.1021/nn100244a).
- [40] J. Thiem, S. Spelthann, L. Neumann, F. Jakobs, H.-H. Johannes, W. Kowalsky, D. Kracht, J. Neumann, A. Ruehl, and D. Ristau. "Upconversion Nanocrystal Doped Polymer Fiber Thermometer." In: *Sensors* 20.21 (2020), p. 6048. DOI: [10.3390/s20216048](https://doi.org/10.3390/s20216048).
- [41] Ilya V. Fedotov, Maxim A. Solotnikov, Matvey S. Pochechuev, Olga I. Ivashkina, Sergei Ya. Kilin, Konstantin V. Anokhin, and Aleksei M. Zheltikov. "All-Optical Brain Thermometry in Freely Moving Animals." In: *ACS Photonics* 7.12 (2020), pp. 3353–3360. DOI: [10.1021/acsp Photonics.0c00706](https://doi.org/10.1021/acsp Photonics.0c00706).
- [42] Hanyang Li, Feng Wei, Yanzeng Li, Miao Yu, Yu Zhang, Lu Liu, and Zhihai Liu. "Optical fiber sensor based on upconversion nanoparticles for internal temperature monitoring of Li-ion batteries." In: *J. Mater. Chem. C* 9 (41 2021), pp. 14757–14765. DOI: [10.1039/D1TC03701C](https://doi.org/10.1039/D1TC03701C).
- [43] L. Koettters, S. Spelthann, L. Buehre, R. Kompan, H. Weller, R. Hanke-Rauschenbach, D. Ristau, C. Gimmler, B. Bensmann, and M. Steinke. "Fiber-tip nanothermometer based on up-conversion nanocrystals for electrolysis cells." In: *10th EPS-QEOD Europhoton Conference on Solid-State, Fibre, and Waveguide Coherent Light Sources (EUROPHOTON 2022)*. 2022.
- [44] J. Thiem, S. Spelthann, J. Neumann, A. Ruehl, and D. Ristau. "Three-dimensional nanothermometry below the diffraction limit." In: *Optics Letters* 46.14 (2021), p. 3352. DOI: [10.1364/ol.423626](https://doi.org/10.1364/ol.423626).
- [45] Frederike Carl, Leonie Birk, Bettina Grauel, Monica Pons, Christian Würth, Ute Resch-Genger, and Markus Haase. "LiYF<sub>4</sub>:Yb/-LiYF<sub>4</sub> and LiYF<sub>4</sub>:Yb,Er/LiYF<sub>4</sub> core/shell nanocrystals with luminescence decay times similar to YLF laser crystals and the upconversion quantum yield of the Yb,Er doped nanocrystals." In: *Nano Research* 14.3 (2021), pp. 797–806. DOI: [10.1007/s12274-020-3116-y](https://doi.org/10.1007/s12274-020-3116-y).

- [46] Jiayan Liao, Jiajia Zhou, Yiliao Song, Baolei Liu, Yinghui Chen, Fan Wang, Chao hao Chen, Jun Lin, Xueyuan Chen, Jie Lu, and Dayong Jin. "Preselectable Optical Fingerprints of Heterogeneous Upconversion Nanoparticles." In: *Nano Letters* 21.18 (2021), pp. 7659–7668. DOI: [10.1021/acs.nanolett.1c02404](https://doi.org/10.1021/acs.nanolett.1c02404).
- [47] Anthony E. Siegman. *Lasers*. University Science Books, 1986.
- [48] Magdalena Dudek, Marcin Szalkowski, Małgorzata Misiak, Maciej Ćwierzona, Artiom Skripka, Zuzanna Korczak, Dawid Piątkowski, Piotr Woźniak, Radosław Lisiecki, Philippe Goldner, Sebastian Maćkowski, Emory M. Chan, P. James Schuck, and Artur Bednarkiewicz. "Size-Dependent Photon Avalanching in  $\text{Tm}^{3+}$  Doped  $\text{LiYF}_4$  Nano, Micro, and Bulk Crystals." In: *Advanced Optical Materials* 10.19 (2022), p. 2201052. DOI: <https://doi.org/10.1002/adom.202201052>.
- [49] Stefan Fischer, Heiko Steinkemper, Philipp Löper, Martin Hermle, and Jan Christoph Goldschmidt. "Modeling upconversion of erbium doped microcrystals based on experimentally determined Einstein coefficients." In: *Journal of Applied Physics* 111.1 (2012), p. 013109. DOI: [10.1063/1.3674319](https://doi.org/10.1063/1.3674319).
- [50] Robert B. Anderson, Steve J. Smith, P. Stanley May, and Mary T. Berry. "Revisiting the NIR-to-Visible Upconversion Mechanism in  $\beta\text{-NaYF}_4\text{:Yb}^{3+},\text{Er}^{3+}$ ." In: *The Journal of Physical Chemistry Letters* 5.1 (2014), pp. 36–42. DOI: [10.1021/jz402366r](https://doi.org/10.1021/jz402366r).
- [51] Md Yeathad Hossan, Amy Hor, QuocAnh Luu, Steve J. Smith, P. Stanley May, and Mary T. Berry. "Explaining the Nanoscale Effect in the Upconversion Dynamics of  $\beta\text{-NaYF}_4\text{:Yb}^{3+},\text{Er}^{3+}$  Core and Core–Shell Nanocrystals." In: *The Journal of Physical Chemistry C* 121.30 (2017), pp. 16592–16606. DOI: [10.1021/acs.jpcc.7b04567](https://doi.org/10.1021/acs.jpcc.7b04567).
- [52] Gabriella Tessitore, Gabrielle A. Mandl, Mikhail G. Brik, Wounghang Park, and John A. Capobianco. "Recent insights into up-converting nanoparticles: spectroscopy, modeling, and routes to improved luminescence." In: *Nanoscale* 11 (25 2019), pp. 12015–12029. DOI: [10.1039/C9NR02291K](https://doi.org/10.1039/C9NR02291K).
- [53] Jan W. Stouwdam, Gerald A. Hebbink, Jurriaan Huskens, and Frank C. J. M. van Veggel. "Lanthanide-Doped Nanoparticles with Excellent Luminescent Properties in Organic Media." In: *Chemistry of Materials* 15.24 (2003), pp. 4604–4616. DOI: [10.1021/cm034495d](https://doi.org/10.1021/cm034495d).
- [54] S. Spelthann, R. Kompan, M. Steinke, D. Ristau, A. Ruehl, C. Gimmler, and H. Weller. "Bulk-like emission in the visible spectrum of colloidal  $\text{LiYF}_4\text{:Pr}$  nanocrystals downsized to 10 nm." In: *Nanoscale Advances* 4.14 (Apr. 25, 2022), pp. 2973–2978. DOI: [10.1039/d2na00045h](https://doi.org/10.1039/d2na00045h).

- [55] Freddy T. Rabouw, P. Tim Prins, Pedro Villanueva-Delgado, Marieke Castelijns, Robin G. Geitenbeek, and Andries Meijerink. "Quenching Pathways in NaYF<sub>4</sub>:Er<sup>3+</sup>,Yb<sup>3+</sup> Upconversion Nanocrystals." In: *ACS Nano* 12.5 (2018), pp. 4812–4823. DOI: [10.1021/acsnano.8b01545](https://doi.org/10.1021/acsnano.8b01545).
- [56] Pedro Villanueva-Delgado, Karl W. Krämer, and Rafael Valiente. "Simulating Energy Transfer and Upconversion in β-NaYF<sub>4</sub>:Yb<sup>3+</sup>,Tm<sup>3+</sup>." In: *The Journal of Physical Chemistry C* 119.41 (2015), pp. 23648–23657. DOI: [10.1021/acs.jpcc.5b06770](https://doi.org/10.1021/acs.jpcc.5b06770).
- [57] Pedro Villanueva-Delgado, Karl W. Krämer, Rafael Valiente, Mathijs de Jong, and Andries Meijerink. "Modeling blue to UV upconversion in β-NaYF<sub>4</sub>:Tm<sup>3+</sup>." In: *Phys. Chem. Chem. Phys.* 18 (39 2016), pp. 27396–27404. DOI: [10.1039/C6CP04347J](https://doi.org/10.1039/C6CP04347J).
- [58] Federico Pini, Laura Francés-Soriano, Nicola Peruffo, Antonio Barbon, Niko Hildebrandt, and Marta Maria Natile. "Spatial and Temporal Resolution of Luminescence Quenching in Small Upconversion Nanocrystals." In: *ACS Applied Materials & Interfaces* 14.9 (2022), pp. 11883–11894. DOI: [10.1021/acsmi.1c23498](https://doi.org/10.1021/acsmi.1c23498).
- [59] Changhwan Lee, Emma Z. Xu, Yawei Liu, Ayelet Teitelboim, Kaiyuan Yao, Angel Fernandez-Bravo, Agata M. Kotulska, Sang Hwan Nam, Yung Doug Suh, Artur Bednarkiewicz, Bruce E. Cohen, Emory M. Chan, and P. James Schuck. "Giant nonlinear optical responses from photon-avalanching nanoparticles." In: *Nature* 589.7841 (2021), pp. 230–235. DOI: [10.1038/s41586-020-03092-9](https://doi.org/10.1038/s41586-020-03092-9).
- [60] Ting Cheng, Riccardo Marin, Artiom Skripka, and Fiorenzo Vetrone. "Small and Bright Lithium-Based Upconverting Nanoparticles." In: *Journal of the American Chemical Society* 140.40 (2018), pp. 12890–12899. DOI: [10.1021/jacs.8b07086](https://doi.org/10.1021/jacs.8b07086).
- [61] M. S. Pudovkin, S. L. Korableva, D. A. Koryakovtseva, E. V. Lukinova, A. V. Lovchev, O. A. Morozov, and V. V. Semashko. "The comparison of Pr<sup>3+</sup>:LaF<sub>3</sub> and Pr<sup>3+</sup>:LiYF<sub>4</sub> luminescent nano- and microthermometer performances." In: *Journal of Nanoparticle Research* 21.12 (2019), p. 266. DOI: [10.1007/s11051-019-4713-0](https://doi.org/10.1007/s11051-019-4713-0).
- [62] M. Pudovkin, S. Korableva, E. Lukinova, D. Koryakovtseva, O. Morozov, and V. Semashko. "The luminescence thermometry based on analysing of <sup>3</sup>P<sub>0</sub> – <sup>3</sup>H<sub>5</sub> emission band of Pr<sup>3+</sup> ions in Pr<sup>3+</sup>:LiYF<sub>4</sub> nanoparticles and microparticles." In: *EPJ Web of Conferences* 220 (2019), p. 02011. DOI: [10.1051/epjconf/201922002011](https://doi.org/10.1051/epjconf/201922002011).

- [63] Helmut Goesmann and Claus Feldmann. "Nanoparticulate Functional Materials." In: *Angewandte Chemie International Edition* 49.8 (2010), pp. 1362–1395. DOI: <https://doi.org/10.1002/anie.200903053>.
- [64] C. Wagner. "Theorie der Alterung von Niederschlägen durch Umlösen (Ostwald-Reifung)." In: *Zeitschrift für Elektrochemie, Berichte der Bunsengesellschaft für physikalische Chemie* 65.7-8 (1961), pp. 581–591. DOI: <https://doi.org/10.1002/bbpc.19610650704>.
- [65] D. V. Talapin, A. L. Rogach, M. Haase, and H. Weller. "Evolution of an Ensemble of Nanoparticles in a Colloidal Solution: Theoretical Study." In: *The Journal of Physical Chemistry B* 105.49 (2001), pp. 12278–12285. DOI: [10.1021/jp012229m](https://doi.org/10.1021/jp012229m).
- [66] Venkataramanan Mahalingam, Fiorenzo Vetrone, Rafik Nacache, Adolfo Speghini, and John A. Capobianco. "Colloidal Tm<sup>3+</sup>/Yb<sup>3+</sup>-Doped LiYF<sub>4</sub> Nanocrystals: Multiple Luminescence Spanning the UV to NIR Regions via Low-Energy Excitation." In: *Advanced Materials* 21.40 (2009), pp. 4025–4028. DOI: <https://doi.org/10.1002/adma.200901174>.
- [67] J. T. Mulder, M. S. Meijer, J. J. van Blaaderen, I. du Fossé, K. Jenkinson, S. Bals, L. Manna, and A. J. Houtepen. "Understanding and Preventing Photoluminescence Quenching to Achieve Unity Photoluminescence Quantum Yield in Yb:YLF Nanocrystals." In: *ACS Applied Materials & Interfaces* 15.2 (2023), pp. 3274–3286. DOI: [10.1021/acscami.2c17888](https://doi.org/10.1021/acscami.2c17888).
- [68] Renfu Li, Xiaodie Fang, Jilou Ren, Baojun Chen, Xiaoyun Yuan, Xuechun Pan, Peng Zhang, Lantian Zhang, Datao Tu, Zhenlan Fang, Xueyuan Chen, and Qiang Ju. "The effect of surface-capping oleic acid on the optical properties of lanthanide-doped nanocrystals." In: *Nanoscale* 13 (29 2021), pp. 12494–12504. DOI: [10.1039/D0NR08488C](https://doi.org/10.1039/D0NR08488C).
- [69] M Fibrich, J Šulc, and H Jelínková. "Pr:YLF orange laser investigation at cryogenic temperature." In: *Laser Physics Letters* 12.9 (July 2015), p. 095801. DOI: [10.1088/1612-2011/12/9/095801](https://doi.org/10.1088/1612-2011/12/9/095801).
- [70] Maxim Gaponenko, Philip Werner Metz, Antti Härkönen, Alexander Heuer, Tomi Leinonen, Mircea Guina, Thomas Südmeyer, Günter Huber, and Christian Kränkel. "SESAM mode-locked red praseodymium laser." In: *Opt. Lett.* 39.24 (2014), pp. 6939–6941. DOI: [10.1364/OL.39.006939](https://doi.org/10.1364/OL.39.006939).
- [71] Peng Wu, Bo Xiao, Qichen Feng, Xiuji Lin, Wensong Li, Huiying Xu, and Zhiping Cai. "Spectral analysis of new-wavelength transitions originated from <sup>1</sup>D<sub>2</sub> level of Pr:YLF crystal." In: *Journal of Luminescence* 235 (2021), p. 118028. ISSN: 0022-2313. DOI: <https://doi.org/10.1016/j.jlumin.2021.118028>.

- [72] Zhongyu Wang, Zhengdong Dai, Shuaihao Ji, Shuhua Huang, Bo Xiao, Zhibin He, Huiying Xu, and Zhiping Cai. "Spectral analysis of  $1G_4$  level in the  $\text{Pr}^{3+}:\text{YLF}$  crystal." In: *Journal of Luminescence* 247 (2022), p. 118870. ISSN: 0022-2313. DOI: <https://doi.org/10.1016/j.jlumin.2022.118870>.
- [73] L. Esterowitz, F. J. Bartoli, R. E. Allen, D. E. Wortman, C. A. Morrison, and R. P. Leavitt. "Energy levels and line intensities of  $\text{Pr}^{3+}$  in  $\text{LiYF}_4$ ." In: *Phys. Rev. B* 19 (12 1979), pp. 6442–6455. DOI: [10.1103/PhysRevB.19.6442](https://doi.org/10.1103/PhysRevB.19.6442).
- [74] Western Bolanos, Gurvan Brasse, Florent Starecki, Alain Braud, Jean-Louis Doualan, Richard Moncorge, and Patrice Camy. "Green, orange, and red  $\text{Pr}^{3+}:\text{LiYF}_4$  epitaxial waveguide lasers." In: *Opt. Lett.* 39.15 (Aug. 2014), pp. 4450–4453. DOI: [10.1364/OL.39.004450](https://doi.org/10.1364/OL.39.004450).
- [75] R. E. Thoma, C. F. Weaver, H. A. Friedman, H. Insley, L. A. Harris, and H. A. Jr. Yakel. "Phase Equilibria in the System  $\text{LiF}-\text{YF}_3$ ." In: *The Journal of Physical Chemistry* 65.7 (1961), pp. 1096–1099. DOI: [10.1021/j100825a003](https://doi.org/10.1021/j100825a003).
- [76] E. B. Sveshnikova, A. A. Stroganov, and N. T. Timofeev. "Role of quasilocizable vibrations in the deactivation of rare-earth ions in fluoride bases." In: *Optics and Spectroscopy* 64.1 (1988), pp. 43–46.
- [77] A. A. Kaminskii, H. J. Eichler, B. Liu, and P. Meindl. " $\text{LiYF}_4:\text{Pr}^{3+}$  laser at 639.5 nm with 30 J flashlamp pumping and 87 mJ output energy." In: *Physica Status Solidi (a)* 138.1 (1993).
- [78] X.X. Zhang, A. Schulte, and B.H.T. Chai. "Raman spectroscopic evidence for isomorphous structure of  $\text{GdLiF}_4$  and  $\text{YLiF}_4$  laser crystals." In: *Solid State Communications* 89.2 (1994), pp. 181–184. DOI: [https://doi.org/10.1016/0038-1098\(94\)90402-2](https://doi.org/10.1016/0038-1098(94)90402-2).
- [79] H. K. Kammler and L. Madler. "Characterization of Fine Dry Powders." In: *Chemical processing of ceramics* (2005), pp. 233–266.
- [80] Caroline A. Schneider, Wayne S. Rasband, and Kevin W. Eliceiri. "NIH Image to ImageJ: 25 years of image analysis." In: *Nature Methods* 9.7 (2012), pp. 671–675. DOI: [10.1038/nmeth.2089](https://doi.org/10.1038/nmeth.2089).
- [81] Brian Henderson and George F. Imbusch. *Optical Spectroscopy of Inorganic Solids*. Oxford Science Publications, 1989.
- [82] Guokui Liu and Bernard Jacquier. *Spectroscopic Properties of Rare Earths in Optical Materials*. Springer Berlin, 2005.
- [83] Vikas Dubey, Neha Dubey, Marta Michalska Domanska, M. Jayasimhadri, and Sanjay J Dhoble, eds. *Rare-earth-activated phosphors*. Elsevier - Health Sciences Division, 2022.

- [84] Felix Bussieres, C. Clausen, Alexey Tiranov, Boris Korzh, Varun B. Verma, Sae Woo Nam, Francesco Marsili, Alban Ferrier, Philippe Goldner, Harald Herrmann, Christine Silberhorn, Wolfgang Sohler, Mikael Afzelius, and Nicolas Gisin. "Quantum teleportation from a telecom-wavelength photon to a solid-state quantum memory." In: *Nature Photonics* 8.10 (2014), pp. 775–778. DOI: [10.1038/nphoton.2014.215](https://doi.org/10.1038/nphoton.2014.215).
- [85] Chr. Klixbüll Jorgensen, Romano Pappalardo, and Elfriede Rittershaus. "Reflection Spectra of Lanthanides in Thorium (IV) Oxide and the Large Nephelauxetic Effect of Oxide Ligands or Vacancies." In: *Zeitschrift für Naturforschung A* 19.4 (1964), pp. 424–433. DOI: [10.1515/zna-1964-0405](https://doi.org/10.1515/zna-1964-0405).
- [86] R Yu Shendrik, A S Myasnikova, A V Egranov, and E A Radzhabov. "Divalent cerium and praseodymium ions in crystals of alkaline-earth fluorides." In: *Optics and Spectroscopy* 116.5 (2014), pp. 777–782.
- [87] L.B. Asprey and T.K. Keenan. "Tetravalent Lanthanides—I Sodium Praseodymium(IV) Fluorides." In: *Journal of Inorganic and Nuclear Chemistry* 16.3 (1961), pp. 260–262. DOI: [https://doi.org/10.1016/0022-1902\(61\)80499-5](https://doi.org/10.1016/0022-1902(61)80499-5).
- [88] Qingnan Zhang, Shu-Xian Hu, Hui Qu, Jing Su, Guanjun Wang, Jun-Bo Lu, Mohua Chen, Mingfei Zhou, and Jun Li. "Pentavalent Lanthanide Compounds: Formation and Characterization of Praseodymium(V) Oxides." In: *Angewandte Chemie International Edition* 55.24 (2016), pp. 6896–6900. DOI: <https://doi.org/10.1002/anie.201602196>.
- [89] Eugene Loh. " $^1S_0$  Level of  $Pr^{3+}$  in Crystals of Fluorides." In: *Phys. Rev.* 140 (5A Nov. 1965), A1463–A1466. DOI: [10.1103/PhysRev.140.A1463](https://doi.org/10.1103/PhysRev.140.A1463). URL: <https://link.aps.org/doi/10.1103/PhysRev.140.A1463>.
- [90] Theodor Förster. "Zwischenmolekulare Energiewanderung und Fluoreszenz." In: *Annalen der Physik* 437 (1-2 Jan. 1948), pp. 55–75. DOI: [10.1002/andp.19484370105](https://doi.org/10.1002/andp.19484370105).
- [91] D. L. Dexter. "A Theory of Sensitized Luminescence in Solids." In: *The Journal of Chemical Physics* 21.5 (1953), pp. 836–850. DOI: [10.1063/1.1699044](https://doi.org/10.1063/1.1699044).
- [92] Joseph R Lakowicz. *Principles of fluorescence spectroscopy*. Springer, 2006.
- [93] H. Warren Moos. "Spectroscopic relaxation processes of rare earth ions in crystals." In: *Journal of Luminescence* 1-2 (1970), pp. 106–121. DOI: [https://doi.org/10.1016/0022-2313\(70\)90027-X](https://doi.org/10.1016/0022-2313(70)90027-X).



- [94] J.L. Adam, W.A. Sibley, and D.R. Gabbe. "Optical absorption and emission of  $\text{LiYF}_4:\text{Pr}^{3+}$ ." In: *Journal of Luminescence* 33.4 (1985), pp. 391–407. DOI: [https://doi.org/10.1016/0022-2313\(85\)90109-7](https://doi.org/10.1016/0022-2313(85)90109-7).
- [95] Bernard Valeur and Mario Nuno Berberan-Santos. *Molecular Fluorescence*. Wiley-VCH Verlag, 2012.
- [96] Ksenia Dolgaleva, Robert W. Boyd, and Peter W. Milonni. "Influence of local-field effects on the radiative lifetime of liquid suspensions of Nd:YAG nanoparticles." In: *Journal of the Optical Society of America B* 24 (3 2007), pp. 516–521. DOI: [10.1364/JOSAB.24.000516](https://doi.org/10.1364/JOSAB.24.000516).
- [97] Chang-Kui Duan and Michael F. Reid. "Dependence of the spontaneous emission rates of emitters on the refractive index of the surrounding media." In: *Journal of Alloys and Compounds* 418.1 (2006), pp. 213–216. ISSN: 0925-8388. DOI: <https://doi.org/10.1016/j.jallcom.2005.10.077>.
- [98] J. C. Maxwell Garnett. "XII. Colours in metal glasses and in metallic films." In: *Philosophical Transactions of the Royal Society of London. Series A, Containing Papers of a Mathematical or Physical Character* 203.359-371 (1904), pp. 385–420. DOI: [10.1098/rsta.1904.0024](https://doi.org/10.1098/rsta.1904.0024).
- [99] Hendrik Antoon Lorentz. *The theory of electrons and its applications to the phenomena of*. BG Teubner, 1916.
- [100] John David Jackson. *Classical electrodynamics*. Wiley, 1999.
- [101] Peter A. Tanner, Lei Zhou, Changkui Duan, and Ka-Leung Wong. "Misconceptions in electronic energy transfer: bridging the gap between chemistry and physics." In: *Chem. Soc. Rev.* 47 (14 2018), pp. 5234–5265. DOI: [10.1039/C8CS00002F](https://doi.org/10.1039/C8CS00002F).
- [102] Yanqing Hu, Qiyue Shao, Yan Dong, and Jianqing Jiang. "Energy Loss Mechanism of Upconversion Core/Shell Nanocrystals." In: *The Journal of Physical Chemistry C* 123.36 (2019), pp. 22674–22679. DOI: [10.1021/acs.jpcc.9b07176](https://doi.org/10.1021/acs.jpcc.9b07176).
- [103] B. Huang, J. Bergstrand, S. Duan, Q. Zhan, J. Widengren, H. Agren, and H. Liu. "Overtone Vibrational Transition-Induced Lanthanide Excited-State Quenching in  $\text{Yb}^{3+}/\text{Er}^{3+}$ -Doped Upconversion Nanocrystals." In: *ACS Nano* 12.11 (2018), pp. 10572–10575. DOI: [10.1021/acsnano.8b05095](https://doi.org/10.1021/acsnano.8b05095).
- [104] F. T. Rabouw, P. T. Prins, P. Villanueva-Delgado, M. Castelijns, R. G. Geitenbeek, and A. Meijerink. "Reply to "Overtone Vibrational Transition-Induced Lanthanide Excited-State Quenching in  $\text{Yb}^{3+}/\text{Er}^{3+}$ -Doped Upconversion Nanocrystals"." In: *ACS Nano* 12.11 (2018), pp. 10576–10577. DOI: [10.1021/acsnano.8b07376](https://doi.org/10.1021/acsnano.8b07376).

- [105] E. B. Sveshnikova and V. L. Ermolaev. "Inductive-resonant theory of nonradiative transitions in lanthanide and transition metal ions." In: *Optics and Spectroscopy* 111 (2011), pp. 34–50. DOI: [10.1134/S0030400X11070186](https://doi.org/10.1134/S0030400X11070186).
- [106] Valerii L Ermolaev, E B Sveshnikova, and E N Bodunov. "Inductive-resonant mechanism of nonradiative transitions in ions and molecules in condensed phase." In: *Physics–Uspekhi* 39.3 (1996), pp. 261–282. DOI: [10.1070/PU1996v039n03ABEH000137](https://doi.org/10.1070/PU1996v039n03ABEH000137).
- [107] Fiorenzo Vetrone, Rafik Naccache, Venkataramanan Mahalingam, Christopher G. Morgan, and John A. Capobianco. "The Active-Core/Active-Shell Approach: A Strategy to Enhance the Upconversion Luminescence in Lanthanide-Doped Nanoparticles." In: *Advanced Functional Materials* 19.18 (2009), pp. 2924–2929. DOI: <https://doi.org/10.1002/adfm.200900234>.
- [108] J. Zhao, X. Chen, B. Chen, X. Luo, T. Sun, W. Zhang, C. Wang, J. Lin, D. Su, X. Qiao, and F. Wang. "Accurate Control of Core–Shell Upconversion Nanoparticles through Anisotropic Strain Engineering." In: *Advanced Functional Materials* 29.44 (2019), p. 1903295. DOI: <https://doi.org/10.1002/adfm.201903295>.
- [109] Rajib Ghosh Chaudhuri and Santanu Paria. "Core/Shell Nanoparticles: Classes, Properties, Synthesis Mechanisms, Characterization, and Applications." In: *Chemical Reviews* 112.4 (2012), pp. 2373–2433. DOI: [10.1021/cr100449n](https://doi.org/10.1021/cr100449n).
- [110] Guanying Chen, Hans Agren, Tymish Y. Ohulchanskyy, and Paras N. Prasad. "Light upconverting core–shell nanostructures: nanophotonic control for emerging applications." In: *Chem. Soc. Rev.* 44 (6 2015), pp. 1680–1713. DOI: [10.1039/C4CS00170B](https://doi.org/10.1039/C4CS00170B).
- [111] Feng Wang, Renren Deng, Juan Wang, Qingxiao Wang, Yu Han, Haomiao Zhu, Xueyuan Chen, and Xiaogang Liu. "Tuning upconversion through energy migration in core–shell nanoparticles." In: *Nature Materials* 10.12 (2011), pp. 968–973. DOI: [10.1038/nmat3149](https://doi.org/10.1038/nmat3149).
- [112] Peng Ren, Xianlin Zheng, Jun Zhang, Simone De Camillis, Jianguo Jia, Hao Wang, Xiaozhou Liao, James A. Piper, and Yiqing Lu. "Quantifying the Influence of Inert Shell Coating on Luminescence Brightness of Lanthanide Upconversion Nanoparticles." In: *ACS Photonics* 9.3 (2022), pp. 758–764. DOI: [10.1021/acsp Photonics.1c01695](https://doi.org/10.1021/acsp Photonics.1c01695).
- [113] Alexis D. Ostrowski, Emory M. Chan, Daniel J. Gargas, Elan M. Katz, Gang Han, P. James Schuck, Delia J. Milliron, and Bruce E. Cohen. "Controlled Synthesis and Single-Particle Imaging of Bright, Sub-10 nm Lanthanide-Doped Upconverting Nano-



- crystals." In: *ACS Nano* 6.3 (2012), pp. 2686–2692. DOI: [10.1021/nn3000737](https://doi.org/10.1021/nn3000737).
- [114] M. Grabolle, M. Spieles, V. Lesnyak, N. Gaponik, A. Eychmüller, and U. Resch-Genger. "Determination of the Fluorescence Quantum Yield of Quantum Dots: Suitable Procedures and Achievable Uncertainties." In: *Analytical Chemistry* 81.15 (2009), pp. 6285–6294. DOI: [10.1021/ac900308v](https://doi.org/10.1021/ac900308v).
- [115] M. S. Meijer, P. A. Rojas-Gutierrez, D. Busko, I. A. Howard, F. Frenzel, C. Würth, U. Resch-Genger, B. S. Richards, A. Turshatov, J. A. Capobianco, and S. Bonnet. "Absolute upconversion quantum yields of blue-emitting  $\text{LiYF}_4:\text{Yb}^{3+},\text{Tm}^{3+}$  upconverting nanoparticles." In: *Phys. Chem. Chem. Phys.* 20 (35 2018), pp. 22556–22562. DOI: [10.1039/C8CP03935F](https://doi.org/10.1039/C8CP03935F).
- [116] A. Richter. *Laser Parameters and Performance of  $\text{Pr}^{3+}$ -doped Fluorides Operating in the Visible Spectral Region*. Cuvillier Verlag, 2007.
- [117] K. Pearson. "X. On the criterion that a given system of deviations from the probable in the case of a correlated system of variables is such that it can be reasonably supposed to have arisen from random sampling." In: *The London, Edinburgh, and Dublin Philosophical Magazine and Journal of Science* 50.302 (1900), pp. 157–175. DOI: [10.1080/14786440009463897](https://doi.org/10.1080/14786440009463897).
- [118] M. Pollnau and M. Eichhorn. "Emission Cross Section, Füchtbauer-Ladenburg Equation, and Purcell Factor." In: (2017). Ed. by Baldassare Di Bartolo, John Collins, and Luciano Silvestri, pp. 387–404.
- [119] D. E. McCumber. "Einstein Relations Connecting Broadband Emission and Absorption Spectra." In: *Phys. Rev.* 136 (1964), A954–A957. DOI: [10.1103/PhysRev.136.A954](https://doi.org/10.1103/PhysRev.136.A954).
- [120] Langping Tu, Xiaomin Liu, Fei Wu, and Hong Zhang. "Excitation energy migration dynamics in upconversion nanomaterials." In: *Chem. Soc. Rev.* 44 (6 2015), pp. 1331–1345. DOI: [10.1039/C4CS00168K](https://doi.org/10.1039/C4CS00168K).
- [121] Xiaowang Liu, Renren Deng, Yuhai Zhang, Yu Wang, Hongjin Chang, Ling Huang, and Xiaogang Liu. "Probing the nature of upconversion nanocrystals: instrumentation matters." In: *Chem. Soc. Rev.* 44 (6 2015), pp. 1479–1508. DOI: [10.1039/C4CS00356J](https://doi.org/10.1039/C4CS00356J).
- [122] Hao Dong, Ling-Dong Sun, and Chun-Hua Yan. "Energy transfer in lanthanide upconversion studies for extended optical applications." In: *Chem. Soc. Rev.* 44 (6 2015), pp. 1608–1634. DOI: [10.1039/C4CS00188E](https://doi.org/10.1039/C4CS00188E).

- [123] Guokui Liu. "Advances in the theoretical understanding of photon upconversion in rare-earth activated nanophosphors." In: *Chem. Soc. Rev.* 44 (6 2015), pp. 1635–1652. DOI: [10.1039/C4CS00187G](https://doi.org/10.1039/C4CS00187G).
- [124] Zijun Wang and Andries Meijerink. "Concentration Quenching in Upconversion Nanocrystals." In: *The Journal of Physical Chemistry C* 122.45 (2018), pp. 26298–26306. DOI: [10.1021/acs.jpcc.8b09371](https://doi.org/10.1021/acs.jpcc.8b09371).
- [125] Brian M. Walsh, Uwe Hommerich, Akira Yoshikawa, and Alessandra Toncelli. "Mid-infrared spectroscopy of Pr-doped materials." In: *Journal of Luminescence* 197 (2018), pp. 349–353. ISSN: 0022-2313. DOI: <https://doi.org/10.1016/j.jlumin.2018.01.032>.
- [126] Ksenia Dolgaleva and Robert W. Boyd. "Laser gain media based on nanocomposite materials." In: *J. Opt. Soc. Am. B* 24.10 (2007), A19–A25. DOI: [10.1364/JOSAB.24.000A19](https://doi.org/10.1364/JOSAB.24.000A19).
- [127] K. K. Pukhov, T. T. Basiev, and Yu. V. Orlovskii. "Spontaneous emission in dielectric nanoparticles." In: *JETP Letters* 88.1 (Sept. 2008), pp. 12–18. DOI: [10.1134/S0021364008130043](https://doi.org/10.1134/S0021364008130043).
- [128] Renren Deng, Juan Wang, Runfeng Chen, Wei Huang, and Xiaogang Liu. "Enabling Förster Resonance Energy Transfer from Large Nanocrystals through Energy Migration." In: *Journal of the American Chemical Society* 138.49 (2016), pp. 15972–15979. DOI: [10.1021/jacs.6b09349](https://doi.org/10.1021/jacs.6b09349).
- [129] Xian Chen, Limin Jin, Wei Kong, Tianying Sun, Wenfei Zhang, Xinhong Liu, Jun Fan, Siu Fung Yu, and Feng Wang. "Confining energy migration in upconversion nanoparticles towards deep ultraviolet lasing." In: *Nature Communications* 7.1 (Jan. 2016), p. 10304. DOI: [10.1038/ncomms10304](https://doi.org/10.1038/ncomms10304).
- [130] Mitio Inokuti and Fumio Hirayama. "Influence of Energy Transfer by the Exchange Mechanism on Donor Luminescence." In: *The Journal of Chemical Physics* 43 (6 Sept. 1965), pp. 1978–1989. DOI: [10.1063/1.1697063](https://doi.org/10.1063/1.1697063).
- [131] R. Naccache, F. Vetrone, A. Speghini, M. Bettinelli, and J. A. Capobianco. "Cross-Relaxation and Upconversion Processes in Pr<sup>3+</sup> Singly Doped and Pr<sup>3+</sup>/Yb<sup>3+</sup> Codoped Nanocrystalline Gd<sub>3</sub>Ga<sub>5</sub>O<sub>12</sub>: The Sensitizer/Activator Relationship." In: *The Journal of Physical Chemistry C* 112.20 (2008), pp. 7750–7756. DOI: [10.1021/jp711494d](https://doi.org/10.1021/jp711494d).
- [132] J. K. Wilmshurst and H. J. Bernstein. "The Infrared and Raman Spectra of Toluene, Toluene- $\alpha$ -d<sub>3</sub>, m-Xylene, AND m-Xylene- $\alpha\alpha'$ -d<sub>6</sub>." In: *Canadian Journal of Chemistry* 35.8 (1957), pp. 911–925. DOI: [10.1139/v57-123](https://doi.org/10.1139/v57-123).

- [133] J. Hegarty, D. L. Huber, and W. M. Yen. “Fluorescence quenching by cross relaxation in  $\text{LaF}_3:\text{Pr}^{3+}$ .” In: *Phys. Rev. B* 25 (9 1982), pp. 5638–5645. DOI: [10.1103/PhysRevB.25.5638](https://doi.org/10.1103/PhysRevB.25.5638).
- [134] Bill P. Petreski, Peter M. Farrell, and Stephen F. Collins. “Cross-relaxation in praseodymium-doped fluorozirconate glass.” In: *Optics Communications* 132.1 (1996), pp. 89–93. DOI: [https://doi.org/10.1016/0030-4018\(96\)00276-3](https://doi.org/10.1016/0030-4018(96)00276-3).
- [135] Xiongfeng Ma, Xiao Yuan, Zhu Cao, Bing Qi, and Zhen Zhang. “Quantum random number generation.” In: *npj Quantum Information* 2.1 (June 2016), p. 16021. DOI: [10.1038/npjqi.2016.21](https://doi.org/10.1038/npjqi.2016.21).
- [136] Alireza Marandi, Nick C. Leindecker, Konstantin L. Vodopyanov, and Robert L. Byer. “All-optical quantum random bit generation from intrinsically binary phase of parametric oscillators.” In: *Opt. Express* 20.17 (Aug. 2012), pp. 19322–19330. DOI: [10.1364/OE.20.019322](https://doi.org/10.1364/OE.20.019322).
- [137] Andy B. Yoo, Morris A. Jette, and Mark Grondona. “SLURM: Simple Linux Utility for Resource Management.” In: *Job Scheduling Strategies for Parallel Processing*. Ed. by Dror Feitelson, Larry Rudolph, and Uwe Schwiegelshohn. Berlin, Heidelberg: Springer, 2003, pp. 44–60. ISBN: 978-3-540-39727-4.
- [138] S. Spelthann, J. Thiem, O. Melchert, R. Komban, C. Gimmler, A. Demircan, A. Ruehl, and D. Ristau. “Predicting the Excitation Dynamics in Lanthanide Nanoparticles.” In: *Advanced Optical Materials* (2023), p. 2300096. DOI: <https://doi.org/10.1002/adom.202300096>.
- [139] Wiebke Albrecht, Ece Arslan Irmak, Thomas Altantzis, Adrián Pedraza-Tardajos, Alexander Skorikov, Tian-Song Deng, Jessi E.S. van der Hoeven, Alfons van Blaaderen, Sandra Van Aert, and Sara Bals. “3D Atomic-Scale Dynamics of Laser-Light-Induced Restructuring of Nanoparticles Unraveled by Electron Tomography.” In: *Advanced Materials* 33.33 (2021), p. 2100972. DOI: <https://doi.org/10.1002/adma.202100972>.
- [140] Yongliang Chen, Chi Li, Tieshan Yang, Evgeny A. Ekimov, Carlo Bradac, Son Tung Ha, Milos Toth, Igor Aharonovich, and Toan Trong Tran. “Real-Time Ratiometric Optical Nanoscale Thermometry.” In: *ACS Nano* 17.3 (2023), pp. 2725–2736. DOI: [10.1021/acsnano.2c10974](https://doi.org/10.1021/acsnano.2c10974).
- [141] Langping Tu, Kefan Wu, Yongshi Luo, Enhui Wang, Jun Yuan, Jing Zuo, Ding Zhou, Bin Li, Jiajia Zhou, Dayong Jin, and Hong Zhang. “Significant Enhancement of the Upconversion Emission in Highly  $\text{Er}^{3+}$ -Doped Nanoparticles at Cryogenic Temperatures.” In: *Angewandte Chemie International Edition* 62.7 (2023), e202217100. DOI: <https://doi.org/10.1002/anie.202217100>.

- [142] Jur W. de Wit, Thomas P. van Swieten, Marie Anne van de Haar, Andries Meijerink, and Freddy T. Rabouw. "Increasing the Power: Absorption Bleach, Thermal Quenching, and Auger Quenching of the Red-Emitting Phosphor  $K_2TiF_6:Mn^{4+}$ ." In: *Advanced Optical Materials* n/a.n/a (), p. 2202974. DOI: <https://doi.org/10.1002/adom.202202974>.
- [143] S. Spelthann, J. Thiem, L. Neumann, H.-H. Johannes, W. Kowalsky, D. Kracht, J. Neumann, A. Ruehl, and D. Ristau. "Fluorescence Dynamics of Laseractive Nanocrystals Emitting in the Visible." In: *2019 Conference on Lasers and Electro-Optics Europe & European Quantum Electronics Conference (CLEO/Europe-EQEC)*. 2019.

## LIST OF PUBLICATIONS

---

Some ideas and figures have appeared previously in the following publications:

### PEER REVIEWED PAPERS

- [1] **S. Spelthann**, D. H. Chau, L. F. Klepzig, D. A. Rudolph, M. Chemnitz, S. Junaid, D. Ristau, M. A. Schmidt, J. Lauth, and M. Steinke. "Microfluidic Filling and Spectroscopy of Colloidal CdSe/CdS Nanoplatelets in Silica Capillary Fibers." In: *Submitted to Optics Letters*. (2023). DOI: <https://doi.org/10.48550/arXiv.2303.09624>.
- [2] **S. Spelthann**, J. Thiem, O. Melchert, R. Kompan, C. Gimmler, A. Demircan, A. Ruehl, and D. Ristau. "Predicting the Excitation Dynamics in Lanthanide Nanoparticles." In: *Advanced Optical Materials* (2023), p. 2300096. DOI: <https://doi.org/10.1002/adom.202300096>.
- [3] **S. Spelthann**, R. Kompan, M. Steinke, D. Ristau, A. Ruehl, C. Gimmler, and H. Weller. "Bulk-like emission in the visible spectrum of colloidal LiYF<sub>4</sub>:Pr nanocrystals downsized to 10 nm." In: *Nanoscale Advances* 4.14 (Apr. 25, 2022), pp. 2973–2978. DOI: [10.1039/d2na00045h](https://doi.org/10.1039/d2na00045h).
- [4] M. Steinke, **S. Spelthann**, A. Rühl, and D. Ristau. "Absorption and multi-phonon quenching in nanocrystal doped SiO<sub>2</sub> fibers." In: *Optical Materials Express* 11.6 (2021), p. 1631. DOI: [10.1364/ome.424116](https://doi.org/10.1364/ome.424116).
- [5] **S. Spelthann**, S. Unland, J. Thiem, F. Jakobs, J. Kielhorn, P. Y. Ang, H.-H. Johannes, D. Kracht, J. Neumann, A. Ruehl, W. Kowalsky, and D. Ristau. "Towards Highly Efficient Polymer Fiber Laser Sources for Integrated Photonic Sensors." In: *Sensors* 20.15 (2020), p. 4086. DOI: [10.3390/s20154086](https://doi.org/10.3390/s20154086).
- [6] J. Thiem, **S. Spelthann**, L. Neumann, F. Jakobs, H.-H. Johannes, W. Kowalsky, D. Kracht, J. Neumann, A. Ruehl, and D. Ristau. "Upconversion Nanocrystal Doped Polymer Fiber Thermometer." In: *Sensors* 20.21 (2020), p. 6048. DOI: [10.3390/s20216048](https://doi.org/10.3390/s20216048).
- [7] L. Neumann, F. Jakobs, **S. Spelthann**, D. Zaremba, S. Radunz, U. Resch-Genger, R. Evert, J. Kielhorn, W. Kowalsky, and H.-H. Johannes. "Integration of  $\beta$ -NaYF<sub>4</sub> Upconversion Nanoparticles into Polymers for Polymer Optical Fiber Applications." In: *Optics and Spectroscopy* 125.5 (2018), pp. 711–715. DOI: [10.1134/s0030400x18110206](https://doi.org/10.1134/s0030400x18110206).

## INTERNATIONAL CONFERENCES

- [8] **S. Spelthann**, M. Steinke, R. Kompan, H. Weller, C. Gimm-ler, A. Ruehl, and D. Ristau. "Colloidal LiYF<sub>4</sub>:Pr nanocrystals downsized to 10 nm – Part 2: Spectroscopic Properties." In: *10th EPS-QEOD Europhoton Conference on Solid-State, Fibre, and Waveguide Coherent Light Sources (EUROPHOTON 2022)*. 2022.
- [9] R. Kompan, **S. Spelthann**, M. Steinke, D. Ristau, A. Ruehl, C. Gimm-ler, and Horst Weller. "Colloidal LiYF<sub>4</sub>:Pr nanocrystals downsized to 10 nm – Part 2: Synthesis and Micro-Structural Characteristics." In: *10th EPS-QEOD Europhoton Conference on Solid-State, Fibre, and Waveguide Coherent Light Sources (EUROPHO-TON 2022)*. 2022.
- [10] **S. Spelthann**, L. F. Klepzig, D. H. Chau, M. Chemnitz, S. Ju- naid, R. Stephan, K. Hausmann, M. Schmidt, J. Lauth, M. Steinke, and D. Ristau. "Optical emission characterization of liquid core fibers filled with colloidal nanoplatelets." In: *10th EPS-QEOD Europhoton Conference on Solid-State, Fibre, and Wave- guide Coherent Light Sources (EUROPHOTON 2022)*. 2022.
- [11] L. Koettters, **S. Spelthann**, L. Buehre, R. Kompan, H. Weller, R. Hanke-Rauschenbach, D. Ristau, C. Gimm-ler, B. Bensmann, and M. Steinke. "Fiber-tip nanothermometer based on up-conversion nanocrystals for electrolysis cells." In: *10th EPS-QEOD Europho- ton Conference on Solid-State, Fibre, and Waveguide Coherent Light Sources (EUROPHOTON 2022)*. 2022.
- [12] **S. Spelthann**, J. Thiem, L. Neumann, H.-H. Johannes, W. Kowal- sky, D. Kracht, J. Neumann, A. Ruehl, and D. Ristau. "Design of Pr:YLF Core-Shell Nanocrystals for Fiber Lasers Emitting in the Visible Spectral Range." In: *Nanophotonics and Micro/Nano Optics International Conference 2019*. Munich, Germany, 2019.
- [13] S. Unland, **S. Spelthann**, J. Thiem, F. Jakobs, J. Kielhorn, P. Y. Ang, H.-H. Johannes, D. Kracht, J. Neumann, A. Ruehl, W. Kowalsky, and D. Ristau. "Highly Efficient Rhodamine B Doped Polymer Fiber Lasers." In: *The 28th International Conference on Plastic Optical Fibers 2019*. Yokohama, Japan, 2019.
- [14] J. Thiem, **S. Spelthann**, L. Neumann, H.-H. Johannes, W. Kowal- sky, D. Kracht, J. Neumann, A. Ruehl, and D. Ristau. "Design and optimization of laseractive nanoparticles for fiber lasers." In: *2019 Conference on Lasers and Electro-Optics Europe & Euro- pean Quantum Electronics Conference (CLEO/Europe-EQEC)*. Mu- nich, Germany, 2019.
- [15] **Spelthann, S.**, J. Thiem, L. Neumann, H.-H. Johannes, W. Kowal- sky, D. Kracht, J. Neumann, A. Ruehl, and D. Ristau. "Flu- orescence Dynamics of Laseractive Nanocrystals Emitting in

- the Visible." In: *2019 Conference on Lasers and Electro-Optics Europe & European Quantum Electronics Conference (CLEO/Europe-EQEC)*. 2019.
- [16] R. Caspary, F. Jakobs, J. Kielhorn, P.Y. Ang, M. Cehovski, M. Beck, H.-H. Johannes, S. Balendat, J. Neumann, S. Unland, **Spelthann, S.**, J. Thiem, A. Ruehl, D. Ristau, and W. Kowalsky. "Polymer Fiber Lasers." In: vol. 67. 2019, pp. 1–4.
- [17] T. Hellwig, M. Brinkmann, **S. Spelthann**, and C. Fallnich. "Electronically Tunable Dual-Color All-Fiber Optical Parametric Oscillator." In: *2017 European Conference on Lasers and Electro-Optics and European Quantum Electronics Conference*. Optica Publishing Group, 2017.

## NATIONAL CONFERENCES

- [18] J. Thiem, **S. Spelthann**, L. Neumann, H.-H. Johannes, W. Kowalsky, D. Kracht, J. Neumann, A. Ruehl, and D. Ristau. "Laseraktive Nanokristalle für Polymerfasern (POF)." In: *Tagungsband Drittes Deutsches POF-Symposium*. 2020, pp. 43–58.
- [19] **S. Spelthann**, N. Tinne, D. Kracht, J. Neumann, and D. Ristau. "Nd<sub>2</sub>O<sub>4</sub>-Nanopartikel-Dispersionslaser im sichtbaren Spektralbereich." In: *DGaO-Proceedings 2018*. 2018.





## ACKNOWLEDGEMENTS

---

This work would not have been possible without the support and encouragement of many people. Therefore, I would like to express my gratitude:

First of all, I thank Prof. Dr. Detlev Ristau for supervising my thesis and his support during its creation.

Furthermore, I am thankful to Prof. Dr. Uwe Morgner and Prof. Dr. Markus A. Schmidt for evaluating my thesis.

I would like to express my deep gratitude to Dr. Axel Ruehl for supporting and inspiring me beyond the call of duty. He has been a valuable mentor to me during the time this thesis has been created.

I am thankful to Dr. Jonas Thiem for numerous interesting discussions (scientific and otherwise). Thanks to his commitment I started to enjoy programming after all. Various inside jokes testify to the fun we had working together. Inside jokes also characterized the spirit in room 163 which is why I look back fondly this time. I would like to thank all the people that contributed to this excellent and entertaining atmosphere.

I thank Dr. Michael Steinke very much for welcoming me in the Laser Components and Fibres group. He gave me a lot of freedom and responsibility to develop and pursue new ideas. Furthermore, he promoted me by helping me to extend my professional network and improving my ability to write down visionary ideas in proposals. I thank the whole group for welcoming me as a team member and the excellent working atmosphere.

This thesis would not have been possible without our collaborators, Dr. Rajesh Kombar and Dr. Christoph Gimmler, at the Fraunhofer Center for Applied Nanotechnology. They provided me with all samples and respective information needed. Thank you for this extraordinarily fruitful collaboration.

Dr. Oliver Melchert and Prof. Dr. Ayhan Demircan supported me with the core structure of the python script that lead to the results presented in this thesis. Thank you for the fruitful discussions.

Dr. Michael Zopf helped me implementing the fitting routines for the lifetimes. Thank you also for various lunch breaks with interesting conversations on physics and beyond.

I acknowledge Dr. Pascal Rusch for performing the quantum yield measurement, Dr. Christian Kraenkel and Dr. Sascha Kalusniak for providing absorption and emission cross section data for  $\text{LiYF}_4:\text{Pr}^{3+}$  bulk crystals, Tamara Grossmann and Dr. Torben Sell for helpful discussions on probability theory, and Dr. Reinhard Caspary for fruitful

discussions and valuable insight on the spectroscopy of lanthanide ions.

A lot of students supported me with their workforce and tried out my ideas: Pia Grupe (Student Research Project), Chao Ding (Student Research Project), Stefanie Unland (Student Research Project & Master thesis), Jannik Wagner (Internship), Jerry C. John (Student Research Project), Dan Huy Chau (Bachelor Thesis), Eugenius Naumenko (Internship), and Mahdiah Taheri (Master Thesis). Working with them helped me learn more about professional leadership and supervision. In addition, Dan Huy Chau provided some awesome scientific artwork that has also been used throughout this thesis.

I am deeply grateful for a lot of friends that accompanied me during this journey and took part in my successes and defeats.

Finally, I want to express my deep love to my family: Luisa, you always encouraged me to take a step back during the harder times. You complete my weaknesses and highlight my strengths. My gratitude exceeds my ability to express it. Lisanne and Mileen, thank you for making sure that I did not work too much and distracting me from stressful situations. You both are wonderful and excellent! Mum and Dad, you encouraged my curiosity and inquisitiveness from my childhood on and I would not have been able to go to university without you. Lisa, I am proud of you, you are an amazing sister!

# CURRICULUM VITÆ

## PERSONAL DATA

*Name* Simon Spelthann  
*ORCID* 0000-0003-1387-0577  
*Born* 06.06.1990  
in Meyrin, Canton Geneva, CH  
*Nationality* German  
*Family* married, two children (\*2018 & \*2021)

## CAREER

*since 02/2023* Member of the Cluster of Excellence PhoenixD  
*since 12/2022* Member of the Cluster of Excellence QuantumFrontiers  
*since 11/2021* Research assistant at Laser Components and Fibres Group, Institute of Quantum Optics, Leibniz University Hannover  
*05 & 09/2021 + 03/2022* Parental leave  
*08/2020–10/2021* Research assistant at Ultrafast Photonics Group, Laser Zentrum Hannover  
*09/2018 + 08/2019* Parental leave  
*05/2017–07/2020* Research assistant at Institute of Quantum Optics, Leibniz University Hannover  
*2012–2014* Teaching assistant for lab supervision and tutoring in Physics at FH Münster

## UNIVERSITY EDUCATION

*since 2017* Ph.D. Candidate Physics, Leibniz University Hannover  
*2014–2017* Studies of Engineering Physics at FH Münster, M.Sc.  
*Investigations on the Spectral Emission Bandwidth of a Fiber-based Optical Parametric Oscillator*, Prof. Fallnich, University of Münster.  
*2012–2015* Studies of Industrial Engineering at FH Münster, B.Sc.  
*Laser Heating of Carbon Modifications*, Physics Lab, FH Münster.  
*2011–2014* Studies of Engineering Physics at FH Münster, B.Sc.  
*Cer-doped YAG - A Transparent Phosphor for a Laser-based Light Source in Automotive Headlights*, Hella GmbH.

## EDUCATION & VOLUNTEER SERVICE

*2010–2011* Federal Volunteer Service, Centre des Jeunes, Brittany, France  
*2010* Abitur, Lise-Meitner-Gymnasium Geldern

June 19, 2023



## COLOPHON

This document was typeset using the typographical look-and-feel `classicthesis` developed by André Miede. The style was inspired by Robert Bringhurst's seminal book on typography "*The Elements of Typographic Style*". `classicthesis` is available for both  $\text{\LaTeX}$  and  $\text{\LyX}$ :

<https://bitbucket.org/amiede/classicthesis/>

Happy users of `classicthesis` usually send a real postcard to the author, a collection of postcards received so far is featured here:

<http://postcards.miede.de/>

*Final Version* as of June 19, 2023 (`classicthesis`).

